In situ deformation transmission electron microscopy investigation of the mechanical behaviours of nanomaterials

Yujie Chen

A thesis submitted in partial fulfilment of requirements
for the degree of Doctor of Philosophy

Faculty of Engineering and IT
The University of Sydney

2016

献给我的父母

Dedicated to my parents

Declaration

I hereby declare that this submission is my own work and that, to the best of my knowledge and belief, it contains no material previously published or written by another person nor material which to a substantial extent has been accepted for the award of any other degree or diploma of the university or other institute of higher learning, except where due acknowledgment has been made in the text.

Signed:_____ On: 23/03/2016

Abstract

Due to their low-dimensional structures, nanomaterials demonstrate many interesting properties that are not seen in bulk materials, for example discrete carrier energy levels in nanostructured semiconductors, and a larger dynamic range of elastic and plastic strains observed in nanostructured materials. With their superior properties and nanoscale dimensions, nanomaterials including nanowires (NWs) and nanofilms have many significant applications in areas including solar cells, nanogenerators, lasers, photodetectors, and highly-sensitive biological and chemical sensors. The mechanical properties of these nanomaterials are a crucial factor in designing devices where predictable and reproducible operation is important. As such, mechanical characterisation of nanomaterials is necessary. However, because of the difficulty of mechanical testing of nanoscale objects, mechanical properties of nanomaterials have been less investigated.

Many techniques have been used to study the mechanical behaviours of nanomaterials. Among them, *in situ* deformation transmission electron microscopy (TEM) is one of the most effective approaches. This thesis aims to apply an *in situ* deformation TEM technique combined with finite element analysis (FEA) to investigate the mechanical behaviours of semiconductor NWs, and also aims to develop an *in situ* technique to extract the Young's modulus of thin films with a thickness down to ~ 2 nm.

In the first chapter of this thesis, the applications, synthesis methods, nanomechanical characterisation techniques, and mechanical behaviours of nanomaterials (mainly focusing on NWs and nanofilms) are summarised.

The second chapter provides a general understanding of the methods used in this thesis, including TEM, scanning electron microscopy, *in situ* nanomechanical characterisation, and FEA. Details of the experimental and modelling procedures are also described.

Loading misalignment and tapering of nanowires are usually unavoidable factors in compression and tensile mechanical property testing of nanowires.

Unfortunately, these two factors have been largely ignored in previous data analysis of NW mechanical characterisation using uniaxial compression or tension. In the third chapter, quantitative FEA and experimental measurements were conducted to investigate how these two factors affect the measured compression and tensile mechanical properties if they are not included in the data analysis. The results obtained show that ignoring these two factors leads to different degrees of underestimation of the critical buckling load, Young's modulus, and tensile fracture strength.

The fourth chapter discusses the effect of a high density of stacking faults (SFs) on the Young's modulus of GaAs NWs. The Young's moduli of GaAs NWs with two distinct structures – defect-free single crystalline wurtzite (WZ) and highly-defective wurtzite containing a high density of SFs (WZ-SF) – were investigated using combined *in situ* compression TEM and FEA. The Young's moduli of both WZ and WZ-SF GaAs NWs were found to increase with decreasing diameter due to the increasing volume fraction of the native oxide shell. The presence of a high density of SFs was further found to increase the Young's modulus by 12%. This stiffening effect of SFs is attributed to the change in the interatomic bonding configuration at the SFs.

Determination of the elastic modulus of nanostructures with sizes at a several nanometre range is a significant challenge. In the fifth chapter, a method is developed to measure the Young's modulus of nanoscale films with thicknesses down to ~ 2 nm by using a core–shell NW structure. *In situ* nano-compression in a TEM and FEA were used to determine the Young's modulus of the core–shell NWs. The Young's modulus of the shell at varying thicknesses was then extracted using a core–shell model. The method was applied to the GaAs–Al_2O_3 core–shell NW system. The results indicate that the elastic modulus of amorphous Al_2O_3 (a-Al_2O_3) shells (thin films) increases significantly when the thickness of the layer is smaller than 5 nm. This phenomenon can be attributed to the re-construction of the bonding on the surface of the material, coupled with the increase of the surface-to-volume ratio with reducing materials dimensions.

In the last chapter, major conclusions are drawn from this PhD research. Some possible future work is proposed as extension of what has been achieved.

Acknowledgements

This dissertation would not have been possible without the guidance of my academic supervisors, the support of my colleagues and friends, and the love of my family. This is the time to say thank you:

Foremost, I would like to express my sincere gratitude to my supervisor, Professor Xiaozhou Liao, for his guidance, enthusiasm, and encouragement in all aspects of my PhD study. He has been an irreplaceable role model for my research and academic life, and the knowledge I learnt from him extends beyond what can be found in any textbook.

I would like to especially thank my co-supervisor, Professor Yiu-Wing Mai, who provided me with excellent guidance along the way.

I would like to offer my thanks to Professor Chennupati Jagadish and Professor H. Hoe Tan of the Australian National University, Professor Jin Zou of the University of Queensland, and Professor Simon P. Ringer of the University of Sydney for their excellent collaboration and valuable advice.

My thanks also go to Dr Qiang Gao and Mr Tim Burgess of the Australian National University for providing GaAs nanowire samples. I also would like to acknowledge the technical help on the use of electron microscopes provided by Dr Hongwei Liu and Mr Steve Moody from the Australian Centre for Microscopy & Microanalysis.

Professor Xiaodong Han of Beijing University of Technology is acknowledged for hosting my three-month visit to his laboratory. During the visit, I learned the atomic-scale in situ straining TEM technique – developed by the Han group – from Dr Lihua Wang, Ms Yan Lu, and Mr Zhiming Liao.

I extend my thanks to all of the past and present members of Professor Liao's group. In particular, I am grateful for the critical discussion and helpful advice given by Dr Xianghai An, Dr Yanbo Wang, and Dr Bin Chen. In addition, I thank Mr Zibin Chen, Dr Jingli Sun, Dr Yang Cao, Mr Silu Liu, and Mr Peng Gao for their great

support and companionship.

Most importantly, I wish to thank my beloved family for their continued love and support throughout this whole experience.

Publication List

Book Chapter:

Y.J. Chen, X.Z. Liao
Mechanical Behaviors of Semiconductor Nanowires.
Semiconductor Nanowires: Part B, Semiconductors and Semimetals, Vol. 94, pp. 109-158. USA: Elsevier.
(ISBN: 978-0-12-804016-4)

Journal Papers:

1. **Y.J. Chen**, T. Burgess, X.H. An, Y.-W. Mai, H.H. Tan, J. Zou, S.P. Ringer, C. Jagadish, X.Z. Liao
   Effect of a high density of stacking faults on the Young's modulus of GaAs nanowires
   Nano Letters **16** (2016) 1911-1916.

2. **Y.J. Chen**, X.H. An, X.Z. Liao, Y.-W. Mai
   Effects of loading misalignment and tapering angle on the measured mechanical properties of nanowires
   Nanotechnology **26** (2015) 435704.

3. **Y.J. Chen**, Q. Gao, Y.B. Wang, X.H. An, X.Z. Liao, Y.-W. Mai, H.H. Tan, J. Zou, S.P. Ringer, C. Jagadish
   Determination of Young's modulus of ultrathin nanomaterials
   Nano Letters **15** (2015) 5279-5283.

4. B. Chen, J. Wang, Q. Gao, **Y.J. Chen**, X.Z. Liao, C.S. Lu, H. Tan, Y.-W. Mai, J. Zou, S.P. Ringer, H. J. Gao, C. Jagadish
   Strengthening brittle semiconductor nanowires through stacking faults: insights from in situ mechanical testing.
   Nano Letters **13** (2013) 4369-4373.

Table of Contents

Declaration II

Abstract III

Acknowledgements V

Publication List VII

Table of Contents VIII

List of Figures XI

List of Tables XVII

List of Acronyms XVIII

1 Introduction 1

1.1 Applications of nanomaterials 2

1.2 Fabrication of semiconductor nanowires 3

1.3 Fundamental concepts of mechanical properties 5

1.4 Methods for testing the mechanical behaviours of nanomaterials 9

1.4.1 Bending 10

1.4.2 Resonance 12

1.4.3 Uniaxial loading 13

1.4.4 Nanoindentation 15

1.4.5 Computational approaches 15

1.5 Mechanical behaviours of nanomaterials 16

1.5.1 Young's modulus 16

1.5.2 Elastic strain 20

1.5.3 Anelasticity 22

1.5.4 Plastic strain 24

1.5.5 Fracture strength 31

1.5.6 Fatigue 33

1.6 Outstanding issues in the field and the aims of this thesis 35
2 Methodology 37
2.1 Electron microscopy 37
2.1.1 Brief history of electron microscopy 37
2.1.2 Interactions of electrons with matter 38
2.1.3 Transmission electron microscopy 39
2.1.4 Scanning electron microscopy 42
2.2 *In situ* TEM nanomechanical testing 43
2.2.1 An overview of *in situ* TEM nanomechanical testing 43
2.2.2 The PI 95 TEM PicoIndenter 44
2.3 Fundamental concepts of finite element analysis 47
2.3.1 What is finite element analysis? 47
2.3.2 How does finite element analysis work? 48
2.4 Experimental and analytical procedures 52
2.4.1 Specimens 52
2.4.2 Structural characterisation 53
2.4.3 *In situ* compression in TEM 53
2.4.4 Finite element analysis 55
3 Effects of loading misalignment and tapering angle on the measured mechanical properties of nanowires 61
3.1 Introduction 61
3.2 Methods 62
3.3 Effect of tapering angle 64
3.4 Effect of loading misalignment 68
3.5 Combined effect of misalignment and tapering 72
3.6 Conclusions 72
4 Effect of a high density of stacking faults on the Young's modulus of GaAs nanowires 74

4.1 Introduction 74
4.2 Results 75
4.3 Discussion 83
4.4 Conclusions 85
5 Young's modulus of ultrathin nanomaterials 86
5.1 Introduction 86
5.2 Results 87
5.3 Discussion 96
5.4 Conclusions 98
6 Conclusions and future perspectives 99
6.1 Conclusions 99
6.2 Future work 101
7 References 105

List of Figures

Figure 1-1 Schematic diagram of NW growth via the vapour–liquid–solid mechanism (adapted from Dailey et al. [44]). 4

Figure 1-2 A typical engineering stress–strain curve for metals [47].....6

Figure 1-3 A typical buckling load-displacement curve for a slender column subjected to an axial compressive load.....9

Figure 1-4 A series of SEM images showing a bending-deformation process of a NW. One end of the NW is fixed on the carbon film by the electron-beam-induced deposition of Pt. The other end is gradually bent by a manipulator. The top right corner of the images indicates the time-stamp (in seconds) during the experiment [10].....12

Figure 1-5 An illustration of the NW tensile testing technique using bimetallic strips. (a) Prior to the tensile test. (b) During the tensile test [90].....14

Figure 1-6 A series of TEM images showing the anelastic behaviour of a GaAs NW with a diameter of ~ 25 nm. (a) Before deformation. (b) During deformation with arrows indicating the bending contours. (c) Immediately after the external stress was completely removed. The gap between the two dotted arrows is the difference between the current and original positions of the NW tip. (d, e) The NW gradually returned to its original shape. Dotted ellipses mark the region for contrast comparison. (f) The NW completely recovered to its original shape. The inset in (f) presents the whole length of the NW. The scale bar in the inset image is 200 nm [84].....23

Figure 1-7 A typical atomic-resolution TEM image of the interface in a NW with SFs [84].....24

Figure 1-8 An atomic-scale *in situ* observation of a Lomer lock dislocation–formation process via a dislocation reaction and the subsequent crystalline to amorphous transition. (a, b) A glissile dislocation with a Burgers vector of b = 1/2[011] and 1/2[$10\bar{1}$], respectively. (c) A Lomer lock dislocation

formed via the reaction of the two dislocations shown in (a) and (b). (d) An enlarged HRTEM image showing the Lomer lock structure. (e, f) Enlarged HRTEM images showing a crystalline to amorphous transition process at the atomic scale [69]. 26

Figure 1-9 An *in situ* TEM tensile test of a single Si NW. (a) Snapshots of the tensile elongation and fracture process. Uniform elongation occurred until simultaneous abrupt fracture at two positions. (b) An HRTEM image of the Si a NW at fracture site. (c) Typical stress−strain curve illustrating a linear elastic deformation until abrupt failure with the values of fracture stress and strain of 8.7 GPa and 4.6%, respectively [12]. 28

Figure 1-10 The microstructural evolution of a GaAs NW during a bending–release process. (a) An HRTEM image and a corresponding SAED pattern of a NW deformed 4.81% show a very high density of dislocations. (b) An HRTEM image of the NW following release of the applied load. The inset SAED pattern is identical to that of the undeformed sample [10]. 30

Figure 1-11 The effect of size-dependent defect density on the fracture strength of SiC NWs. (a) Fracture strength of SiC NWs as a function of the diameter. (b) Defect density as a function of NW diameter. The range between the dotted lines corresponds to the diameter range tested (17 nm−45 nm) [181]. 34

Figure 2-1 The interactions between a high-energy electron beam interacts and a thin material [193]..... 39

Figure 2-2 Schematic diagrams showing the TEM three-stage magnification imaging system in the diffraction mode (left) and the imaging mode (right) [193]. 40

Figure 2-3 A schematic representation of the principle of the SEM [198]..... 43

Figure 2-4 PI 95 TEM PicoIndenter holder for usage in JEOL TEMs [201]. 45

Figure 2-5 The transducer actuation diagram [201]. 46

Figure 2-6 Schematic diagram of a system composed of two springs (Element 1 and 2) loaded by external forces. 50

Figure 2-7 Schematic diagram of an isolated element composed of a single spring loaded by external forces. 50

Figure 2-8 Schematic diagram showing the isolated single elements split from an original system composed of two springs. 51

Figure 2-9 Schematic diagram of NW compression tests performed by the PI 95 TEM PicoIndenter 54

Figure 2-10 A C3D8R eight-node linear brick reduced integration element with one integration point. 55

Figure 2-11 A 2-D solution region divided into many small subregions using the triangular elements with different mesh sizes. “elts” = elements, “nds” = “nodes”. 56

Figure 2-12 Contour plots of the stress distribution for the same plate obtained for different mesh sizes. 57

Figure 2-13 The effect of the number of elements (mesh size) on the Young’s modulus obtained from FEA. 58

Figure 2-14 NW models with mesh sizes of 20 nm and 7.2 nm, which yield 2,160 and 31,680 elements, respectively. 59

Figure 3-1 (a) Schematic diagram of a tapered NW under compression. (b) Contour plots of maximum principal stress distribution of NWs with a slenderness ratio of 15 and different degrees of tapering angle under the same compressive loading condition. (c) The effect of tapering angle on the normalised critical buckling load of tapered NWs with different slenderness ratios under uniaxial compression. 65

Figure 3-2 (a) Schematic diagram of a tapered NW under tension. (b) Contour plots of maximum principal stress distribution of NWs with a slenderness ratio of 15 and different degrees of tapering angle under the same tensile loading condition. (c) The effect of tapering angle on the normalised tensile

fracture load of tapered NWs with different slenderness ratios under uniaxial tension. 66

Figure 3-3 (a) Schematic diagram of a cylindrical NW under tension with misalignment angle. (b) Contour plot of maximum principal stress distribution of a cylindrical NW under uniaxial tension and 10°-misaligned tension. (c) The effect of loading misalignment angle on the normalised fracture load of a cylindrical NW with a diameter of 100 nm and a length of 1.5 μm under tension. The insets are the contour plots of maximum principal stress distribution at one end of a cylindrical NW under uniaxial tension (left) and 10°-misaligned tension (right). 69

Figure 3-4 (a)–(c) Loading misalignment angle of 0°, 4°, and 6° between the NW axial direction and the loading direction. (d) Force-displacement curves of the same NW with different misalignment angles. The flat portion of the red curve indicated by the arrow is caused by the plastic deformation of the Au particle at the NW tip during the first compression test. (e) The effects of misalignment angle of loading on the normalised critical buckling load of cylindrical NWs under compression. 71

Figure 4-1 Low magnification TEM images of WZ (a) and WZ-SF (b) GaAs NWs. Diffraction contrast (c) and HRTEM (d) images of WZ GaAs NWs. Diffraction contrast (e) and HRTEM (f) images of WZ-SF GaAs NWs. The inset in (c) and (e) are their corresponding SAED patterns. 76

Figure 4-2 (a) An SEM image showing that the WZ and WZ-SF NWs are oriented perpendicularly to the GaAs substrate surface. SEM images show that the cross sections of both WZ (b) and WZ-SF (c) NWs are hexagonal. 77

Figure 4-3 (a) A portion of a load-time curve (from 3 s to 13 s) of an *in situ* compression process of a WZ-SF GaAs NW. The inset shows the complete load-displacement-time curve of the whole compression process. (b)–(e) A series of microscopy images corresponding to points 1 (before compression), 2 (the starting point of buckling), 3, and 4 (fracture point), respectively, in

(a). (f) FEA simulation of the maximum principal strain corresponding to the deformation state at (d). 79

Figure 4-4 Experimental results showing the effective Young's modulus of WZ (black rhombus) and WZ-SF (red dot) GaAs NWs as a function of diameter and best fits to the WZ (black solid line) and WZ-SF (red solid line) data by the core–shell NW model..... 80

Figure 5-1 (a) An SEM image showing that the GaAs–a-Al_2O_3 core–shell NWs are oriented perpendicularly to the GaAs substrate surface. (b) A typical low magnification TEM image of a GaAs NW with a 10 nm thick a-Al_2O_3 shell. The inset is a corresponding SAED pattern. (c) An HRTEM image of the NW in (b). 88

Figure 5-2 An HRTEM image of a GaAs NW with a native oxide layer on the surface. 89

Figure 5-3 (a) A portion of a load-time curve (from 2.5 to 9.5 s) of an *in situ* compression process of a GaAs NW with a 5-nm thick a-Al_2O_3 shell. The inset shows the complete load-displacement-time curve of the whole compression process. The three arrowheads indicate load drops caused by plastic deformation of the Au particle at the tip of the NW. (b)–(e) A series of microscopy images corresponding to points 1 (before compression), 2 (starting point of buckling), 3, and 4 (fracture point), respectively, in (a). The white arrows in (b)–(e) point to the NW being tested. 90

Figure 5-4 A typical tapered FEA NW model with a tapering angle of ~ 0.7°. The model was meshed using C3D8R elements with a mesh size of 10 nm. 91

Figure 5-5 (a)–(d) FEA simulations of the maximum principal strain corresponding to the deformation state at Figures 5-3(b), (c), (d), and (e), respectively. 92

Figure 5-6 (a) The failure strain of GaAs core–shell NWs with different thicknesses of the a-Al_2O_3 shell (open squares) or with a 2 nm thick native oxide shell (red star). (b) Young's modulus of GaAs–a-Al_2O_3 NWs as a

function of shell thickness. The red stars in (a) and (b) are the corresponding values for a GaAs NW with native oxide shell.....93

Figure 5-7 Young's modulus of a-Al_2O_3 as a function of shell thickness. The red star corresponds the value for a GaAs NW with a native oxide shell.....95

List of Tables

Table 1-1 Elastic, plastic, and fracture strain of semiconductor NWs.....21

Table 1-2 Fracture strength of semiconductor NWs and their bulk counterparts. 32

List of Acronyms

a-Al_2O_3	Amorphous Al_2O_3
AFM	Atomic force microscope
FEA	Finite element analysis
HRTEM	High-resolution transmission electron microscopy
MD	Molecular dynamics
NW	Nanowire
PTP	Push-to-pull
SEM	Scanning electron microscopy or scanning electron microscope
SAED	Selected area electron diffraction
SF	Stacking fault
TEM	Transmission electron microscopy or transmission electron microscope
TSL	Twinning superlattices
2-D	Two-dimensional
WZ	Wurtzite
ZB	Zinc blende

1 Introduction

Nanomaterials are defined as materials with structural features (e.g., grain sizes) smaller than ~ 100 nm in at least one dimension. Nanowires (NWs) are one-dimensional nanomaterials with diameters ranging from several to several hundred nanometres and lengths varying from hundreds of nanometres to several millimetres [1-4]. Nanofilms are two-dimensional nanomaterials with thicknesses in the nanoscale range [5].

Nanomaterials demonstrate many interesting physical, chemical, and mechanical properties that are not seen in bulk materials because of their low-dimensional structures. For example, semiconductor nanomaterials have a unique quantum-mechanics effect that leads to discrete-carrier (electron and hole) energy levels in the nanomaterials, which is different from the continuous energy levels presented in bulk materials [6, 7]. Nanostructured materials can apparently sustain a larger dynamic range of elastic and plastic strains than their bulk counterparts [8-10]. Mechanical properties, such as Young's modulus and fracture strength, are independent of size in bulk materials, but they show strong size-dependency in nanomaterials [8, 11-13]. The unique characteristics permit many applications of nanomaterials, including nanosensors [14-16], nanogenerators [17] and nanolasers [18]. Over the past two decades, the field of nanomaterials – including metals and alloys, magnetic materials, semiconductors, and oxides – has undergone a significant expansion, becoming one of the most active research areas in materials science. Nanomaterials such as nanowires (NWs) and nanofilms have received increasing attention because of their unique properties and significant applications. The mechanical properties of these nanostructures are a crucial factor in designing such devices, where predictable and reproducible operation is crucial. In the literature review of this thesis, the applications, synthesis methods, nanomechanical characterisation techniques, and mechanical behaviours of nanomaterials (focusing on NWs and nanofilms) are summarised.

1.1 Applications of nanomaterials

Due to their novel physical and mechanical properties, nanomaterials have significant advanced applications in areas including nanolasers [18], nanogenerators [17], solar cells [19-21], nanosensors [14-16], thermoelectrics [22, 23], nanoscale transistors [24-26], actuators [27], and light-emitting diodes [28-30]. Some applications of NWs and nanofilms are briefly discussed below.

Semiconductor NWs are key building blocks for bottom-up nanotechnology. For example, by taking advantage of the superior mechanical properties and piezoelectric property of ZnO NWs, a ZnO NW-based nanogenerator was developed, which can convert ambient vibration, hydraulic energy, and mechanical movement to electricity [17]. These devices provide a solution to power battery-free wireless nanodevices.

Si NWs with rough surfaces can be essentially thermal insulators, but with good electrical conductivity [22, 23]. Therefore, they can be used as excellent thermoelectric materials for converting heat – which could be otherwise lost to the environment during fuel combustion – to electricity.

Solar cells are attractive because they provide clean and renewable power. Compared to the planar semiconductors that are used in thin-film solar cells, NW arrays show low reflective losses, strong light-trapping capability, and long optical path lengths while maintaining short distances for carrier collection. Moreover, the cost of NW solar cells is relatively low [19-21]. These features make NW solar cells more efficient and less expensive than planar Si solar cells. Further, at a significantly reduced size, NW solar cells might serve as integrated power sources for nanoelectronic systems.

Semiconductor NWs can also be used for interfacing with living cells. Research has provided a good understanding of the electrical functionality of semiconductor NWs [14, 24, 25]. The large surface-to-volume ratio of NWs significantly enhances the communication between cells and NWs. In addition, the dimensions of NWs are much smaller than the typical cell dimensions, making NWs very comparable and compatible to the dimensional scale of biological and chemical species, and less invasive. All these characteristics make NWs excellent candidates

for creating nanosensors to be used to detect a wide range of chemical and biological species such as proteins, antibodies, and viruses [14-16].

Optically-active semiconductor (e.g., III-V compound semiconductor) NWs are good candidates to replace thin films in computing tools that will merge photonics with electronics on a single platform, because NW growth enables a dislocation-free semiconductor, while conventional thin-film technologies often result in highly-defective optical semiconductors. The presence of crystallographic defects can adversely affect the optical and electrical properties of semiconductors [31].

In addition to ZnO NWs, highly-efficient piezoelectric thin films – such as $(Pb_{0.92}Sr_{0.08})(Zr_{0.65}Ti_{0.35})O_3$ (PSZT) – can also convert small mechanical movement into electrical voltage to power silicon transistor logic, and to enable micro- and nano-electronic circuits which can scavenge their power from their environment. Moreover, it has been proposed that the piezoelectric thin films are more suitable for powering nanosensors than nanowires, since they have higher voltage output and current [32].

Due to their large surface-to-volume ratio, nanofilms have been extensively used in ultrasensitive sensors for ultrafine resolution applications. ZnO is an important semiconductor for toxic and combustible gas-sensing devices. The gas-sensing principle involves absorption of oxygen from gas molecules on the sensor surface causing charge transfer, leading to a change in surface resistance of the sensor element [33]. Therefore, ZnO nanofilms exhibit a higher degree of gas sensitivity compared to other forms of sensor elements.

1.2 Fabrication of semiconductor nanowires

The fabrication of semiconductor NWs with well-controlled surface, orientation, diameter, and length is the first step in the development of semiconductor NW-based devices. A variety of “top-down” and “bottom-up” methods have been developed to synthesise semiconductor NWs. The top-down approaches use a subtractive fabrication strategy. An example is Si NW fabrication from silicon-on-insulator wafers using electron-beam lithography [34]. Bottom-up approaches produce crystalline one-dimensional structures via directed self-assembly of atoms from

source materials. Bottom-up approaches usually produce devices that are much cheaper than those produced using top-down approaches. Bottom-up approaches have been widely used for the growth of semiconductor NWs, producing NWs with relatively smooth surfaces, which can be difficult to achieve using a top-down approach.

Currently, the most popular bottom-up approach for NW synthesis is the vapour–solid–liquid growth technique [35-42], first described by Wagner and Ellis in 1964 with silicon whiskers grown using gold (Au) catalyst [42]. This technique uses a liquid metal particle (often Au) as a catalyst, which is heated to react with the supplied source vapour semiconductor materials to form a liquid-alloy particle. This alloy particle becomes supersaturated on continuous supply of the source materials and the excess semiconductor materials precipitate at the bottom of the particle in the form of a one-dimensional semiconductor NW, with a diameter comparable to the size of the particle. Further growth and extension of the NW occur through continuous precipitation of additional materials at the interface between the alloy particle and the NW [43]. The different steps involved in the vapour–solid–liquid growth mechanism are demonstrated in Figure 1-1.

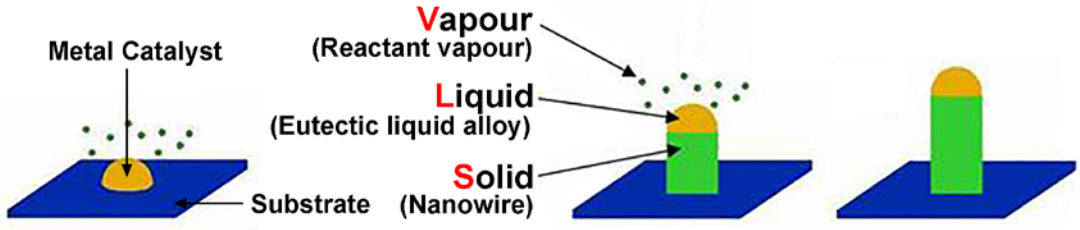

Figure 1-1 Schematic diagram of NW growth via the vapour–liquid–solid mechanism (adapted from Dailey et al. [44]).

The advantage of the vapour–liquid–solid approach is that it can grow a broad range of NW materials, including group IV, III-V and II-VI semiconductors in core–shell, superlattice, and branched structures with precisely controlled composition and morphology [37, 38, 41, 45, 46]. The development in NW synthesis techniques makes

it possible to control NW growth and manipulate the electrical, mechanical, and thermal properties of NWs.

1.3 Fundamental concepts of mechanical properties

Materials are usually subjected to force or load when in service. It is therefore necessary to understand the mechanical behaviours and properties of materials under various types of applied load, including tension, compression, torsion, and shear. Mechanical properties depend mainly on the chemical composition and structure of materials, and are measured through standardised mechanical tests.

In many situations, mechanical testing data are recorded as engineering stress vs engineering strain. Engineering stress is defined as the instantaneous applied load divided by the original cross-sectional area of the specimen. Engineering strain is defined as the change in the length of materials at some instant, divided by the original length of the specimen. Mechanical properties can be extracted from a stress–strain curve [47].

Figure 1-2 shows a typical tensile engineering stress–strain curve for a ductile metallic material. The material first undergoes elastic, or non-permanent, deformation, in which stress and strain are proportional, i.e., there is a linear relationship between the stress and the strain. The slope of this linear elastic region is the Young's modulus – or elastic modulus – of the material, which is a measure of the stiffness of the material. At the atomic scale, the magnitude of the Young's modulus is a measure of the resistance to separation of adjacent atoms, or the interatomic-bonding force. Elastic deformation is reversible; when the applied load is released, the material returns to its original shape.

Elastic deformation is usually time-independent. Upon release of the load, the elastic strain is completely recovered (i.e., the strain returns to zero immediately). However, in some materials, there also exists a time-dependent elastic-strain component, and some finite time is required for complete recovery after the load has been released. This time-dependent elastic behaviour is known as anelasticity, and it

is due to time-dependent microscopic and atomistic processes that are attendant to the deformation [47].

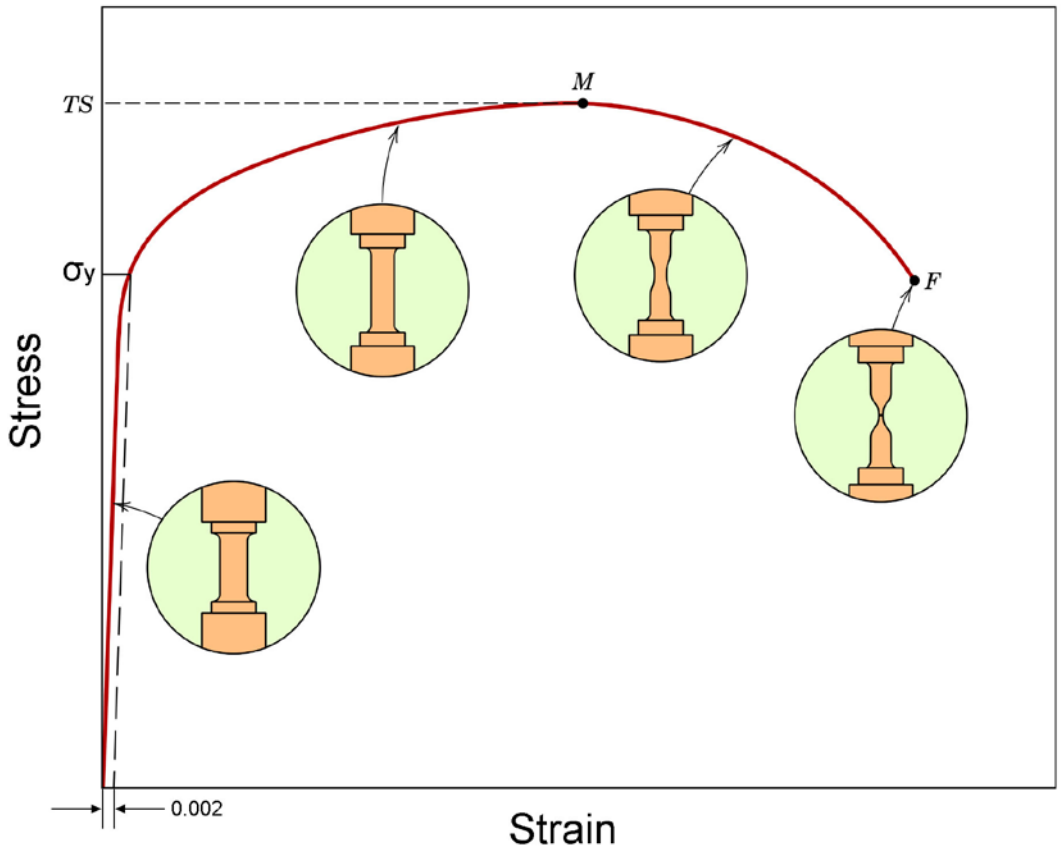

Figure 1-2 A typical engineering stress–strain curve for metals [47].

Beyond a certain stress level, elastic strain reaches its limit and plastic deformation occurs. In plastic deformation, stress is no longer proportional to strain. Plastic deformation in crystalline materials is primarily caused by dislocation slip and twinning. Plastic deformation is permanent – or not reversible – which means that when the applied load is removed, the material does not return to its original shape [47]. Yielding represents the onset of plastic deformation on a microscopic level. The position of the yielding point is difficult to measure precisely, so it is determined roughly by constructing a line parallel to the elastic portion of the curve, but offset to the right by a strain of 0.002. The intersection of this line and the stress–strain curve is

the yielding point. The stress value at the yielding point is the 0.2 % offset yield strength σ_y [47].

After yielding, stress continues increasing to the maximum on the engineering stress–strain curve, point M. The stress at point M is the tensile strength TS, representing the maximum stress that a structure can sustain in tension. Before point M, the deformation is uniform throughout the narrow region of the tensile specimen. Beyond point M, necking starts at some point of the specimen and all subsequent deformation is confined to this neck. As a result of necking after point M, stress decreases to eventual fracture at point F. The fracture strength is the stress value at which fracture occurs [47].

There are two basic types of fracture: brittle and ductile. For ductile materials, fracture occurs in the ductile mode. Ductile fracture is mediated by plastic deformation. For brittle materials, such as ceramics, no plastic deformation is possible [47]. The stress–strain curve for brittle materials only has the linear part of Figure 1-2 and fracture occurs before plastic deformation. A brittle-fracture process consists of the formation and propagation of cracks. Bulk semiconductor materials are brittle in nature, because dislocation activities are largely blocked by the ionic/covalent bonding in semiconductor materials. Therefore, they tend to fracture catastrophically in a brittle manner before any plastic deformation occurs.

When structural components, such as columns and bars, are subjected to uniaxial compressive load, they may either fail by crushing or buckling depending on whether they have a slenderness ratio (length/diameter) smaller or larger than their critical slenderness ratio. The value of the critical slenderness ratio varies and depends on the boundary conditions and materials. If the structural component has a slenderness ratio smaller than the critical slenderness ratio, failure occurs by either crushing for brittle materials, or yielding for ductile materials, when the compressive stress reaches the fracture strength or yield strength, respectively. If the structural component has a slenderness ratio larger than the critical slenderness ratio, buckling – or lateral deflection – occurs before the compressive stress applied on the structural component reaches the strength of the material, and finally failure associated with buckling occurs [48].

When a structural component is designed, fracture strength is used as the criterion to determine failure if – and only if – the component is always in static equilibrium when it is loaded. Otherwise, if buckling (lateral deflection) occurs, the critical buckling load will be used as the failure criterion. Critical buckling load is the maximum axial load that the structural component can support when it is on the verge of buckling. It causes the column to be in a state of unstable equilibrium, the introduction of the slightest lateral force will cause the column to buckle and therefore deflect laterally.

Buckling is geometric instability. Figure 1-3 presents a buckling load-displacement curve for a slender column subjected to an axial compressive load. The behaviour of an ideal column compressed by an axial load P is summarised below:

1. At the initial stage, the column is in the stable equilibrium state in the straight position. The load increases with the displacement, which corresponds to the initial increase between points 1 and 2 in the load-displacement curve.

2. At the critical buckling point ($P = P_{cr}$), which is point 2 at the load-displacement curve, the column is in a neutral equilibrium in either the straight or a slightly bent position.

3. After the critical buckling point, the column becomes unstable and starts to buckle, but does not suddenly collapse. Here, the load-displacement curve becomes flat.

4. Finally, the column fractures at point 3.

In 1757, Leonhard Euler derived a formula that gives the maximum axial load or critical buckling load that a long, slender, ideal column can carry without buckling. The formula is known as Euler buckling formula [49]:

$$P_{cr} = \frac{\pi^2 EI}{(KL)^2} \qquad \textbf{1-1}$$

where *Pcr* is critical buckling loading; E is the modulus of elasticity (later known as Young's modulus); I is the area moment of inertia of the cross section of the column; L is the original length of the column; K is column effective length factor, whose value depends on the boundary conditions of the end support of the column (K = 1.0

for both ends pinned, $K = 0.50$ for both ends fixed, $K \approx 0.699$ for one end fixed and the other end pinned, $K = 2.0$ for one end fixed and the other end free to move laterally). *KL* is the effective length of the column.

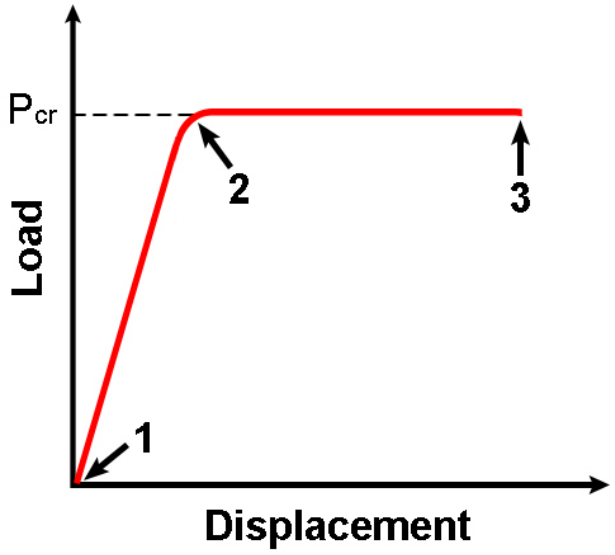

Figure 1-3 A typical buckling load-displacement curve for a slender column subjected to an axial compressive load.

1.4 Methods for testing the mechanical behaviours of nanomaterials

Several experimental and computational methods have been used to investigate the mechanical properties of nanomaterials. The experimental techniques differ from each other based on the mechanical properties measured and the platform used for the nanomechanical characterisation. Due to the small dimensions of nanomaterials, all nanomechanical characterisations of NWs have been conducted in one of the following types of microscopes: atomic force microscope (AFM), scanning electron microscope (SEM), and transmission electron microscope (TEM). Here, we categorise and review the existing experimental techniques for nanomechanical characterisation of nanomaterials from the literature, basing this on loading modes including bending, resonance, uniaxial loading, and nanoindentation. In addition,

computational calculations/simulations of the mechanical behaviours of nanomaterials are reviewed.

1.4.1 Bending

Bending tests of semiconductor NWs can be conducted in AFM, TEM, and SEM. There are two types of bending test: In the first, one end of individual NWs must be fixed and the other free, then load is applied at the free end to bend the NW using an AFM probe [50-55]. In the second, both ends of an individual NW is fixed, and load is applied at the middle point of the NW, which is termed "three-point bending" [56-62].

The first type of bending test is performed as follows: For NWs that are epitaxially grown perpendicular to the substrate, one end of the NWs is already fixed at the substrate, the testing can be easily conducted through applying a lateral force perpendicular to the NW axis at the free end of the NWs. This technique allows direct measurement of the mechanical properties of individual NWs without destroying or manipulating the sample. AFM is a major platform for the investigation of the mechanical behaviour of NWs. While AFM-based testing techniques enable direct measurement of force as a function of displacement from which the mechanical properties of NWs are extracted, the techniques are incapable of real-time imaging, which makes it difficult to interpret the *F–d* correlations to details of the structural evolution during NW deformation processes. *In situ* bending tests of NWs can also be conducted in TEM using a special TEM sample holder equipped with AFM/nanoindentation systems [63]. Thanks to the real-time high-resolution imaging capability of TEM, this method enables direct observation of the NW deformation process to understand the deformation mechanisms of NWs. Some bending tests conducted in SEM do not provide any *F–d* curve, however, the quantitative strength and strain values of NWs at fracture can still be calculated using three-dimensional finite element analysis (FEA) [50-52].

The three-point-bending method [56-62], in which a force perpendicular to the NW axis is applied at the middle point of a double-clamped NW, has also been used

in AFM to measure the mechanical properties of individual NWs. The *F–d* curve is recorded during the test. Using this method, the elastic modulus and yield strength of Au NWs with different diameters as small as 40 nm are measured [57]. This method has also been applied to the mechanical property measurement of other materials, including Si [56] and SiO_2 [59] NWs.

It is easy to perform bending experiments to measure the elastic modulus, fracture stress, and fracture strain of NWs because no complicated specimen preparation is needed and the testing can be completed in short time. However, the stress status of NWs under bending conditions is very complicated, with one lateral side under compression and the other side under tension. This makes it difficult to analyse the deformation mechanism of NW bending.

Although the above-mentioned methods enable direct measurement of the mechanical properties of NWs subjected to bending, they do not reveal the deformation mechanisms and dislocation activities of NWs that require real-time observation of the NW deformation at the atomic-level resolution. Han et al. developed a technique that enables *in situ* observation of the deformation process of individual NWs at the atomic scale [9, 64-69]. In this technique, NWs are sonicated off the substrate and dispersed in ethanol; they are then deposited on a TEM grid with a broken colloidal/carbon supporting film on the Cu grid. When the broken colloidal/carbon film is irradiated/heated by the electron beam, it undergoes shrinkage and applies bending or tensile force to individual NWs deposited on it. An intact colloidal/carbon film does not deform under the irradiation of electron beam. The experiment can be conducted in a high-resolution TEM (HRTEM) using a double-tilted holder so that individual NWs can be tilted to a specific zone axis for HRTEM imaging. Using this method, the mechanism of the unusually large plasticity in semiconductor NWs is revealed [64, 66, 67, 69]. The drawback of this method is that the strain rate and deformation mode of the NWs are normally uncontrollable.

Another way to investigate the atomic-scale mechanism of bending deformation of NWs is through an HRTEM, observing the dislocation activities of individual NWs that are deformed in an SEM using a manipulator and kept in the deformed status [10]. A typical deformation process of a NW is presented in Figure 1-4: one point at the NW is fixed on the TEM grid using electron-beam-induced

deposition of Pt (Figure 1-4a), followed by bending of the NW using the manipulator on one end of the NW (Figure 1-4b). The bending status of the NW is maintained through fixing the bent end of the NW on the TEM grid (Figure 1-4c). The bent NW is then observed at atomic scale in HRTEM.

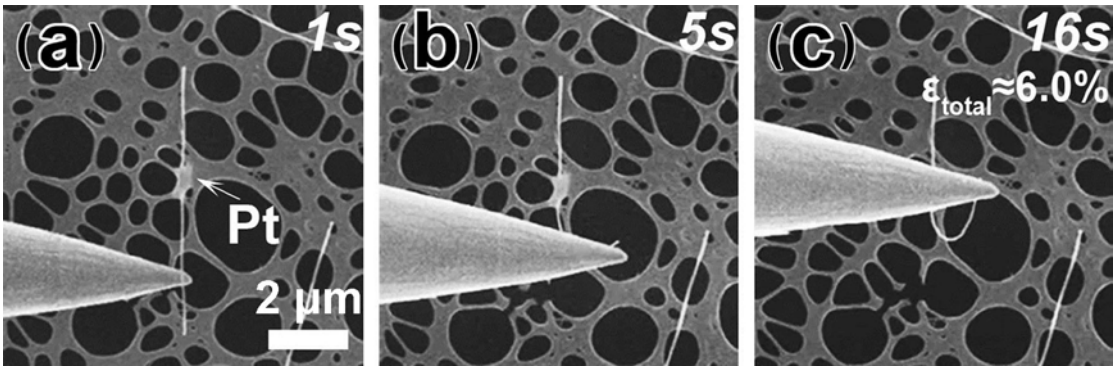

Figure 1-4 A series of SEM images showing a bending-deformation process of a NW. One end of the NW is fixed on the carbon film by the electron-beam-induced deposition of Pt. The other end is gradually bent by a manipulator. The top right corner of the images indicates the time-stamp (in seconds) during the experiment [10].

1.4.2 Resonance

The resonance method was first used in 1999 to characterise the mechanical properties of multi-walled carbon nanotubes [70], and has been applied to NW research [71-74]. The resonance method is based on the natural resonant vibration of a single cantilevered NW that is excited with an alternating current. The method can be used in TEM with a homemade TEM specimen holder that allows the application of electrical signals between the tip, to which the NWs are mounted, and a counter electrode [74, 75]. The application of a frequency-tuneable alternating current voltage across the tip and the counter electrode will drive the NW to vibrate mechanically, from which the resonance frequency is measured. Performing the experiment in TEM allows accurate measurements of the dimensions of the NWs and direct monitoring of the resonance. In addition to TEM, both SEM [72] and AFM [76] has also been used

for resonance experiments. While mechanical characterisation of NWs using the resonance method is straightforward, the only mechanical property that can be extracted from these experiments is the elastic modulus.

1.4.3 Uniaxial loading

Mechanical characterisation of NWs can also be performed by uniaxial tension and compression loading of a single NW in SEM or TEM.

Tensile tests in SEM can be performed by clamping one end of a NW to the tungsten tip of a nanomanipulator and the other end on an AFM cantilever using electron-beam-induced deposition. A tensile force is applied to the NW through the precision movement of the nanomanipulator, and the AFM cantilever works as the load sensor. The same experimental setup for tensile testing can be used for compression tests of individual NWs in SEM through moving the nanomanipulator towards the AFM cantilever in the opposite direction to apply compressive load to the NWs [13].

Deforming a NW in SEM using an AFM probe or nanomanipulator enables direct real-time observation of the structural changes during the entire process of the NW deformation. The large chamber size in SEM makes it easy to manipulate the NW deformation processes. However, it is difficult to reveal the deformation mechanisms of NWs during *in situ* testing in SEM because of the poor structural resolution of SEM. This problem can be overcome by conducting *in situ* experiments in TEM.

Recently, several commercial *in situ* TEM straining stages have been developed. The Hysitron PicoIndenter© and NanoFactory holders are the most commonly-used commercial products for *in situ* TEM tensile, compression, and bending tests [8, 77-87]. Some stages are able to provide quantitative stress–strain curves during the deformation, which is the basic requirement for mechanical property testing. *In situ* tensile testing in a TEM can be accomplished by coupling the PicoIndenter with a push-to-pull (PTP) device developed by Hysitron. This device has been used in a TEM to study the tensile strength of submicron-sized metallic glass

wires [88], the elastic properties and strain-induced phase transformation of individual VO_2 NWs [81], and dislocation activities in Mo alloy nanofibers [89]. Although these types of specially designed *in situ* straining TEM holders can provide quantitative stress–strain data, it is very difficult to use them for 2-D HRTEM imaging for the investigation of atomic-scale deformation mechanisms because the holders are usually single-tilt.

Han et al. have developed a method that allows 2-D HRTEM imaging during *in situ* uniaxial tensile deformation with controllable strain rate in TEM [90-95]. The working mechanism of the method is demonstrated in Figure 1-5. A specimen, which can be a NW, is attached to the edges of a trench between two bimetallic strips made of two materials that have different thermal expansion coefficients. When the strips are heated in a TEM heating stage holder with double-tilt capability, the bimetallic strips bend slowly in opposite directions, pulling the sample with an adjustable strain rate that is controlled by the temperature of the heating stage. While this method is excellent for the investigation of tensile deformation mechanisms at the atomic resolution, it does not provide any quantitative mechanical data. This technique can also be used to perform tensile tests of nanofilms. By using this technique, dislocation behaviour in a Pt ultrathin film with nanometre grains has been observed [91].

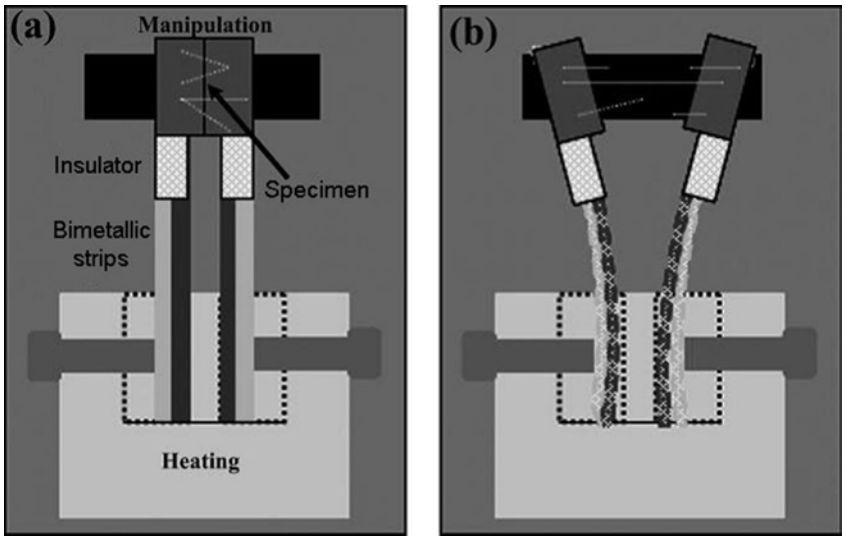

Figure 1-5 An illustration of the NW tensile testing technique using bimetallic strips. (a) Prior to the tensile test. (b) During the tensile test [90].

The stress state of the NWs under uniaxial tension is very simple, leading to easy interpretation of the measured mechanical data. However, mechanical characterisation of a single NW under uniaxial tension is very difficult. It requires a significant amount of specimen preparation due to the requirement to clamp NW samples to the testing stage (e.g., AFM cantilever, nanomanipulator, or PTP device). Characterisation of NWs using this method requires a great deal more time than the other methods.

1.4.4 Nanoindentation

One of the most commonly used techniques for the investigation of mechanical properties of nanomaterials, especially nanofilms, is nanoindentation. In this method, a nanometre-sized hard tip or nanoindenter is pressed into a sample by applying a small force. Young's modulus and hardness – resistance to permanent or plastic deformation – of the sample is measured from the test. Nanoindentation has been widely used in AFM for mechanical characterisation of nanofilms [96, 97], nanobelts [98, 99] and NWs [100-102]. Hardness and Young's modulus were extracted from the *F–d* curve obtained by nanoindentation. Nanoindentation hardness can be calculated from the following equation:

$$H = \frac{P_{\max}}{A} \qquad \textbf{1-2}$$

where P_{max} is the indentation load (the peak load from the *F–d* curve) and *A* is the projected contact area of the indentation. The Oliver–Pharr data analysis procedure [103] is used to calculate the elastic modulus.

1.4.5 Computational approaches

Experimental measurements are essential to investigate the mechanical behaviours of nanomaterials. However, due to the difficulty of sample handling, the sensitivity limits of testing facilities, and the inability to decouple the mechanical

properties of thin films from those of their underlying bulk substrates, it is very challenging to conduct experimental measurements for nanomaterials such nanowires and nanofilms with relatively small dimensions (no more than ~ 20 nm). Moreover, it is difficult to explore the deformation mechanisms of nanomaterials at atomic scale through experimental techniques. Computational methods are helpful in the investigation of the deformation behaviour of nanomaterials because they enable the real-time observation of the deformation at the atomic scale and, at the same time, provide stress–strain curves [104-107]. Two major computational approaches are molecular-dynamics (MD) simulations and first-principles calculations. Theoretical approaches have some unavoidable limitations, as the results obtained from computational methods depend strongly on the parameters and theoretical functions used. Due to the computational limitations, theoretical calculations have only been used to study NWs with relatively small diameters, usually below 20 nm [105, 106, 108, 109]. Moreover, the strain rates applied in simulations are very high, usually 10^{8} s^{-1} [105, 106], which is much higher than the strain rate of ~10^{-4} s^{-1} applied in experiments [12, 65, 66].

1.5 Mechanical behaviours of nanomaterials

1.5.1 Young's modulus

For bulk materials, Young's modulus is an intrinsic property of materials, and is fundamentally independent of the dimensions of the materials. However, the Young's modulus of a low-dimensional nanomaterial is very different to that of its bulk counterpart, and is also size-dependent. The size dependency of Young's modulus is important for the applications of nanomaterials and, therefore, has attracted a great deal of attention from researchers.

The Young's modulus of ZnO NWs has been extensively investigated by many research groups because of the significant potential applications of ZnO NWs [13, 53, 61, 72, 110-121]. Results have been significantly scattered. For example, AFM lateral bending experiments demonstrate that the Young's modulus of ZnO NWs with an average diameter of 45 nm is 29 ± 8 GPa [53], which is significantly

lower than the bulk value (~ 140 GPa); a much larger Young's modulus of 220 GPa for ZnO NWs with a diameter of 17 nm was obtained from electric-field-induced resonance measurement [72]. A report has also demonstrated that the Young's modulus of ZnO NWs with diameters ranging from 18 nm to 304 nm is close to the bulk value [61].

In addition to the scatter of the value of Young's modulus of ZnO NWs, there is no consensus on the size effect on the Young's modulus. Some reports have claimed that the Young's modulus of ZnO NWs is essentially independent of NW dimensions [61, 122], while others have found that the Young's modulus of ZnO NWs decreases with decreasing diameters [113]. However, most studies have supported the conclusion that the Young's modulus of ZnO NWs increases dramatically with decreasing diameter [52, 72, 112, 115, 119]. For example, the Young's modulus of ZnO NWs increases from 140 GPa to 210 GPa when the diameter decreases from 550 nm to 17 nm [72]. The same trend on the size effect on Young's modulus has also been reported in GaAs NWs [8].

Similar to ZnO NWs, significant discrepancy in the experimental results on the size effect on Young's modulus also exists for Si NWs [108, 109, 123-127]. The sources that lead to the discrepancy are not clear but experimental errors could be a reason. The different techniques used for mechanical testing are also a possible reason for the discrepancy. For example, NW surface carries more stress in flexural-loading conditions (i.e., resonance and bending) than in uniaxial loading conditions; as such, the surface has a greater effect on the Young's modulus of NWs under resonance and bending than under tension. Loading misalignment of NWs, which can be quantified based on the misalignment angle between the loading direction and the NW axis, is usually unavoidable in mechanical property testing of NWs. Unfortunately, loading misalignment has been ignored in many investigations, which leads to underestimation of the Young's modulus. A misaligned load can be resolved into two components F_x and F_y, which represent the force perpendicular and parallel to the NW axial direction, respectively. For a compression test, F_x can generate a bending moment to buckle the NW. Compared to uniaxial compression, a smaller force is needed to buckle a NW with loading misalignment due to the bending moment. Most epitaxially grown NWs are tapered rather than straight-edged because NW bases are grown first, and hence are exposed to reactants for a greater length of time than the

later grown tips [128]. Ignoring the NW tapering during the data analysis of NW tensile or compression tests results in inaccuracy of the measured Young's modulus because the inaccurate cross-sectional area of the NW is used. In addition, for a technique that needs information on materials density, such as the resonance method, the density of bulk materials could be used. However, if native oxides form on the surface of NWs, the density changes, which becomes a source of the error. Combined detailed structural characterisation at the atomic scale and careful mechanical testing would provide more information on the sources of the discrepancy.

Several mechanisms have been proposed to explain the size effects on the Young's modulus of NWs, including bulk nonlinear elasticity [129, 130] and surface reconstruction [13, 72, 112, 115, 119]. The dependency of Young's modulus on the dimensions of materials has been observed in high-quality single-crystal NWs with few defects [8, 13, 72, 112]. Therefore, it is expected that the phenomenon of size-dependent Young's modulus originates from surface reconstruction of NWs. Young's modulus is very sensitive to interatomic distance. Atomic reconstruction on the surface of materials usually decreases the interatomic spacing on the surface, leading to the surface-stiffening effect [131]. The difference between the Young's moduli on the surface and in the bulk does not affect the overall Young's modulus for bulk materials. However, this difference significantly affects the Young's modulus of NWs due to their large surface-to-volume ratios. By assuming a NW with a diameter of D having a core–shell structure composed of a core with modulus (E_0) of the bulk material, a surface shell layer with constant thickness (r_s), and a surface modulus (E_s) higher than the bulk value, a core–shell model has been proposed to calculate the effective Young's modulus (E) of the NW [72]:

$$E = E_0\left[1+8\left(\frac{E_s}{E_0}-1\right)\left(\frac{r_s}{D}-3\frac{r_s^{\,2}}{D^2}+4\frac{r_s^{\,3}}{D^3}-2\frac{r_s^{\,4}}{D^4}\right)\right] \qquad \textbf{1-3}$$

A combined experimental/simulation study proposed that the effect of surface reconstruction rapidly decays beyond a certain number of atomic layers, and the number of these atomic layers increases with increasing the NW diameter [115]. It is suggested that the shell thickness is not constant and remains ~ 15% of NW diameters ranging from 20 nm to 80 nm, which is in contrast to the assumption made in the core–shell model [72].

Based on a continuum-mechanics approach that describes the surface effect of NWs under tension and bending, a core–surface model [132] was established to calculate the effective Young's modulus (E) of NWs with a diameter of D. In the model, a NW consists of a core with elastic modulus E_c and a surface with zero thickness and surface elastic modulus S (the unit is Pa•m). The effective Young's modulus E is given by the following:

$$E = E_c + 4\frac{S}{D} \text{ under tension, and} \quad \textbf{1-4}$$

$$E = E_c + 8\frac{S}{D} \text{ under bending.} \quad \textbf{1-5}$$

The surface-reconstruction mechanisms, including the core–shell and the core–surface models, are experimentally confirmed and well accepted [13]. However, some studies explain the size effect through bulk nonlinear elasticity, in which the residual tension-stiffened interior atomic layers are the main contributor to the size effect [129, 130]. This explanation is drawn from theoretical studies without support from experimental data.

Theoretical simulations have also been widely used to investigate the size effect on the Young's modulus of NWs [104, 106, 108, 109, 133-136]. However, computational data has presented some discrepancies from the experimental results. For example, computational results demonstrated that the Young's modulus of Si NWs begins to deviate from that of bulk Si only when the diameter of the Si NWs is less than 10 nm [104, 108, 109, 133, 137]. However, experimental results indicate the transition diameter is approximately 30 nm [125]. Due to the computational limit, theoretical simulations have only been used to investigate the size dependency of NWs with diameters smaller than 15 nm. In contrast, due to the difficulty of sample handling and the sensitivity limit of testing facilities, most experimental results have come from NWs with diameters larger than 15 nm. The dimension gap between experimental results and computational predictions makes the comparison of the experimental results and computational predictions difficult.

By using the computational methods, it has also been revealed that the Young's modulus of ZnO nanofilms [130, 138] and nanobelts [129] is size-dependent,

and the value differs from that of bulk ZnO when the thickness was below 8 nm and 4 nm, respectively. Theoretical investigations also revealed that the effect of size on the mechanical properties of nanomaterials depends strongly on the specific material properties. In some situations, opposite effects were predicted. For example, the Young's modulus of ZnO films was expected to increase by ~ 22% with decreasing thickness from 8 nm to 1 nm[130, 138], whereas the Young's modulus of Cu films has been predicted to decrease when the thickness of the film decreases from 12 nm to 1 nm.[139, 140]

1.5.2 Elastic strain

Ceramic materials are naturally hard but brittle at room temperature. They usually fracture in the brittle mode with little (< 0.1%) or no plastic strain [47]. However, large elastic strains in semiconductor NWs have been widely reported (Table 1-1) [8, 10, 51, 52, 65, 66, 141, 142]. In Table 1-1, the fracture strain of a NW is either the same as the elastic strain or equal to the sum of elastic strain and plastic strain, depending on whether the fracture is brittle or ductile. MD simulations have demonstrated that the tensile elastic strain of SiC NWs with a radius of 0.432 nm at room temperature can be as high as 8.9% [141]. Large elastic strains in semiconductor NWs have been experimentally confirmed. The elastic strain of SiC and Si NWs can be as high as ~ 2% [66] and 10% [142], respectively. The elastic strain in brittle fracture of ZnO NWs measured by two research groups was 7.7 ± 0.8% [52] and 4–7% [51].

Combined *in situ* compression in TEM and FEA has been used to study the fracture strain of GaAs NWs [8]. The failure strain is 11.3%, which is approximately 100 times higher than the bulk value. Brittle fracture with fracture strain remaining at 10–11% for NWs with diameters in the range of 50 nm to 150 nm was observed, indicating that the high elastic strain could be an intrinsic material property. Recently, another study on GaAs NWs also revealed the development of high elasticity, with an elastic strain up to 3.16%, during a bending-deformation process of GaAs NWs with a diameter of ~ 50 nm [10].

Table 1-1 Elastic, plastic, and fracture strain of semiconductor NWs.

Material	Loading	Fracture	Elastic Strain (%)	Plastic Strain (%)	Fracture Strain (%)
GaAs [8]	Compression	Brittle	11.3	-	11.3
Si [142]	Tension	Brittle	10.0	-	10.0
ZnO [52]	Bending	Brittle	7.7	-	7.7
ZnO [13]	Tension	Brittle	6.1	-	6.1
GaAs [10]	Bending	Ductile	3.16	0.99	4.15
SiC [66]	Bending	Ductile	2.0	1.5	3.5
SiC [141]	Tension	Ductile	8.9	46.0	54.9
Si [67]	Bending	Ductile	-	-	21.5
Si [65]	Tension	Ductile	-	-	125.0
Ge [143]	Bending	Ductile	-	-	17.0
SiC [90]	Tension	Ductile	-	-	200.0

A fracture process involves two steps: crack formation and propagation. For brittle materials, cracks usually initiate at microscopic flaws or imperfections that exist at the surface and within the interior of the materials. These flaws significantly reduce the fracture stress and fracture strain because an applied stress may be amplified or concentrated at the tip of the flaw, which makes the material fracture at a strain far below its elastic limit. It is well known that with the reduction of materials' dimensions, the probability of the existence of a flaw in materials decreases. The fracture strain of semiconductor NWs with no pre-existing defects is expected to be a great deal higher than that of their bulk counterparts because the mechanism of crack initiation by flaws is absent. The NW has a core–shell structure, comprising a perfect crystalline core without any defect and an amorphous surface around the core, and the amorphous/crystalline interface is smooth. All of these factors indicate that crack initiation in such a NW would be difficult due to a lack of crack-initiation sites. Therefore, superelasticity was observed in GaAs NWs [144].

These results clearly demonstrate that semiconductor NWs can sustain elastic strain that is approximately 100 times higher than that of their bulk counterparts due to the diminished number of defects in the NWs. Many physical and chemical properties of materials are closely related to the interatomic distances of neighbouring atoms. Elastic straining could alter the electronic structure [145], band gaps [146-149], thermal transport [150, 151], and electro-optical [152, 153] properties of materials. Unfortunately, no large elastic strain can be applied to bulk materials because pre-existing defects in the bulk materials would lead to plastic deformation or fracture at very small elastic strain. Tuning the physical and chemical properties through elastic-strain engineering can only be achieved in nanomaterials. In fact, elastic-strain engineering has been widely applied to commercial semiconductor products. For example, strained silicon technology [154-156] has been widely used to improve the mobility of charged carriers (more than 50% improvement in response to tensile elastic strain of ~ 1%) [156] and electrical conductivity (a compressive elastic strain of 0.4% doubles the conductivity) [157].

1.5.3 Anelasticity

Anelasticity has been observed in polymers [158], metallic alloys [159, 160], polycrystalline ceramics [161], and bulk metallic glasses [162]. The underlying mechanisms of the anelasticity in different materials are different. For example, phase transformations, reversible motion of twins, grain reorientation, and cooperative motion of many atoms at grain boundaries are the dominant mechanisms for the anelasticity in Cu-Al-Ni alloys [160], In-Ti alloys [159], yttria-stabilised zirconia [163], and nanocrystalline Au [164], respectively. Note that none of these materials is a single crystal, and the polycrystalline feature of these materials is a key factor for anelasticity.

A recent investigation demonstrated that single-crystal GaAs semiconductor NWs with small diameters (e.g., 25 nm) demonstrate anelasticity [84]. However, anelasticity was not observed in GaAs NWs with large diameters (55 nm). As demonstrated in Figure 1-6a, a GaAs NW with a diameter of 25 nm presented uniform contrast in TEM. Compression led to bending of the NW and bending contour,

indicated with arrows in Figure 1-6b, presented along the NW. Upon load release of the NW (Figure 1-6c), the bending contour did not disappear immediately, indicating no instantaneous full recovery of the elastic strain. In fact, it took close to two minutes for the NW to recover gradually to its original shape (Figure 1-6d–f). Structural characterisation of the NWs revealed the reason for the anelasticity. Figure 1-7 presents a typical HRTEM image of a GaAs NW with SFs; an amorphous native-oxide layer covers the surface of the GaAs NW. The atomic bonding at the interfacial region may not be as strong as that inside the NW crystal, therefore, after the same displacement, the residual stress and relaxation time of the amorphous surface layer

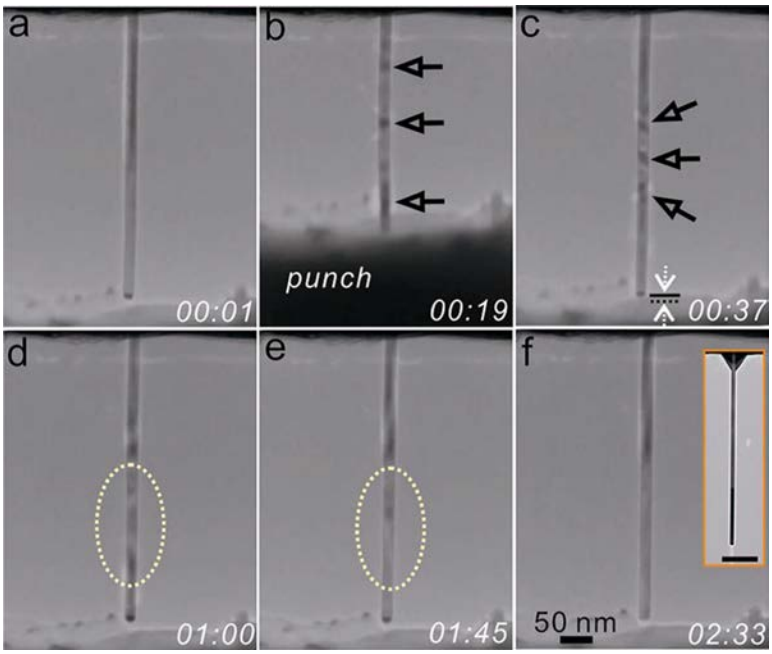

Figure 1-6 A series of TEM images showing the anelastic behaviour of a GaAs NW with a diameter of ~ 25 nm. (a) Before deformation. (b) During deformation with arrows indicating the bending contours. (c) Immediately after the external stress was completely removed. The gap between the two dotted arrows is the difference between the current and original positions of the NW tip. (d, e) The NW gradually returned to its original shape. Dotted ellipses mark the region for contrast comparison. (f) The NW completely recovered to its original shape. The inset in (f) presents the whole length of the NW. The scale bar in the inset image is 200 nm [84].

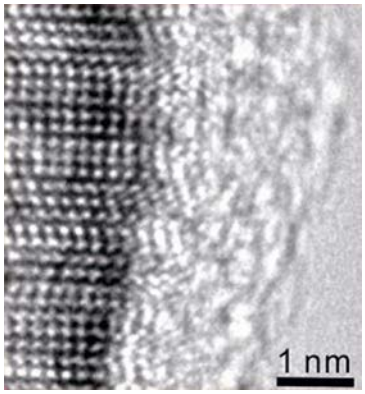

Figure 1-7 A typical atomic-resolution TEM image of the interface in a NW with SFs [84].

and the crystal core of the NW are different during the unloading process. When the external stress is removed, the whole NW gradually returns to its original shape with a time delay, since the amorphous layer holds back the crystal core resulting in a slow recovery. Anelasticity in GaAs NWs with small diameters was attributed to the interfacial effect between the amorphous layer and the crystalline core. Therefore, the interfacial structure, which was closely related to the defects in the NWs, plays a crucial role in determining the anelasticity of the NWs. The interfacial effect would no longer dominate the mechanical behaviour of NWs with large diameters due to the significantly decreased surface-to-volume ratio. As such, no anelasticity was observed in NW with large diameters. In addition to GaAs NWs, single-crystalline ZnO NWs with diameters ranging from 38 nm to 65 nm released from bending strain were also reported to exhibit anelastic behaviour [165]. The large anelasticity in ZnO NWs is due to the stress-gradient-induced diffusion of point defects, i.e., oxygen vacancies diffuse from the tensile to the compressive side and zinc interstitials diffuse in the opposite direction. These findings open up the prospect of using semiconductor NW materials for nanoscale damping applications.

1.5.4 Plastic strain

The mechanical behaviours of nanomaterials can be different from that of their bulk counterparts. For example, although Si is nominally brittle, ductility was

reported in Si nanopillars below a critical diameter, between 310 nm to 400 nm [166]. Bending deformation of a SiC NW resulted in a failure strain of ~ 1.5%, and this has been achieved through increasing dislocation density, atomic lattice disordering, and amorphisation [64]. Unusual large plastic bending strain (no quantitative strain value was provided) of SiC NWs has been observed through *in situ* deformation HRTEM at close to room temperature [66]. Superplasticity of SiC NWs with > 200% elongation has been observed in the 3C structure of SiC by *in situ* axial-tensile experiments in SEM [90]. Large plastic strains have also been observed in Si NWs under bending [67, 69] and tensile [12, 65] stress. It has been demonstrated that Ge NWs tolerate diameter-dependent flexural strains of up to 17% before fracture, and the crystalline NW structure transforms to an amorphous structure at the maximum strain [143]. ZnO NWs have also been found to demonstrate a crystal-to-amorphous transition in highly compressed regions after a number of loading and unloading cycles [119]. A summary of the fracture modes and failure strain, including the values of plastic strain in some cases, is listed in Table 1.

Due to the existence of flaws in bulk ceramic materials, ceramics usually fracture at a stress lower than the critical resolved shear stress, which is the minimum resolved shear stress required to initiate dislocation-mediated plastic deformation [47]. However, when the dimensions of ceramic materials reduce to a small scale, defect-free structures can be obtained, which makes it possible for the materials to sustain high strain and high stress before fracturing. This stress could be high enough to overcome the critical resolved shear stress and supply sufficient energy to nucleate and/or move glissile dislocations. In addition to the defect-free structures, the high surface-to-volume ratios in NWs could also be responsible for the development of plasticity because the surface of the NWs provides abundant dislocation-nucleation sites, and much lower stress is required for dislocation nucleation at the surface than dislocation self-multiplication within crystals [167, 168].

HRTEM investigations of the bending deformation of Si NWs has revealed the atomic mechanisms of large plastic strain in semiconductor NWs [69]. During bending deformation, prevalent mobile full dislocations nucleate, interact, and form Lomer lock dislocations. A typical example of the process is presented in Figures 1-8a–d. A dislocation with a Burgers vector of b = 1/2[011] is shown in Figure 1-8a

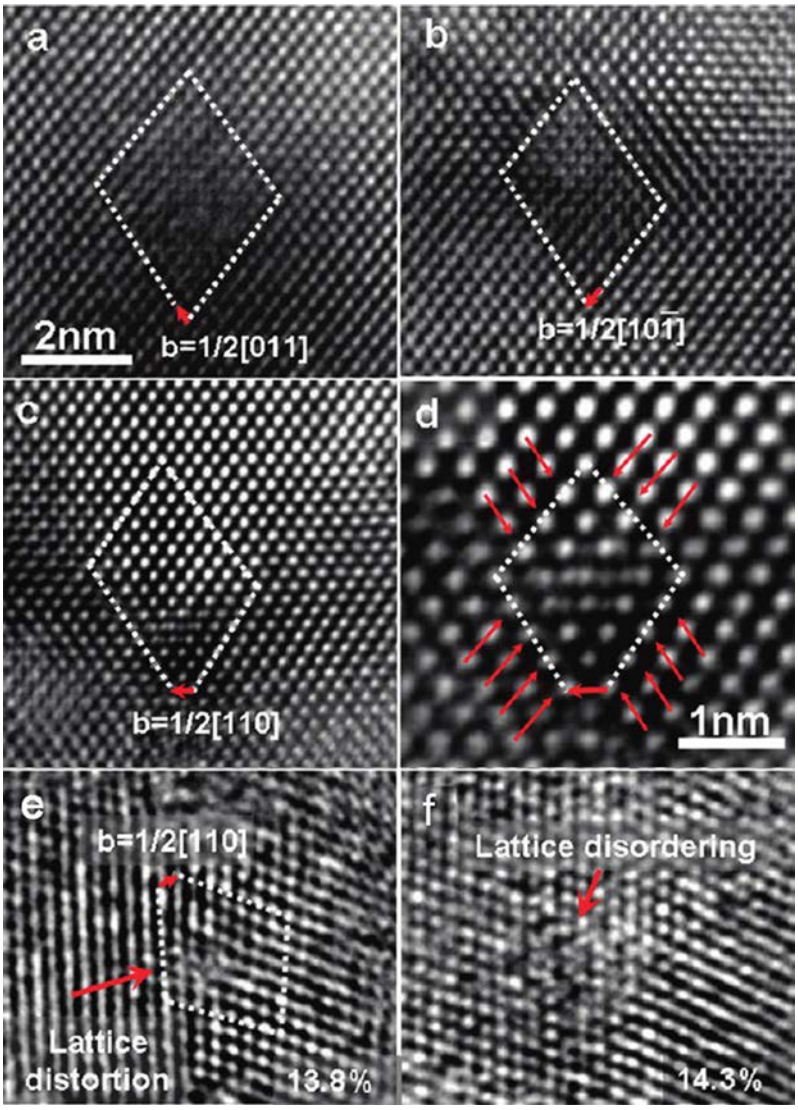

Figure 1-8 An atomic-scale *in situ* observation of a Lomer lock dislocation–formation process via a dislocation reaction and the subsequent crystalline to amorphous transition. (a, b) A glissile dislocation with a Burgers vector of b = 1/2[011] and 1/2[$10\bar{1}$], respectively. (c) A Lomer lock dislocation formed via the reaction of the two dislocations shown in (a) and (b). (d) An enlarged HRTEM image showing the Lomer lock structure. (e, f) Enlarged HRTEM images showing a crystalline to amorphous transition process at the atomic scale [69].

and another dislocation with a Burgers vector of b = 1/2[$10\bar{1}$] is presented in Figure 1-8b. These two types of dislocations can react and form a Lomer lock dislocation (Figure 1-8c). An enlarged HRTEM image of the Lomer lock structure is presented in Figure 1-8d. Figures 1-8e–f present two HRTEM images taken from the same region

at different strain values, demonstrating that continuously increasing bending strain results in atomic disorder at the core of a Lomer lock that eventually transforms the local area into an amorphous structure. These results clearly demonstrate that ultralarge plasticity in some semiconductor NWs is caused by extensive dislocation activities and a crystal-to-amorphous phase transition.

Controversial results have also been reported for the deformation behaviour of semiconductor NWs. Many studies have demonstrated that semiconductor NWs are brittle and have not observed any noticeable plastic deformation before catastrophic fracture under both uniaxial tension and bending. For example, both bending tests [50, 124, 169] and tensile deformation [12, 125, 170, 171] of Si NWs demonstrated only brittle fracture. Figure 1-9a presents a typical *in situ* tensile test on a Si NW using a TEM–AFM platform [12]. An HRTEM image of the fracture surface is presented in Figure 1-9b. The fracture is brittle by cleavage along the (111) planes. The fracture surface is flat and perpendicular to the loading direction without any obvious necking or sliding. A typical stress–strain curve in Figure 1-9c demonstrates a linear elastic deformation before an abrupt drop in the stress caused by failure. ZnO NWs have also been found to deform elastically until brittle fracture under bending [51, 52, 61].

The fact that different or contradictory results have been reported indicates that the mechanical behaviours of semiconductor NWs are complicated and depend on many factors, including strain rate, loading condition, sample size, sample orientation, and sample defects. The mechanical behaviours of materials (e.g., brittle-to-ductile transition) are sensitive to the strain rate [172, 173]. The critical brittle-to-ductile transition temperature increases with increasing strain rate. Large plastic strain is usually obtained at a low strain rate, for example, Si NWs under bending or tension with a strain rate of approximately 10^{-5} s^{-1} [65, 66], and Ge NWs under bending with a strain rate of 10^{-3} s^{-1} [143]. Higher strain rates might result in brittle fracture. Much faster loading with a constant displacement of 20 nm/s has been used to compress GaAs NWs for the whole cycle distance of ~ 150 nm, and brittle fracture was observed [8]. Similarly, Si NWs have demonstrated brittle fracture when bent at a speed of 10 nm–30 nm for a distance of 100 nm–300 nm [124].

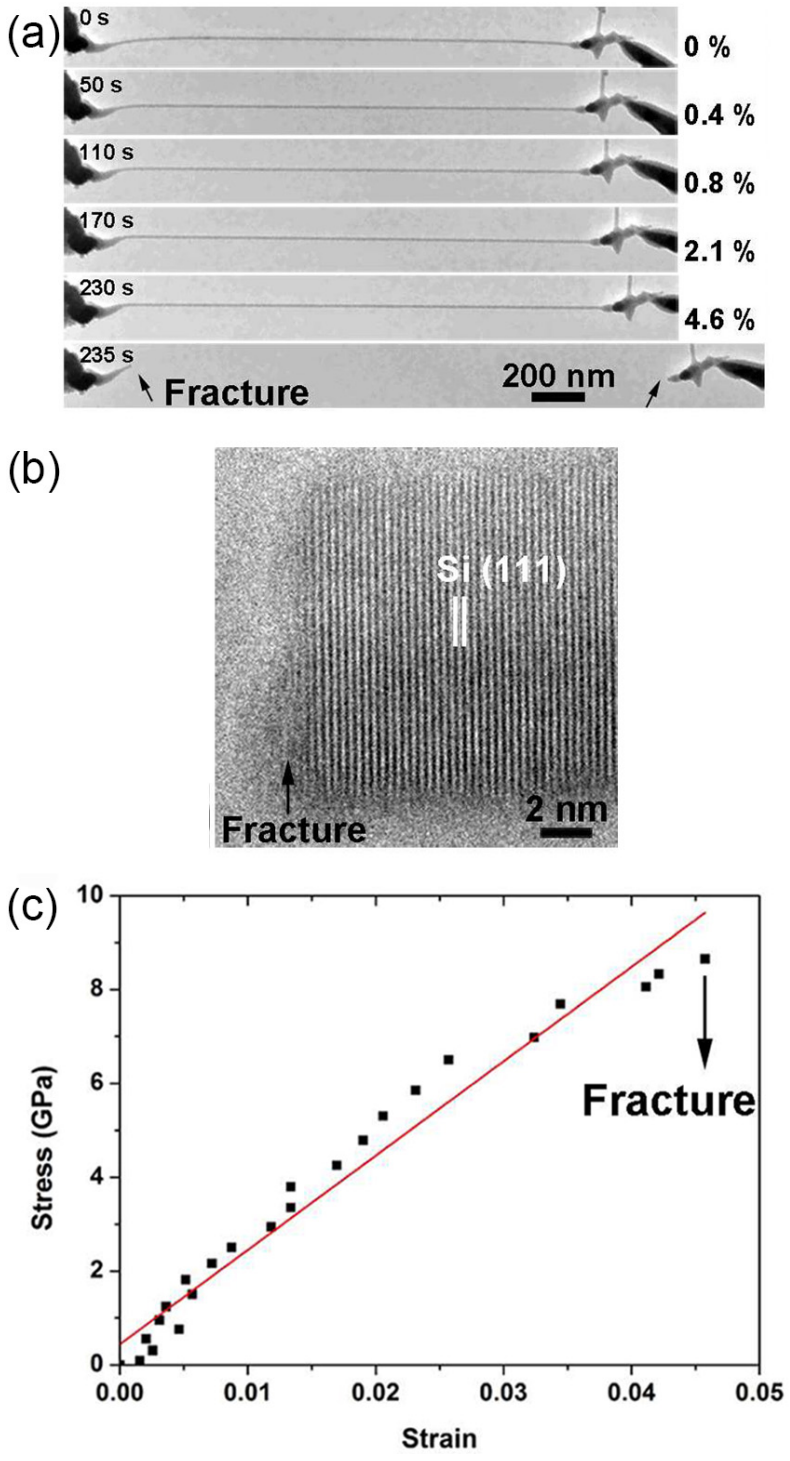

Figure 1-9 An *in situ* TEM tensile test of a single Si NW. (a) Snapshots of the tensile elongation and fracture process. Uniform elongation occurred until simultaneous abrupt fracture at two positions. (b) An HRTEM image of the Si a NW at fracture site. (c) Typical stress−strain curve illustrating a linear elastic deformation until abrupt failure with the values of fracture stress and strain of 8.7 GPa and 4.6%, respectively [12].

Under different loading conditions, stress states are different and therefore might result in different mechanical behaviours. A stress-state parameter (α) of the ratio between the maximum shear stress and the maximum axial-tensile stress can be defined to describe the influence of the stress state on the ductility of a material: $\alpha = (\tau_{max})/(S_{max}) = (\sigma_1 - \sigma_3)/(2[\sigma_1 - \nu(\sigma_2 + \sigma_3)])$, where τ_{max}, S_{max}, $\sigma_{1,2,3,}$ and ν are the maximum shear stress, maximum tensile stress, three principal stresses, and Poisson's ratio, respectively [174]. The α value for uniaxial tension and compression states is ~ 0.5 and ~ 2, respectively. Materials tend to be more brittle with a smaller α value, so materials are usually more brittle under tension than under compression. Si NWs fractured in a brittle manner under tension but pronounced plastic deformation by dislocation activities and crystalline to amorphous transition occurred under bending [12]. The diameters of NWs have important influences on the mechanical behaviours of NWs. It has been proposed that the plasticity of a particular material is controlled by the dislocation velocity, which is regarded as the rate of emission of dislocations and/or dislocation motion [65]. The dislocation velocity is diameter-dependent. NWs with a small diameter have a high dislocation velocity and tend to be ductile. Further, MD simulations have suggested that materials' dimensions are critical in determining the fracture mode. For example, Si NWs [107] and ZnO NWs [175] could fracture in either brittle or ductile manners under tension, depending on their diameter. For example, under a bending condition, brittle fracture was observed for Si NWs with diameters in the range of 100 nm to 700 nm [124] and ductile deformation presented in Si NWs with diameters between 15 nm to 70 nm [65]. The mechanical behaviours are also closely related to NW orientations (growth directions). It has been found that Si NWs with [111] growth directions are more brittle than those with [110] growth directions [104, 107]. Defects such as surface steps or twin boundaries may act as stress concentrators and initiation sites for cracks, facilitating a brittle fracture [12, 124], while ductility may be observed in a defect-free NW [65]. In addition, experimental conditions, such as electron-beam irradiation[176], NW clamping and loading alignments could also affect the mechanical behaviours of NWs.

In bulk materials, plastic deformation is nonrecoverable or permanent. However, reversible plasticity has been observed in GaAs NWs during bending-deformation processes [10]. The reversible plastic deformation is accompanied by large elastic strain and occurs from an early stage of bending deformation until failure.

As presented in Figure 1-10a and the inset selected area electron diffraction (SAED) pattern, a high density of dislocations was found across a bent NW. After the release of the bending stress, the dislocation density in the recovered NWs reduced dramatically (Figure 1-10b). The results indicate that upon load release, both the lattice-based elastic deformation and the dislocation-based plastic deformation recovered. In this study [10], the NWs were deformed to different strain levels. It was found that both elastic and plastic strain components increase with the increase of the total strain, indicating that plastic strain develops in parallel with elastic strain throughout the whole deformation range.

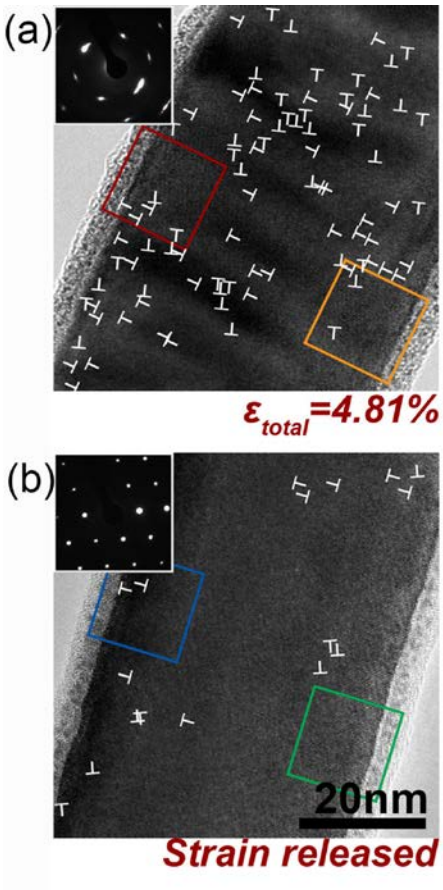

Figure 1-10 The microstructural evolution of a GaAs NW during a bending–release process. (a) An HRTEM image and a corresponding SAED pattern of a NW deformed 4.81% show a very high density of dislocations. (b) An HRTEM image of the NW following release of the applied load. The inset SAED pattern is identical to that of the undeformed sample [10].

It is known that NW has very high surface-to-volume ratio, and the surfaces of NWs provide abundant sources for dislocation nucleation and act as the sink for dislocation annihilation. Hence, during the bending deformation of a NW, a very high density of dislocations nucleates from the surface of the NW. For bending deformation of a NW, the stress status changes from tension at one side of the NW to compression at the other side. There is a transition zone somewhere around the geometric axial centre of the NW with zero stress. Such a zero-stress area acts as a barrier to prevent dislocations from passing through the whole NW. Consequently, the tangling of dislocations results in significant work hardening, leading to a very rapid increase in flow stress and further increases in significant elastic strain after the initiation of plastic deformation. When the load is removed, the recovery of elastic strain produces large internal stress, which is opposite in direction and approximately equivalent in magnitude to the applied stress. This internal stress spontaneously drives the dislocation motion backwards and, finally, most of the dislocations annihilate at the NW surface from which they nucleate. Therefore, the plastic strain is recovered through the reverse motion of the dislocations.

1.5.5 Fracture strength

The measured fracture strengths of most materials are significantly lower than the theoretical prediction calculated based on atomic-bonding energy. This is caused by the unavoidable defects (e.g., dislocations and cracks) in materials that serve as sources for crack formation and propagation. When the dimensions of materials are reduced to the nanometre regime, a structure with few or no internal defects could be obtained that would provide the ability to sustain high stress before failure. Therefore, the fracture strength of semiconductor NWs could be much higher than that of their bulk counterparts (Table 2).

The fracture strength of SiC NWs was first measured by the Lieber group in 1997 using AFM-based bending tests [177]. The group reported that the maximum fracture strength of SiC NWs was 53.4 GPa, which is much larger than the corresponding values for bulk SiC and microscale SiC whiskers. The fracture strength of Si NWs increased from 5.1 GPa to 12.2 GPa as the NW diameter decreased from

Table 1-2 Fracture strength of semiconductor NWs and their bulk counterparts.

Material	Diameter (nm)	Loading Mode	Fracture Strength (GPa)	
			NW	Bulk
SiC	35	Bending	53.4 [177]	0.8-1.5 [47]
SiC	50	Compression	5.4 [85]	0.8-1.5 [47]
Si	15	Tension	12.2 [125]	0.3-1.0 [178]
Si	100	Bending	18.0 [50]	0.3-1.0 [178]
ZnO	220	Bending	7.7 [52]	0.1 [179]
ZnO	20	Tension	10.32 [13]	0.1 [179]
Ge	23	Bending	18.0 [143]	0.13-0.15 [143]
GaN	200	Tension	7.0 [180]	-

60 nm to 15 nm [125]. Such a size effect on fracture strength was related to the reduced numbers of defects in NWs with smaller diameters. This study also revealed that the strength of Si NWs increased with decreasing the side surface area of Si NWs, which confirmed the importance of the surface defects in fracture. Similar results have also been reported for the tensile fracture strength of Si NWs [12, 171]. However, no clear size effect was discovered for the bending fracture strength of Si NWs [50, 124]. For example, the bending fracture strength of Si NWs with diameters of 90 nm to 140 nm was found to be in the range of 7 GPa to 18 GPa without showing a clear size effect [50]. Using a microelectromechanical systems testing stage, the tensile fracture strength of GaN NWs was measured to be in the range of 4 GPa to 7 GPa [180]. Ultrahigh strength of the ZnO NWs under tension is size dependent. It is believed that, in addition to the diminished number of defects in small NWs, surface strengthening also contributes to the size effect of the fracture strength [13]. Structural reconstruction on materials' surface leads to reduced bond length and this strengthens the materials on the surface. Reducing the dimensions of NWs increases the surface-to-volume ratio of the NWs, and therefore leads to higher fracture strength.

Grown-in defects in bulk materials, including dislocations and cracks, are a major factor in reducing the strength of materials. Interestingly, a recent investigation proposed that GaAs NWs could be strengthened through defect engineering [85]. This strengthening effect was attributed to the higher Young's modulus values of the NWs with a high density of SFs, which made the NWs more resistant to bending and better able to suppress crack initiation. Most recently, *in situ* tensile tests in SEM of SiC NWs consisting of segments with the 3C structure, the 3C structure with an inclined SF, and a highly-defective structure in a periodic fashion along the NW length [181], demonstrated that the NWs fractured in the 3C with inclined SF segments, rather than in the highly-defective segments. A strong size effect on the fracture strength was observed (Figure 1-11a). As presented in Figure 1-11b, reducing the diameter of SiC NWs reduces the density of defects in the NWs and this increases the fracture strength of the NWs. Therefore, the size effect in this study was due to the size-dependent defect density.

1.5.6 Fatigue

Fatigue is a form of delayed failure that occurs in materials subjected to cyclic loading. Similar to the fracture of materials under static loading, the process of fatigue begins with crack initiation, in which a small crack forms at some point of high stress concentration, followed by crack propagation, during which the crack advances incrementally with each stress cycle. Finally, failure occurs rapidly once the advancing crack has reached a critical size. The applied stress is amplified at a crack tip to the degree that the local stress level exceeds the yield or fracture strength. Therefore, failure occurs in materials even if the maximum applied stress in each stress cycle lies below the yield or fracture strength. Fatigue is catastrophic and insidious, occurring suddenly and without warning. For semiconductor NWs, fatigue is important inasmuch it is a commonly encountered failure mode that determines the stability and lifetime of NW-based devices [182]. However, performing a fatigue experiment on a NW is very difficult due to the small size of the NW, and the experiment is very time-consuming because it usually requires ~ 10^8 loading cycles

[47]. So far, only the fatigue behaviours of ZnO NWs have been studied due to their piezoelectric property-related applications [182, 183].

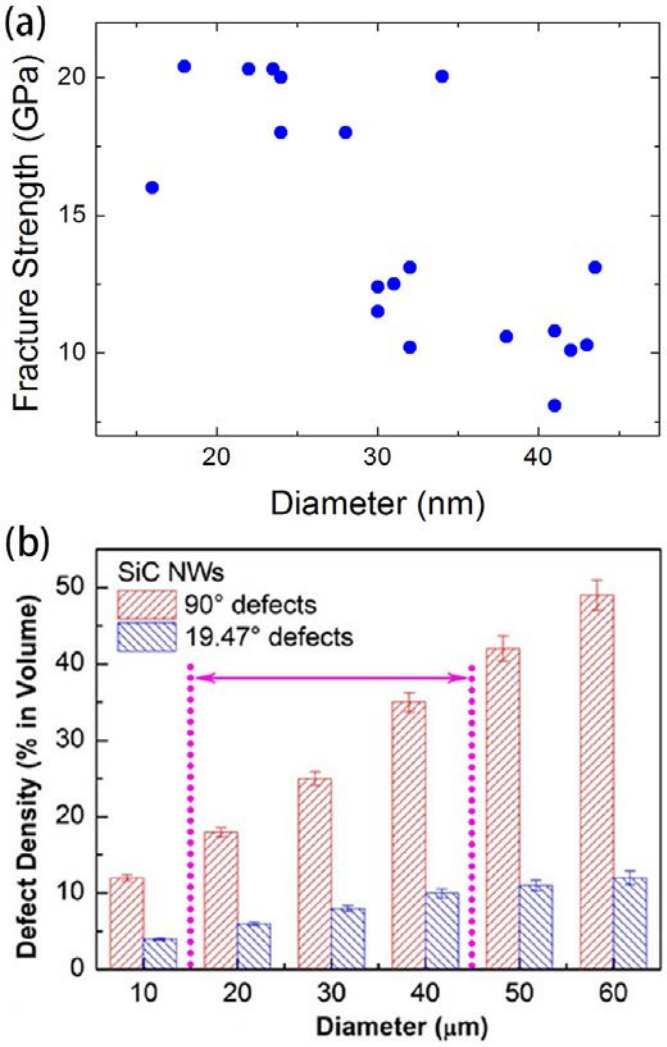

Figure 1-11 The effect of size-dependent defect density on the fracture strength of SiC NWs. (a) Fracture strength of SiC NWs as a function of the diameter. (b) Defect density as a function of NW diameter. The range between the dotted lines corresponds to the diameter range tested (17 nm−45 nm) [181].

In situ TEM fatigue studies have revealed that ZnO NWs are free of fatigue after high-cycle loading up to 10^{10} cycles [182, 183]. However, a NW that was irradiated by an electron beam before resonance testing fractured after resonance for seconds [182]. This is because defects in the NWs act as local stress concentrators,

just like the unavoidable defects (e.g., dislocations and cracks) in materials always serve as sources for crack nucleation and propagation. Therefore, the infinite fatigue life of intact NWs is caused by the defect-free nature of the NWs, which makes crack nucleation extremely difficult. The large surface-to-volume ratio of NWs also contributes to the fatigue-free nature of ZnO NWs, because the surface enhances the atomic mobility that allows the NWs to undergo deformation without fracture.

1.6 Outstanding issues in the field and the aims of this thesis

As seen in the literature review, nanomaterials demonstrate many interesting properties that are not seen in bulk materials and have significant applications in various areas. Before nanomaterials can be successfully incorporated into devices, it is important to gain a better understanding of their mechanical behaviours. However, our understanding of the mechanical behaviours of nanomaterials is still far from complete; there are still some inconsistences and gaps between the existing results on the mechanical behaviours of nanomaterials. As such, to fully utilise the superior properties and advantages offered by the size specificity and selectivity of nanomaterials, further investigation of the mechanical behaviours of nanomaterials, such as NWs and nanofilms, is necessary.

A number of experimental techniques have been developed to measure the mechanical properties of NWs, including resonance, bending, uniaxial tension or compression, and nanoindentation of NWs. Uniaxial *in situ* compression and tension of NWs in an electron microscope are popular nanomechanical testing techniques. However, it is extremely difficult to properly align the NW axial direction with the loading direction because of the nanoscale sample sizes, and most epitaxially grown NWs are tapered. Therefore, loading misalignment and tapering of nanowires are usually unavoidable factors in compression and tensile mechanical property testing of NWs. Unfortunately, these two factors have been largely ignored in previous data analysis of NW mechanical characterisation using uniaxial compression or tension [13, 111, 115, 116, 125]. Neglect of these two factors could lead to inaccurate measured mechanical properties. It is therefore necessary to understand quantitatively how loading misalignment and tapering affect the mechanical behaviour of NWs under

uniaxial compression and tension. The effects of these two factors on the measured compression and tensile mechanical properties of NWs are investigated in this study using quantitative FEA and experimental measurements.

SFs are commonly observed crystalline defects in III-V semiconductor NWs that affect a variety of physical properties. These defects can potentially have a positive impact on some of the physical properties of NWs and therefore benefit certain NW applications [184, 185]. Exploring how crystalline defects affect the mechanical properties of semiconductor NWs is important. However, until now, there have been only a few reports on the effect of planar defects on the Young's modulus of semiconductor NWs, and the available results vary markedly [87, 186]. It is important to explore the mechanical behaviour of semiconductor NWs and to understand how the mechanical behaviour is affected by SFs. The Young's moduli of GaAs NWs with two distinct structures – defect-free single crystalline wurtzite (WZ), and highly-defective wurtzite containing a high density of SFs (WZ-SF) – are investigated here using combined *in situ* compression TEM and FEA.

Due to the small dimensions of nanomaterials, mechanical characterisation of nanomaterials is still a challenge to many existing testing and measurement techniques. Determination of the elastic modulus of nanostructures with sizes at several nm range is even more challenging. Most experimental results on the size dependency of mechanical behaviour have been obtained from nanowires and thin films with dimensions larger than 15 nm [8, 60, 72, 187]. However, due to computational limits, theoretical simulations have normally been used to investigate the size dependency when the dimensions are smaller than 15 nm [129, 130, 138-140], although NWs with a diameter of 20 nm has been simulated [188]. Therefore, there exists presently a gap in the dimensions between experimental measurements and computational predictions. It is necessary to design an experiment to measure the elastic modulus of nanomaterials with dimensions of just several nanometres. In this thesis, a method that combines *in situ* compression TEM and FEA is developed to measure the Young's modulus of nanoscale materials with dimensions as small as 2 nm by using a core–shell NW structure.

2 Methodology

A general understanding of the methods used in this thesis, including TEM, SEM, *in situ* nanomechanical characterisation, and FEA is provided in this chapter, followed by detailed description of the experimental and modelling procedures.

2.1 Electron microscopy

2.1.1 Brief history of electron microscopy

To help exploration of the details of very tiny objects, different tools, for example the magnifying glass and optical microscope, were invented. A good optical microscope can reach a resolution of 260 nm [189]. However, the desire to see further has been driving the exploration of the mechanisms that limit the resolution of optical microscopes and the invention of a microscope with even higher resolution.

In 1873, Ernst Abbe proposed the so-called Abbe diffraction limit for a light microscope: the resolution limit of optical imaging instruments is equal to about half of the wavelength of light used in the microscope [190]. Based on the theory, a light source with a shorter wavelength is necessary to improve the resolution of a microscope. In 1897, J.J. Thomson discovered electrons [191]. In 1924, Louis de Broglie theoretically suggested that electrons had wave-like characteristics, with wavelengths substantially less than those of visible light [192]. Moreover, the wavelength of electrons could be further decreased through accelerating the electrons by applying a high voltage, since [193]:

$$\lambda = \frac{h}{\left[2m_0 eV\left(1+\frac{eV}{2m_0c^2}\right)\right]^{1/2}} \qquad \textbf{2-1}$$

where λ is the wavelength of the radiation, h is Planck's constant, m_0 is the rest mass of an electron, e is the charges carried by an electron, V is the accelerating voltage, and c is the speed of light. For example, with an accelerating voltage of 100 kV and

400 kV, the wavelength of the accelerated electron is ~ 0.00386 nm and 0.00193 nm, respectively. In 1926, Hans Busch found that, in the same way visible light can be focused by lenses, electrons can be focused by magnetic fields [194]. With these findings, the theoretical foundation for building an electron microscope had been established. It was now theoretically possible to build a microscope that could "see" detail well below the atomic level. The first transmission electron microscope TEM was invented by Max Knoll and Ernst Ruska in 1931 in Berlin [195]. Later, in 1936, the Metropolitan-Vicker EM1 was the first commercial TEM successfully built [193]. In 1937, the first high-resolution SEM was developed and built by Von Ardenne [196]. After that, research continued on the electron microscope to improve its resolution limit. Compared to the first commercial TEM, the resolution of today's TEMs has been increased by more than 100 times to sub-angstrom scale [193]. TEM and SEM have become efficient and versatile tools in materials science research.

2.1.2 Interactions of electrons with matter

When fast electrons pass through a thin material, the electrons interact strongly with the material. There are two types of interactions between electrons and a material: elastic interactions and inelastic interactions. There is no measurable energy loss in elastic interactions, while the electrons lose part of their energy to the material in inelastic interactions [193]. The interactions between fast electrons and thin materials lead to many types of products, as illustrated in Figure 2-1. All of these interaction products carry useful information about the materials. By collecting and processing these products, information on the surface morphology, crystal structure, crystal orientation, elemental content etc. can be extracted. Both TEM and SEM use accelerated electrons as the "light source", the major difference between them is they collect and process different types of signals scattered in the interactions between the electrons and the material. Images seen with a TEM are formed by electrons that pass through the specimen, while in SEM, the reflected (or back-scattered) electrons and secondary electrons are collected.

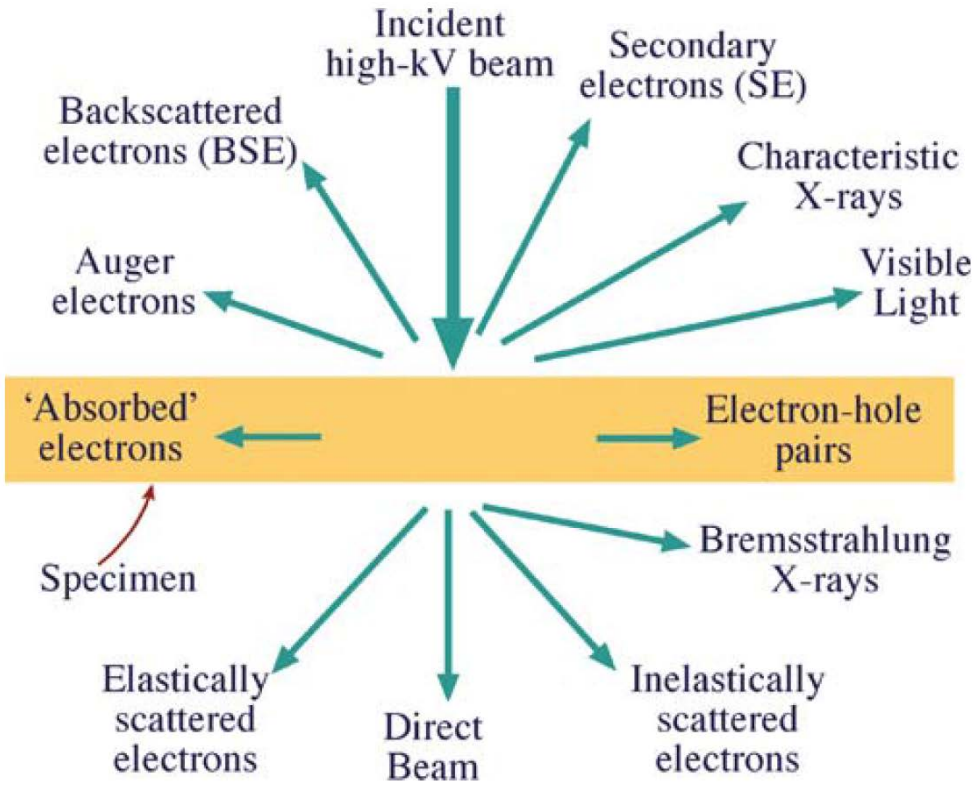

Figure 2-1 The interactions between a high-energy electron beam interacts and a thin material [193].

2.1.3 Transmission electron microscopy

TEM has two operation modes: diffraction mode and imaging mode. The diffraction mode gives electron diffraction patterns, which provide information about the material structure in reciprocal space, while the image mode gives electron scattering contrast images, which provide information in real space. Crystal structural information (for example, unit cell, lattice parameters, space groups, and atomic positions), crystallographic information of the material, and defects in the material can be determined from both diffraction and image modes.

The diffraction mode and image mode can be realised in TEM by controlling the intermediate lenses, as shown in Figure 2-2. A specimen is placed on the front focal plane of the objective lens. In the image mode, an objective aperture is inserted on the back focal-plane of the objective lens to allow selected diffracted beams (one or more), including the transmitted beam, to go through. The image produced by the

objective lens becomes the object for the intermediate lens which produces a second intermediate image. The second intermediate image is further magnified by the projector lens to produce the final image on a fluorescent viewing screen. In diffraction mode, the objective aperture is retracted, while a small selected area diffraction (SAD) aperture is inserted to the first intermediate image plane of the objective lens. Due to the reduction of the strength of the intermediate lens, its focal length is changed from f_I to f_D, and hence an image of the diffraction pattern in the back-focal-plane of the objective lens is focused on the viewing screen. In this mode,

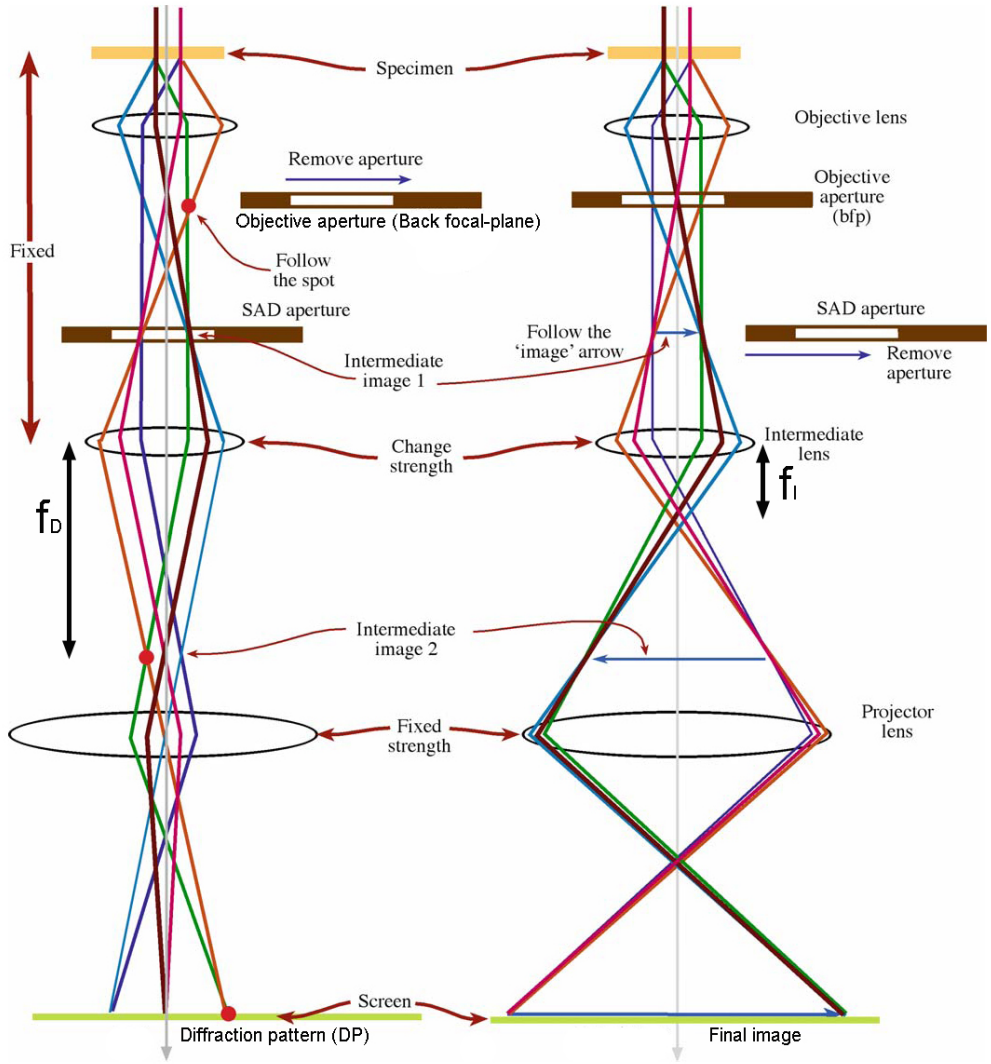

Figure 2-2 Schematic diagrams showing the TEM three-stage magnification imaging system in the diffraction mode (left) and the imaging mode (right) [193].

the back focal plane of the objective lens acts as the object plane for the intermediate lens, so the object for the intermediate lens is the diffraction pattern produced by the objective lens [193].

The incident beam is scattered as it traverses the specimen, and both the amplitude and the phase of the electron wave change at that moment, which give rise to image contrast: so-called amplitude contrast and phase contrast. There are two main types of amplitude contrast, namely, mass-thickness contrast and diffraction contrast.

Diffraction contrast is simply a special form of amplitude contrast where the scattering occurs at special (Bragg) angles [193]. Bragg diffraction is controlled by the crystal structure and orientation of the specimen. In crystalline materials, electrons are strongly scattered by Bragg diffraction, especially in the crystalline area oriented along a zone axis with low indices, so this area appears with dark contrast on a bright field image. To form a diffraction-contrast image in TEM, a small objective aperture is inserted on the back focal plane to select one Bragg scattered beam. The transmitted beam is selected to pass through the aperture to form a bright-field diffraction contrast image. An objective aperture is used to exclude unneeded beams for enhanced contrast. Diffraction contrast is very useful in determining crystalline defects in materials, such as dislocations, twins, and stacking faults.

In addition to amplitude contrast, the difference in the phase of the electron waves scattered through a thin specimen also give rise to contrast in TEM images. A phase contrast image forms by removing the objective aperture or by using a large objective aperture, which allows multiple (> 2) electron beams (not only the transmitted beam, but also diffracted beams) from thin sample areas to contribute to the image. In crystalline materials, the scattering centres (positions of atoms) are periodically spaced, therefore the path difference travelled by all of the waves are integer multiples of the wavelength of the incident wave. The phase contrast image forms as a result of the interference between the transmitted and scattered waves. Phase contrast is mainly used for imaging at the atomic resolution, and employed to image individual atomic columns. Examples of phase contrast include Moiré fringes, Fresnel contrast at defects, and HRTEM images [193].

2.1.4 Scanning electron microscopy

In SEM, the surface of a specimen to be examined is scanned with an electron beam, and the imaging signals generated from secondary electrons or backscattered electrons are collected and then converted to intensity changes in the viewing screen. SE is the most often used signal to produce SEM images because these vary primarily as a result of differences in surface topography. The basic configuration and the working principle of a SEM are illustrated in Figure 2-3. The SEM uses a beam of high energy electrons generated by an electron gun and accelerated through a voltage difference between the cathode and an anode. Then the beam is processed by magnetic lenses, focused at the specimen surface, and systematically scanned (rastered) across the surface of a specimen. The intensity of the signal generated from the interaction between the beam and the specimen is measured from point-to-point across the specimen surface to produce contrast in the image. The intensity of the signal or the contrast in the image generated from each point reflects the topographical and/or compositional difference in the sample. Increased magnification is produced by decreasing the size of the scanned area, which is controlled by the deflection system (two pairs of electromagnetic scan coil). Signals are collected by an electron detector, and then converted to photons by a scintillator, amplified in a photomultiplier. Finally, they are converted to electrical signals to modulate the intensity of the image on the viewing screen [197, 198].

Secondary electrons are formed by inelastic scattering. Normally SE has an energy spectrum in a range of ~ 0 eV–50 eV. Because of their low energy, secondary electrons are easily collected. Generation of the SE signal is mainly affected by the topography of the specimen surface, so the routine SEM image of the specimen surface is formed by SE. Edges and point parts produce more electrons, so they look brighter than the rest of the image. Another important signal used in SEM imagining is BSE, which shows information about the average atomic number of the sample. The angular exit characteristics of BSE are modulated by Kikuchi bands, which can be recorded as an electron backscattered diffraction. Many other signals are also used in SEM imaging, including specimen current, transmitted electrons, electron beam induced current, cathode-luminescence (the emission of ultraviolet, visible, or infrared

light stimulated by electron bombardment), acoustic thermal wave, and x-ray [197, 198].

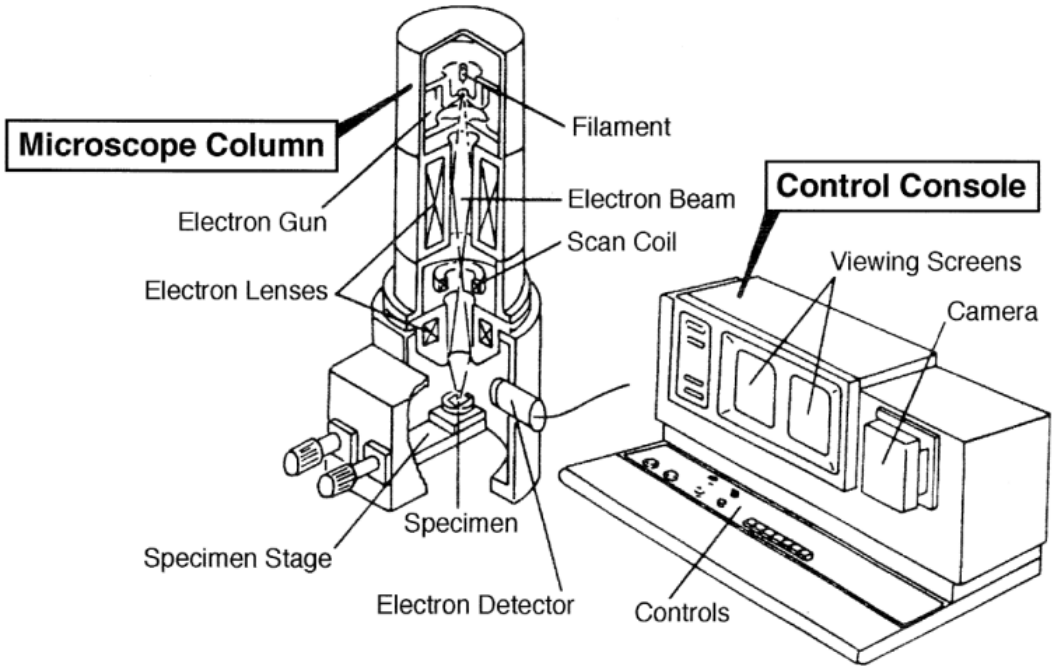

Figure 2-3 A schematic representation of the principle of the SEM [198].

2.2 *In situ* TEM nanomechanical testing

2.2.1 An overview of *in situ* TEM nanomechanical testing

The emergence of nanostructures as fundamental constituents of advanced materials and as key building blocks of next-generation electronic and electromechanical devices has increased the need for the investigation of the mechanical properties and deformation behaviours of materials at the nanoscale. Electron microscopes have been platforms to perform *in situ* nanomechanical testing due to their high-resolution capability. Coupling this capability with *in situ* mechanical deformation enables researchers to have a better understanding of the mechanical behaviours of nanostructures. A number of approaches have been developed to realise *in situ* deformation in electron microscopes.

In 1968, *in situ* indentation experiments were carried out in SEM by using a very fine stylus as an indenter to measure the mechanical properties of metal surfaces, where loads as low as 2 μN could be applied [199]. With some modification of *in situ* indentation techniques in SEM, a series of *in situ* deformation experiments – including indentation, compression, and bending – were conducted in either an SEM or a TEM in 1970 [200]. This was the first use of contact probes inside a TEM. Later, the use of actuated piezo-driven diamond indenters led to the rapid development of *in situ* deformation techniques. Replacing the piezo drive with a depth-sensing transducer and displacement control feedback has increased the sensitivity to load and displacement, while continued device miniaturisation and commercialisation allows experiments to be run almost routinely in the TEM. Recently, several commercial *in situ* TEM straining stages have been developed. The Hysitron PicoIndenter© and NanoFactory holders are the most commonly used commercial products for *in situ* TEM tensile, compression, and bending tests [8, 77-87]. Some stages are able to provide quantitative stress–strain curves during deformation, which is the basic requirement for mechanical property testing.

2.2.2 The PI 95 TEM PicoIndenter

A Hysitron PI-95 Picoindenter holder [201] was used for the *in situ* TEM experiments in this study. The PI-95 Picoindenter is a TEM holder equipped with an indenter. It is the first full-fledged depth-sensing indenter that allows direct observation of nanomechanical testing in a TEM. This holder is specially designed to address various environmental and configurational challenges of a TEM. The most powerful function of this holder is that it provides *in situ* force-time-displacement curves in a precise depth-sensing manner, as well as the corresponding TEM video of *in situ* deformation processes. The coupling of high-resolution techniques offers the potential to reveal the microscopic origin of a transient change in the measured force or the displacement.

The basic hardware components of the PI 95 system include:

- PI 95 PicoIndenter transducer assembly (TEM holder)

- Sample mounting bracket
- PI 95 PicoIndenter control unit, named the *performech*
- Computer and data acquisition system.

Figure 2-4 shows the Hysitron PI 95 PicoIndenter TEM holder, and the enlarged image of the front end of this holder. The core of this holder is the new capacitive force/displacement transducer. The transducer provides electrostatic actuation and capacitive displacement sensing. The traditional three-plate capacitive design provides high sensitivity, a large dynamic range, and a linear force or displacement output signal with displacements up to 5 μm and loads up to 1.5 mN. The transducer consists of the force/displacement sensor, drive circuit board, and hardware used to mount the transducer to the TEM system. The transducer sensor consists of fixed outer electrodes (drive plates), which are driven by AC signals 180 degrees out of phase with adjacent drive plates (Figure 2-5). Since the signals applied to the drive plates are equal in magnitude but opposite in polarity at any instant, the electric field potential is maximised (equal to the applied signal) at the drive plates and minimised (zero, the two opposite polarity signals cancel each other out) at the site cantered directly between the drive plates (Figure 2-5). When a large direct current bias is applied to the bottom plate of the capacitor, an electrostatic attractive force will be created between the bottom plate and the centre plate to pull the centre plate down, then the force is applied to the transducer. The magnitude of the force can be controlled by altering the magnitude of the voltage applied. Since the transducer is electrostatically actuated, substantially larger forces can be realised without compromising force sensitivity [201].

Figure 2-4 PI 95 TEM PicoIndenter holder for usage in JEOL TEMs [201].

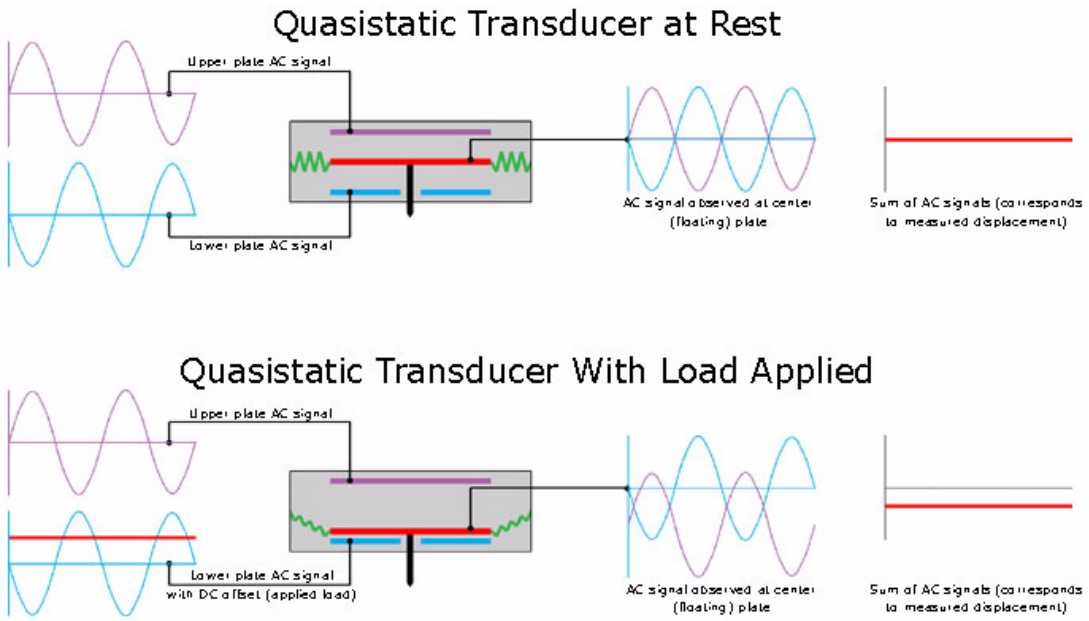

Figure 2-5 The transducer actuation diagram [201].

The axis labelling system of the PicoIndenter differs from that of the existing TEM system. Typically, during an *in situ* TEM deformation experiment, the indentation direction is perpendicular to the direction of the beam, parallel to the direction of the holder. The Hysitron-supplied sample mount consists of a bracket and two screws (Figure 2-4). The sample is adhered to the bracket by using a thin layer of adhesive, such as epoxy. When the sample is adhered to the bracket, efforts should be made to centre the sample, as the movement range of the PicoIndenter is limited. The NW sample should be mounted in a way that the substrate surface is parallel to the surface of the front end of the bracket to ensure that the loading axis is parallel to the NW axis. The sample mounting bracket can be held to the front-end of the holder by tightening the screws. The indentation probe must be fully retracted before loading the bracket to prevent damage to the probe. The PicoIndenter is then ready to be inserted into the TEM.

The PicoIndenter is used with a computer-driven control unit Hysitron call the performech, a state-of-the-art electronic digital signal processor control unit. The control unit provides users with exceptional control and unsurpassed resolution for nanomechanical testing. The PicoIndenter connects to the controller, which connects to the data acquisition computer. All basic instrument operation, data collection, and

analysis are incorporated by the software suite, called TriboScan, in the data acquisition computer supplied by Hysitron. Mechanical testing with difference parameters, such as total displacement and displacement rate, can be realised by editing the loading function using the quasistatic load function editor in the TriboScan software.

2.3 Fundamental concepts of finite element analysis

As we have seen in Chapter 1, significant efforts have been taken to study the deformation mechanisms and mechanical properties of NWs. However, mechanical testing methods at small scales usually have their own limitations and issues. For example, most epitaxially grown NWs are tapered rather than straight-edged [128]. For those tapered NWs, the mechanical properties have to be extracted through FEA, in which the finite element NW models are built based on the experimentally measured real dimensions of the tapered NWs, so the effect of tapering has been considered [8]. In addition to tapering, it is extremely difficult to properly align the NW axial direction with the loading direction because of the nano-scale sample sizes. If these issues are not handled properly, the data extracted from *in situ* compression tests of NWs would be meaningless to the intrinsic mechanical properties of materials at the nanoscale. In many situations, numerical modelling and simulation are conducted to better interpret the experimental data and provide deeper insights into the mechanical behaviour of materials. FEA is an effective approach to simulate the mechanical behaviour of materials at the micron and submicron scales, with controllable loading and modelling parameters [202, 203]. In this section, some basic concepts of FEA are introduced, followed by the introduction of the FEA software package Abaqus used in this thesis.

2.3.1 What is finite element analysis?

FEA is a numerical method for predicting how a structure reacts to forces, vibration, heat, fluid flow, and other physical effects. FEA shows whether a structure

will break, wear out, or work the way it is designed. FEA can be used in a product development process to predict reliability when the product is used in the real-world. FEA was first developed in 1943 by the mathematician Richard L. Courant [204]. In the early 1960s, engineers began to pay attention to this mathematical approach, and this method was used to study the stresses in complex airframe structures in the aircraft industry [205]. Later, the rapid reduction in the cost of computers and significant increases in computing power facilitated the development of FEA to incredible precision.

Because of the diversity and flexibility of the finite element method, it has been extended and applied to structure analysis, solid mechanics, dynamics, thermal analysis, and biomaterials. Recently, the finite element method has also been successfully used in the study of nanostructures, such as nanowires, although this method was originally developed to deal with macroscopic structures. For example, the bending strength of an experimentally bent Si NW that stands perpendicular to the substrate was calculated by FEA [50, 51]. Combined *in situ* compression TEM and FEA was used to evaluate the Young's modulus of GaAs NWs with their diameters ranging from 50 nm to 150 nm [8].

2.3.2 How does finite element analysis work?

FEA consists of a model of a material or design that is stressed and analysed to obtain approximate solutions in engineering. Firstly, a model of the part to be analysed is constructed, and the geometry of the model is broken down into a large number of discrete subregions, or "elements," such as little cubes, connected at discrete points called "nodes." An element is the basic building block of FEA. It is programmed to contain the material and structural properties which define how the structure will react to certain loading conditions. There are several basic types of elements, which can be lines (trusses or beams), areas (2-D plates and membranes), or solids (bricks or tetrahedrals). The selection of the type of elements for FEA that is used depends on the type of the object to be modelled and the type of analysis to be performed. Since these elements can be put together in a variety of ways, they can be used to represent exceedingly complex shapes.

A node is a coordinate location in space where the degree of freedom (DOF) is defined. Some nodes in a model have fixed displacements, while others have prescribed loads. The results of an FEA, including deflections, stresses, and strains, are usually given at the nodes. The density of nodes that are assigned throughout the model depends on the anticipated stress level of a particular area. Areas to be subjected to large stresses, such as a fracture point of a previously tested material, fillets, corners, and complex detail, usually have a higher node density than those areas that experience little or no stress.

A mesh is a list of elements, nodes, and other data that describes the computational domain. The mesh acts like a spider web in that a mesh element extends from each node to each of the adjacent nodes.

Constructing models can be extremely time-consuming, but some commercial FEA software has a user-friendly "pre-processor", which can generate a mesh on a pre-existing computer-aided design (CAD) file.

Once a finite element model has been prepared by the pre-processor, it is used as input to the finite element code itself, which constructs and solves a system of linear or nonlinear algebraic equations. Linear equations use simple parameters and assume that the material is not plastically deformed. Non-linear models consist of stressing the material past its elastic capabilities.

To demonstrate how a complex problem is reduced to a series of simplified interrelated problems by finding solutions for individual elements, an example of a system composed of two springs loaded by external forces is shown in Figure 2-6. The system can be broken down into smaller subregions, i.e., elements connected each other through nodes. Force (F), displacement (d) and spring stiffness (k) are the only parameters in this system. An isolated element is shown in Figure 2-7. For the linear spring, F and d are related through Hooke's law by

$$f_{2x} = k\left(d_{2x} - d_{1x}\right) \qquad \textbf{2-2}$$

The force equilibrium for this single element can be expressed as

$$f_{1x} + f_{2x} = 0 \qquad \textbf{2-3}$$

$$f_{1x} = -f_{2x} = -k\left(d_{2x} - d_{1x}\right) \qquad \textbf{2-4}$$

Collecting the two equations above in matrix form, we have

$$\begin{Bmatrix} f_{1x} \\ f_{2x} \end{Bmatrix} = \begin{bmatrix} k & -k \\ -k & k \end{bmatrix} \begin{Bmatrix} d_{1x} \\ d_{2x} \end{Bmatrix} \qquad \textbf{2-5}$$

or

$$\{f\} = [k]\{d\} \qquad \textbf{2-6}$$

where the square matrix [k] is the element stiffness matrix, the column vector {d} is the element nodal displacement vector, and the column vector {F} is the nodal force vector.

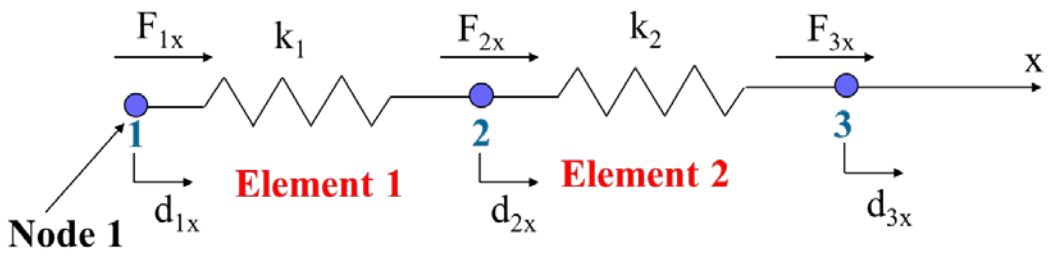

Figure 2-6 Schematic diagram of a system composed of two springs (Element 1 and 2) loaded by external forces.

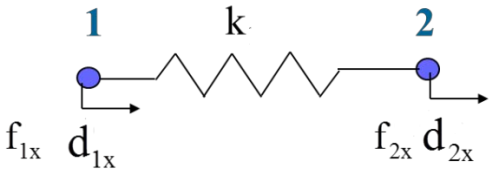

Figure 2-7 Schematic diagram of an isolated element composed of a single spring loaded by external forces.

Although the above matrix expression is derived from a simple example, its form remains unchanged for all of the finite element problems. Having found equations to describe the behaviour of each spring element of the system, we then need to obtain the behaviour of all the elements by assembly. The original structure can be split into component elements (Figure 2-8):

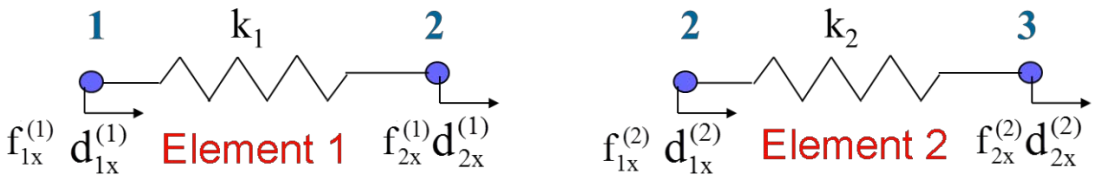

Figure 2-8 Schematic diagram showing the isolated single elements split from an original system composed of two springs.

The equilibrium equations corresponding to the split component elements:

$$\textbf{Element 1:}\quad \begin{Bmatrix} f_{1x}^{(1)} \\ f_{2x}^{(1)} \end{Bmatrix} = \begin{bmatrix} k_1 & -k_1 \\ -k_1 & k_1 \end{bmatrix} \begin{Bmatrix} d_{1x}^{(1)} \\ d_{2x}^{(1)} \end{Bmatrix} \qquad \textbf{2-7}$$

$$\textbf{Element 2:}\quad \begin{Bmatrix} f_{1x}^{(2)} \\ f_{2x}^{(2)} \end{Bmatrix} = \begin{bmatrix} k_2 & -k_2 \\ -k_2 & k_2 \end{bmatrix} \begin{Bmatrix} d_{1x}^{(2)} \\ d_{2x}^{(2)} \end{Bmatrix} \qquad \textbf{2-8}$$

The system assembly procedure is based on the compatibility at the element nodes. At nodes where elements are connected, the value of the unknown nodal variable is the same for all elements connecting at that node. For example, the local displacement of node 2 in element 1($d_{2x}^{(1)}$) and 2 ($d_{1x}^{(2)}$) is the same, and equal to the global displacement of node 2 (d_{2x}), $d_{2x}^{(1)} = d_{1x}^{(2)} = d_{2x}$. To obtain unique values of the displacements of all the nodes, at least one of the nodal displacements must be specified. Thus, boundary conditions have to be considered at this assembling stage.

For the above spring example, the boundary condition is zero displacement of the left end node. After all the above procedures, the finite element problems are now ready for solution.

To summarise, FEA follows three steps:

1. Divide the problem domain into non-overlapping regions (*elements*) connected to each other through special points (*nodes*).
2. Describe the behaviour of each element.
3. Describe the behaviour of the entire body by putting together the behaviour of each of the elements (this is a process known as *assembly*)

For the post-processing of FEA, in earlier days, the values of displacements, stresses, and strains were listed at discrete positions within the model. The user would pore through reams of numbers, so it was easy to miss important trends. Currently, coloured contour plots are displayed in the post-processor to represent stress distribution throughout the model, showing a full-field picture that is easy to read and interpret.

2.4 Experimental and analytical procedures

2.4.1 Specimens

All GaAs NWs samples were grown by Prof. Chennupati Jagadish's group in the Department of Electronic Materials Engineering, Research School of Physics and Engineering at Australian National University. There are three types of samples used in this research, including defect-free zinc-blende (ZB) and wurtzite (WZ) GaAs NWs with a native oxide shell, highly-defective WZ GaAs NWs with a native oxide shell, and ZB GaAs–a-Al_2O_3 core–shell NWs. The GaAs–a-Al_2O_3 core–shell NWs studied in this thesis comprise of two materials, GaAs in the core and a-Al_2O_3 in the shell, which is different from the core–shell NWs mentioned in Section 1.5.1, in which the core is ZnO and the shell is a reconstructed surface layer of ZnO caused by the surface effect.

ZB GaAs NWs with a diameter of 100 nm were coated with amorphous Al_2O_3 (a-Al_2O_3) shells, forming GaAs–a-Al_2O_3 core–shell nanostructures. The ZB GaAs NWs were grown by low-pressure metal-organic chemical vapour deposition using

100 nm Au nanoparticles as the catalyst. Single crystal GaAs NWs were epitaxially grown on a GaAs (111) B substrate using a two-temperature procedure [38]. GaAs NW growth was initiated at the nucleation temperature, T_n, of 450 °C. The temperature was then rapidly ramped down to the subsequent growth temperature, T_g, of 390 °C. Source flows of AsH_3 and trimethylgallium (TMG) are 5.4×10^{-4} and 1.2×10^{-5}, respectively. After NW growth, the a-Al_2O_3 shell was coated via atomic layer deposition with a controlled uniform thickness along the length of the NWs varying from 2 nm to 25 nm.

Wurtzite GaAs NW with a defect-free single crystalline structure and a highly-defective structure containing a high density of SFs were grown by metal-organic chemical vapour deposition using Aixtron 200/4 at a temperature of 575 °C under AsH_3 and trimethylgallium (TMG) molar fractions of 1.43×10^{-5} and 1.04×10^{-5}, respectively, with the Ga and As ratio of 1.4. The semi-insulating GaAs (111) B substrates employed were pre-treated with poly-L-lysine (PLL) and then a 250 nm colloidal Au solution (Ted Pella, Inc.).

2.4.2 Structural characterisation

Structural characterisation was performed using a Zeiss Ultra SEM and a JEM-3000F TEM. For TEM characterisation, NWs are sonicated off the substrate, dispersed in ethanol, and then deposited on a Cu TEM grid with a colloidal/carbon supporting film. The Cu TEM grid is loaded onto a double-tilted holder, which is then inserted into the JEM-3000F TEM for the HRTEM images.

2.4.3 *In situ* compression in TEM

For *in situ* compression in TEM, the NW substrates were cleaved along <110> directions on the (111) surfaces of GaAs substrate into a rhomboid of 2×1 mm^2 using a diamond scribe. As shown in the inset of Figure 2-4, a cleaved substrate sample with vertically aligned NWs was carefully attached onto a mount using epoxy in such a way that a compressive force was applied along its axial direction with a

loading misalignment angle no more than 5°, which was checked in TEM to ensure good alignment (Figure 2-9). A 5° loading misalignment angle in a NW compression test results in less than 10% underestimation of the measured critical buckling load or Young's modulus [206]. A schematic diagram of NW compression tests performed by the PI 95 TEM PicoIndenter holder is shown in Figure 2-9. *In situ* TEM compression tests were conducted in a JEM-2100 TEM using a Hysitron PI 95 TEM PicoIndenter® holder [3] with a diamond flat punch. The compression tests were performed at a constant displacement rate of 10 $nm \cdot s^{-1}$, and the whole process was recorded at a speed of 25 frames per second using a digital video recorder in the microscope. By moving the punch towards a NW, a compressive load is applied to the NW with the loading direction parallel to the NW axis. In response to a gradually increased compressive load, buckling of the NW occurs before fracture. The applied force and displacement of the punch are recorded simultaneously during the deformation process. The fracture strength and critical buckling load of the NW can be easily obtained from the *F–d* curve.

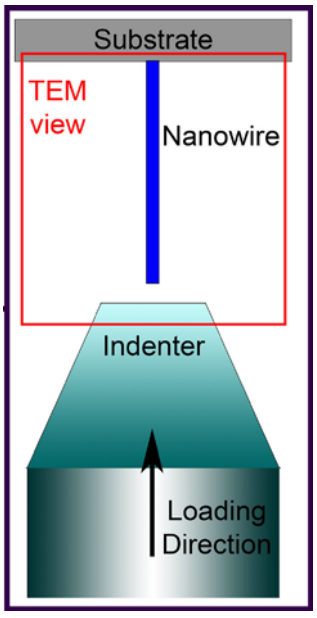

Figure 2-9 Schematic diagram of NW compression tests performed by the PI 95 TEM PicoIndenter.

2.4.4 Finite element analysis

To determine the Young's modulus of a single NW from the experimental measured critical buckling load of the NW, FEA was carried out using Abaqus Version 6.10 software. A NW model was built based on the experimentally-measured dimensions of the NWs. The boundary conditions were set in such a way that the base of the NW was fixed and the tip of the NW was pinned. No rotational and translational motions were allowed at the fixed end, and only rotational motion was permitted at the pinned end. A C3D8R eight-node linear brick reduced integration element with one integration point (Figure 2-10) selected to perform the mesh in all the FEA modelling in this thesis.

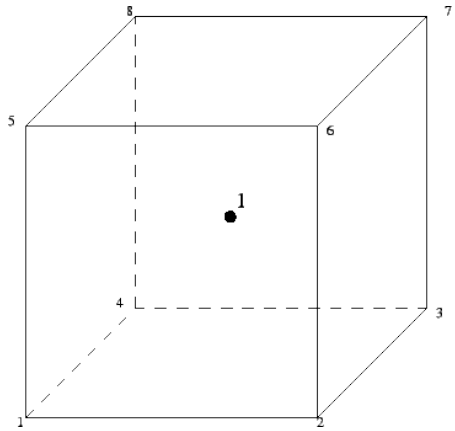

Figure 2-10 A C3D8R eight-node linear brick reduced integration element with one integration point.

The accuracy of the FEA results depends on the mesh size of the model. An example of the basic FEA problem, plate with a hole analysis, is shown in Figure 2-11, where a 2-D solution region is divided into many small subregions using the triangular elements with three nodes. Several models of the plate with different mesh sizes were created to determine the influence of mesh size on results. Figure 2-12 shows the results obtained for different mesh sizes. It is clear that von Mises stress values depend strongly on the mesh size. Reducing the mesh size improves the accuracy of the results. However, finer meshes come with longer calculation time and larger memory requirements. It is necessary to conduct convergence tests to determine

the largest mesh size (i.e. the minimum number of elements) that gives a converged solution. A convergence test begins with a mesh discretisation and then the solution is observed and recorded. The problem is repeated with a finer mesh. A mesh size will be selected when further reducing the mesh size does not lead to much variation in the results.

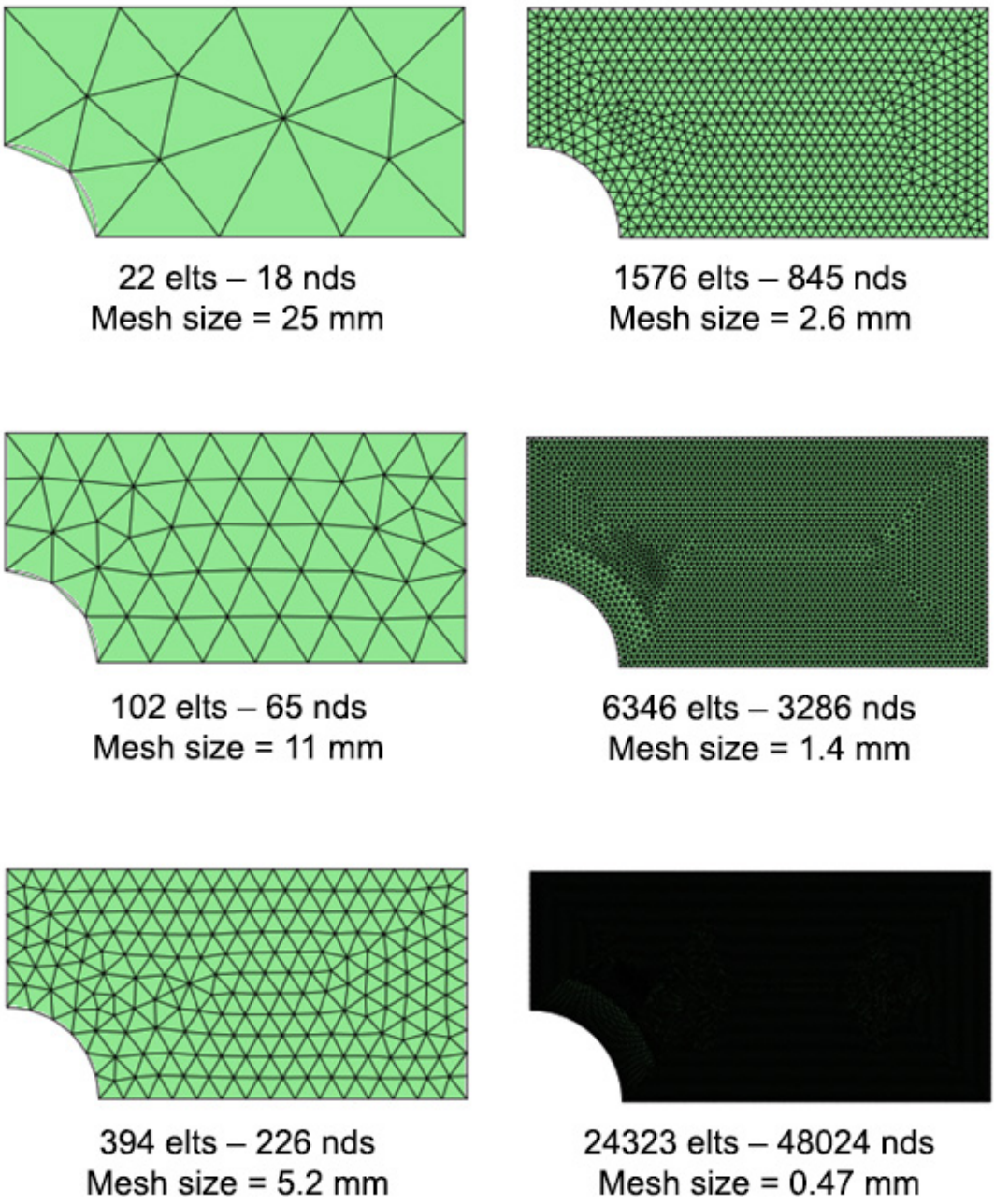

Figure 2-11 A 2-D solution region divided into many small subregions using the triangular elements with different mesh sizes. "elts" = elements, "nds" = "nodes".

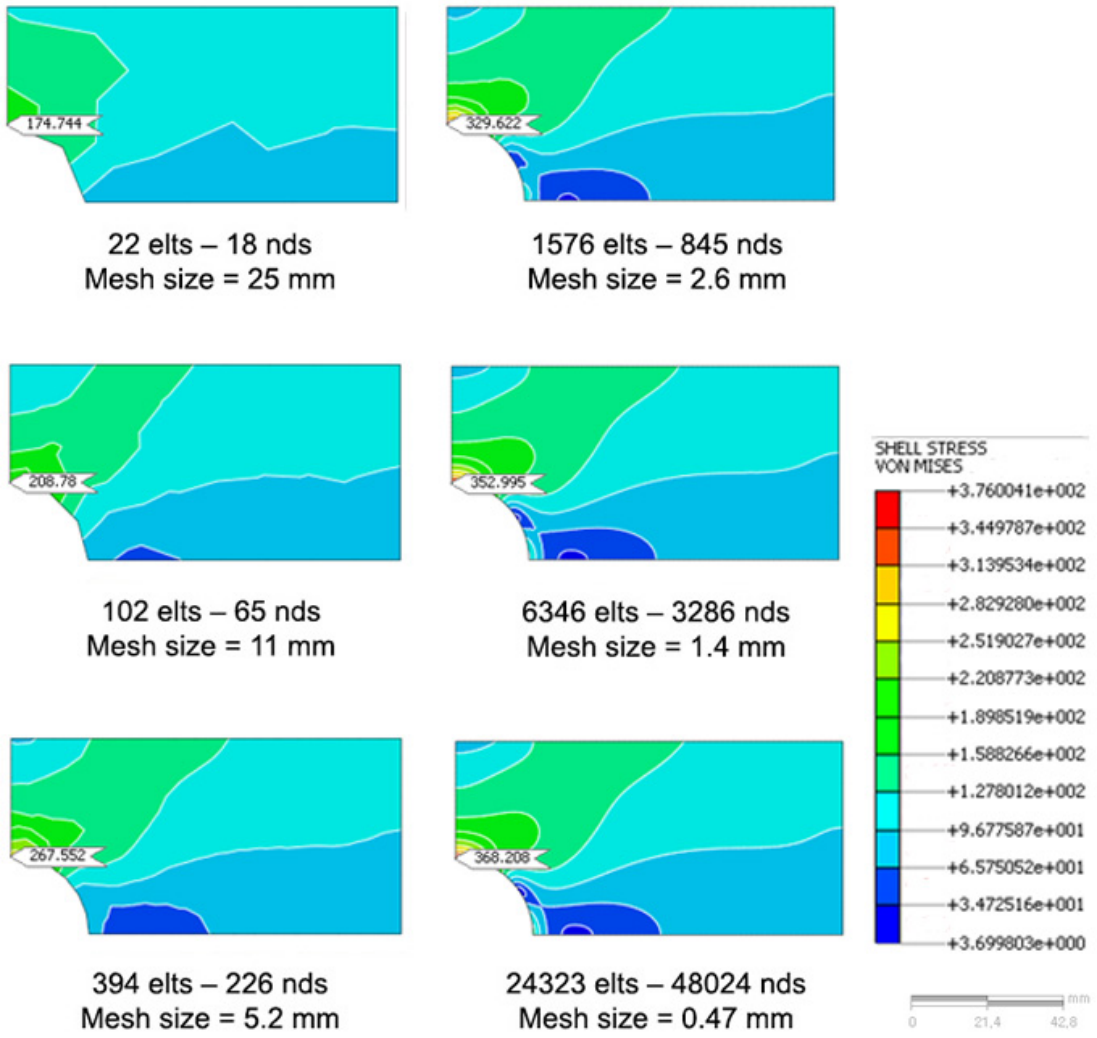

Figure 2-12 Contour plots of the stress distribution for the same plate obtained for different mesh sizes.

In this thesis, the element size was determined from convergence tests for each individual NW. An example of the results from the convergence tests for a NW with a diameter of 100 nm and a length of 1,200 nm are presented in Figure 2-13. The NW model was firstly tested with a mesh size of 20 nm, which generated a total number of 2,160 elements. Then finer meshes, which generated larger numbers of elements, were tested to give converged results. A comparison of the NW models with 2,160 elements and 31,680 elements are shown in Figure 2-14. Young's moduli calculated from the models with different mesh sizes were recorded and normalised with the Young's modulus corresponding to the mesh size of 20 nm. The normalised Young's

moduli were plotted against the total number of elements generated by meshing. The plot shows that the Young's moduli obtained from the models with 31,680 elements (mesh size = 7.2 nm) and 35,738 elements (mesh size = 7 nm) are very close. Therefore, a mesh size of 7.2 nm was selected to generate elements for this model. The optimal mesh size obtained from the convergence tests for NWs with different sizes may be different, so convergence tests were performed for each individual NW to determine the optimal mesh size.

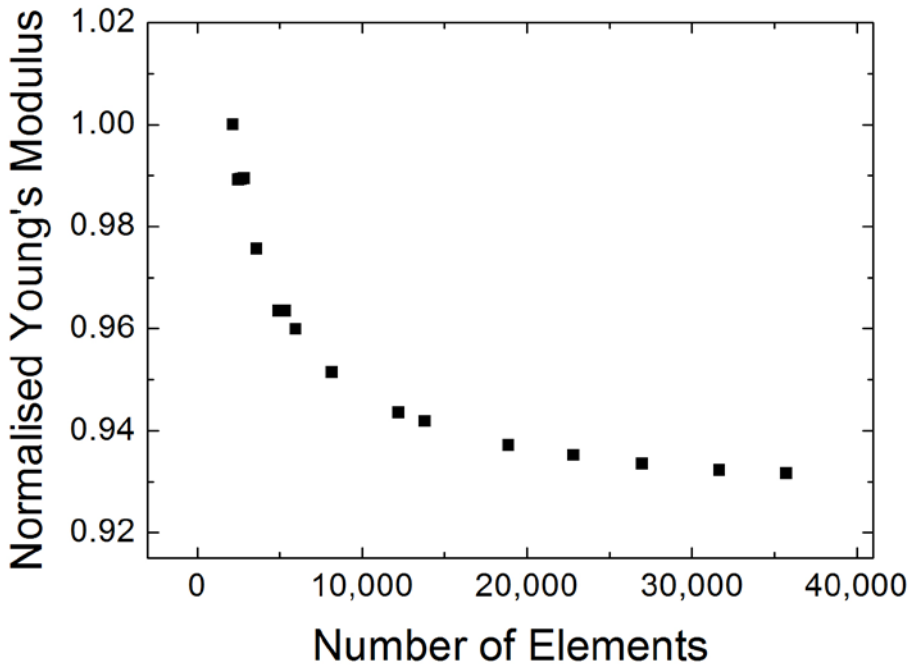

Figure 2-13 The effect of the number of elements (mesh size) on the Young's modulus obtained from FEA.

The Young's modulus of the model (E_{FEA}) was set to an arbitrary value at this step. An arbitrary value of load (P_{FEA}) was applied on the tip of the NW along its axial direction. The linear perturbation method (Buckle) [207] was used to calculate the critical load (P_{crFEA}) corresponding to the given E_{FEA} by giving an Eigenvalue, and the critical load (P_{crFEA}) equals the product of the Eigenvalue and the load applied (P_{FEA}) to the NW in the pre-processing steps, $P_{crFEA} = EigenValue \times P_{FEA}$. According to Euler

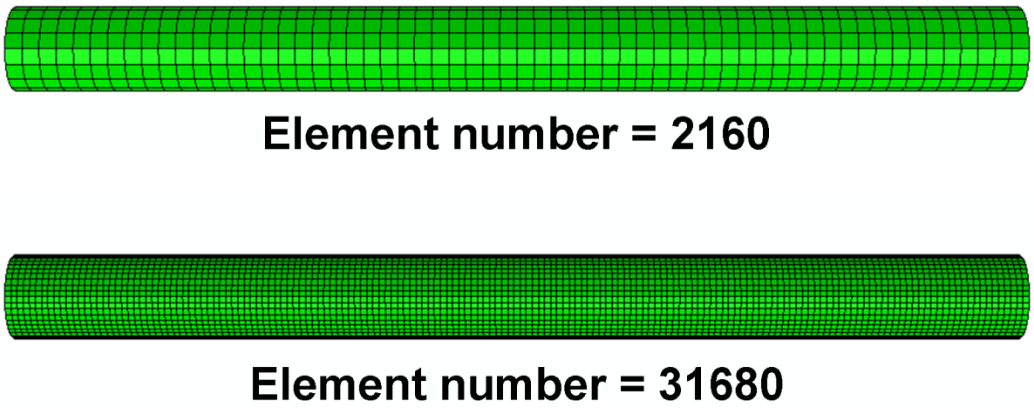

Figure 2-14 NW models with mesh sizes of 20 nm and 7.2 nm, which yield 2,160 and 31,680 elements, respectively.

buckling theory (Equation 1-1), for structures with the same geometry, the buckling load is proportional to the Young's modulus. The effective Young's modulus of the NW was then determined from the expression: $E = E_{FEA} P_{cr} / P_{crFEA}$.

The calculation procedures of how to obtain the Young's modulus for a NW with a diameter of d and a length of l is summarised as following:

1. Obtain the experimentally-determined critical buckling load P_{cr} from the *in situ* compression test.
2. Build the NW model with experimentally-measured dimensions. Set the Young's modulus of the model (E_{FEA}) to an arbitrary value. Apply a load (P_{FEA}) of an arbitrary value on the tip of the NW.
3. Generate meshes for the model with a mesh size determined from convergence tests.
4. Solve the problem with Buckle method, which gives an Eigenvalue. The FEA-calculated critical load (P_{crFEA}) for the NW with a given Young's modulus E_{FEA} is obtained by the following equation: $P_{crFEA} = EigenValue \times P_{FEA}$.
5. Determine the effective Young's modulus of the NW from the expression: $E = \frac{E_{FEA} P_{cr}}{P_{crFEA}}$.

The Riks method (statics, Riks [208]; inclusive of nonlinear geometric effects and fixed step) is used to calculate the elastic strain at fracture. By using this method, a gradually increased load is applied to the tip of a NW. Therefore, in the post-processing step, the results, such as the displacement of the tip and the contour plot of the maximum principal strain distribution, which corresponds to the value of load applied in every step, can be viewed by selecting the step number in the software. The displacement of the NW tip at fracture is experimentally determined from the load-displacement curve obtained from the *in situ* compression test. The fracture strength, at which the NW failed, is determined when the displacement of the tip obtained from FEA reached the experimentally-observed value of the displacement at fracture. The failure strain of the NW is obtained through the contour plot of the maximum strain distribution corresponding to the fracture step.

3 Effects of loading misalignment and tapering angle on the measured mechanical properties of nanowires

3.1 Introduction

Uniaxial *in situ* compression and tension of NWs in an electron microscope are popular nanomechanical testing techniques, since they provide visualisation of the structural evolution processes of nanomaterials under external loading which can directly correlate with the structure, deformation behaviour, and mechanical properties of the nanomaterial [8, 78, 85]. For easy interpretation of experimental results, it is essential to have uniform NW shape and diameter, and perfect loading alignment, i.e., the loading direction is excellently aligned with the NW axial direction during the mechanical testing. However, most epitaxially grown NWs are tapered rather than straight-edged, because NW bases are grown first, and hence are exposed to reactants for a longer time than the later-grown tips [128]. Further, it is extremely difficult to properly align the NW axial direction with the loading direction because of the nano-scale sample sizes. Unfortunately, these two factors have been largely ignored in previous data analysis of NW mechanical characterisation using uniaxial compression or tension [13, 111, 115, 116, 125]. For example, in most NW compression tests, the Young's modulus of a NW was determined based on the conventional Euler buckling theory by measuring its critical axial buckling load [111, 116], which did not take into account of the aforementioned two factors in the data analysis. Neglect of these two factors could lead to inaccurate measured mechanical properties. It has been evidenced that loading misalignment and tapering have significant effects on the test accuracy of micro-compression experiments of posts [209]. The neglect of these two factors in compression and tensile data analysis could be a reason that led to different measured mechanical properties of the same or similar nanomaterials reported by different groups. For example, the Young's moduli of ZnO

NWs with a diameter of 20 nm obtained from uniaxial tensile tests from two groups were 160 GPa and 200 GPa, respectively [115, 118]. Also, the tensile fracture strengths of Si NWs with a diameter of 30 nm measured by two groups were 6.2 GPa and 12.2 GPa, respectively [12, 125].

It is therefore necessary to understand quantitatively how loading misalignment and tapering affect the mechanical behaviour of NWs under uniaxial compression and tension. However, it is difficult to carry out such a study systematically through experiments. FEA is an effective approach to simulate the mechanical behaviour of materials at the micron and submicron scales, with controllable loading and modelling parameters [202, 203]. In this study, we apply FEA to study the effect of tapering of NWs on the critical buckling stress and Young's modulus measured from compression, as well as the effect of loading misalignment and tapering on the fracture strength and Young's modulus obtained from tensile testing. We also conduct *in situ* compression tests in a TEM to explore the effect of loading misalignment on the critical buckling stress.

3.2 Methods

To investigate the effects of loading misalignment and tapering angle on the mechanical behaviour of NWs under uniaxial compression and tension, FEA was performed using the Abaqus software. In this study, ZnO was selected as the model material because the mechanical data of ZnO NWs are readily available in the literature, while no data are available for the Poisson's ratio and tensile fracture strength of GaAs NWs. However, only GaAs NWs are available for *in situ* TEM compression experiments to explore the effect of loading misalignment on the critical buckling load. Therefore, ZnO NWs were used for modelling while GaAs NWs were used for *in situ* TEM compression experiments. The use of different NW materials does not affect the conclusions reached in this study.

Isotropic elasticity is assumed with Young's modulus $E = 150$ GPa and Poisson's ratio $v = 0.3$, which are the average values of ZnO NWs with a diameter larger than 100 nm [61, 115, 118]. For compression testing, the boundary conditions

were set in such a way that the base of the NWs was fixed, and the tip of the NWs was pinned, i.e., the tip end can rotate about any direction and can translate along the axial direction of the NWs. For tensile testing, the base of the NWs was fixed while the tip end can only have translational motion along the loading direction.

To determine the tensile fracture load of a NW, the tensile fracture strength of a ZnO NW with a diameter of ~ 100 nm, which was experimentally determined to be 4.1 GPa [52], was used as the fracture criterion. According to the maximum principal stress criterion, it was assumed that tensile fracture occurred when the maximum principal stress reached 4.1 GPa, so the tensile fracture load of each NW was determined when the load led to the maximum principal stress of 4.1 GPa. Note that the selection of a specific value of the tensile fracture strength does not affect the conclusions reached in this study. To quantify the effect of tapering angle, which is the angle between the tangent of the NW wall and the NW axis, NWs with tapering angle ranging from 0° to 0.8° were modelled, and a uniaxial load P was applied on the tip of each NW. The critical buckling load P_{cr} was obtained using the Buckle method.

Because the Buckle method in Abaqus works only with symmetric loading condition, any analysis with asymmetric loading may lead to incorrect results. As such, *in situ* TEM compression tests, which include asymmetric loading when buckling occurs, were conducted in a JEM-2100 TEM using a Hysitron PI 95 TEM Pico-Indenter holder to study the effect of loading misalignment on the critical buckling load. The NWs have diameters and lengths of 150 nm to 160 nm and 1400 nm to 1500 nm, respectively. The NW sample was attached onto a specimen mount in two ways so that the axial direction of the NWs was (1) parallel to the loading direction and (2) intentionally misaligned from the loading direction with different angles. The angle between the loading direction and the NW axis is defined as the *misalignment angle*. The critical buckling load corresponding to different misalignment angles was determined from the force–time curve obtained during the compression tests. To ensure valid comparison of all the results, the values of the critical buckling load and tensile fracture load were normalised with respect to those of a perfectly-aligned cylindrical NW. This reference NW has the same average diameter as the misaligned or tapered NW.

3.3 Effect of tapering angle

For NWs with the same tapering angle, the reduction of the cross-sectional area of the NW tip is closely related to the slenderness ratio (length/diameter) of the NW. In consideration of the effects of slenderness ratio on the measured properties of NWs, cylindrical and tapered NWs with a length (l) of 1, 1.5 and 2 μm, and a constant average diameter (*d*) of 100 nm were modelled to generate NWs different slenderness ratios. In addition, cylindrical and tapered NWs with diameters of 100, 150 and 200 nm at a constant slenderness ratio of 10 were also modelled. The average diameter of a tapered NW is defined as the average value of the base and tip diameters.

Figure 3-1a shows a schematic diagram of a tapered NW under compression. To explore the effects of NW geometry on the measured mechanical properties in uniaxial compression tests, NWs with a constant average diameter of 100 nm, a constant length of 1.5 μm, and different tapering angles under a constant loading condition were modelled. Figure 3-1b displays the contour plot of maximum principal stress distribution of NWs with 0°, 0.2°, 0.4°, 0.6°, and 0.8° tapering angles, under the same uniaxial compressive load of 6 μN, which is the critical buckling load of the cylindrical NWs calculated from the Euler buckling formula. The buckling point is located near the tip of all NWs and moves closer to the tip with increasing tapering angle. Under the same applied load, increasing the tapering angle increases the maximum principal stress due to the reduced diameter of the buckling site of the NW. This leads to a reduced critical buckling load of the tapered NWs. Figure 3-1c shows the effect of tapering angle of a NW on the critical buckling load of uniaxial compression, suggesting that when the tapering angle increases, the normalised critical load decreases, irrespective of the dimension of NWs. Moreover, the effect of tapering angle on the critical buckling load is more prominent for a slender NW with a larger slenderness ratio, since with the same tapering angle and length, a NW with larger slenderness ratio has more reduction of the cross-sectional area of the NW tip. Since there is a linear relationship between the critical buckling load, critical buckling stress, and Young's modulus [49], for a NW with a slenderness ratio of 15, ignoring the effect of tapering angle of 0.8° will result in 7% underestimation of the critical buckling stress and calculated Young's modulus using Euler's formula.

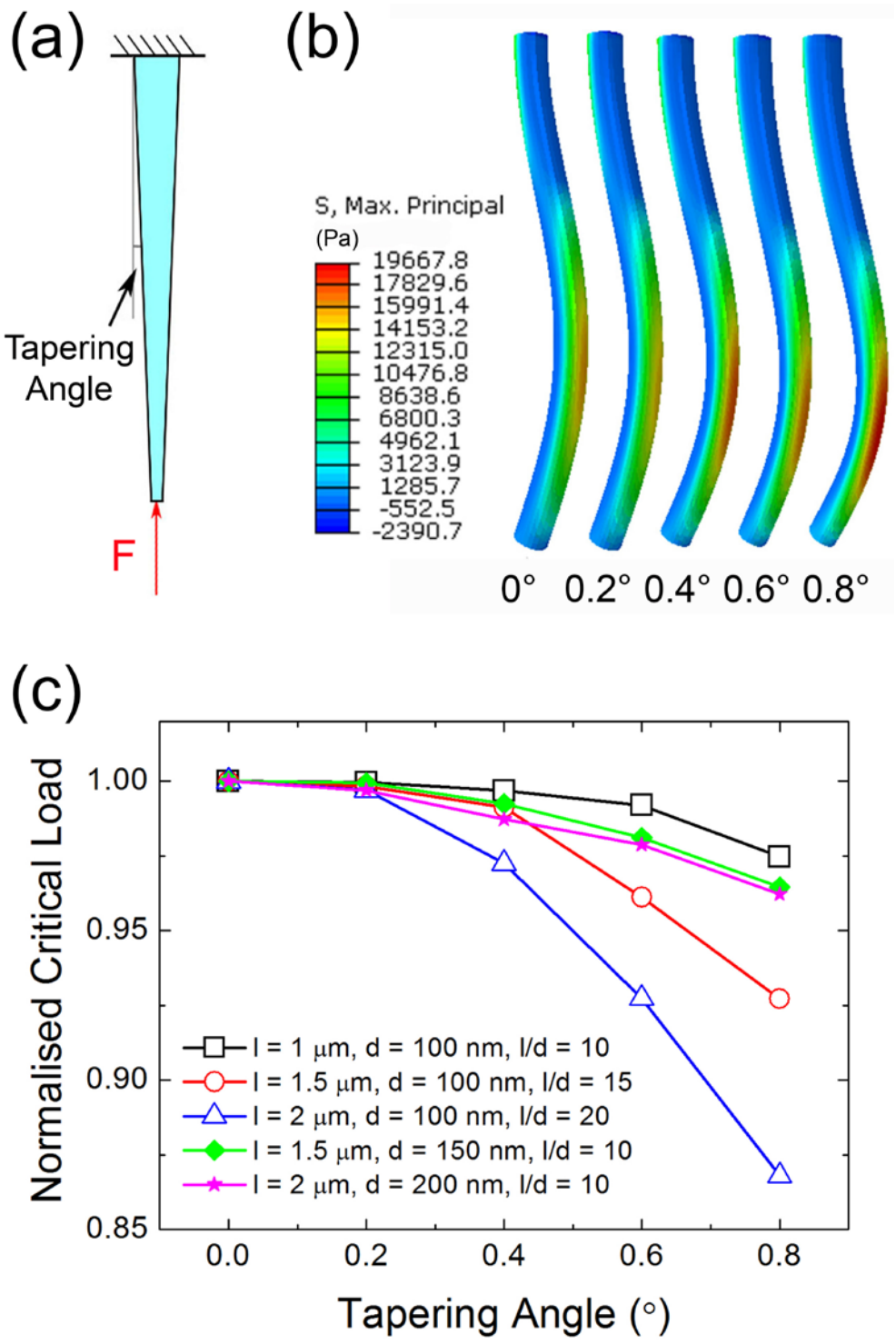

Figure 3-1 (a) Schematic diagram of a tapered NW under compression. (b) Contour plots of maximum principal stress distribution of NWs with a slenderness ratio of 15 and different degrees of tapering angle under the same compressive loading condition. (c) The effect of tapering angle on the normalised critical buckling load of tapered NWs with different slenderness ratios under uniaxial compression.

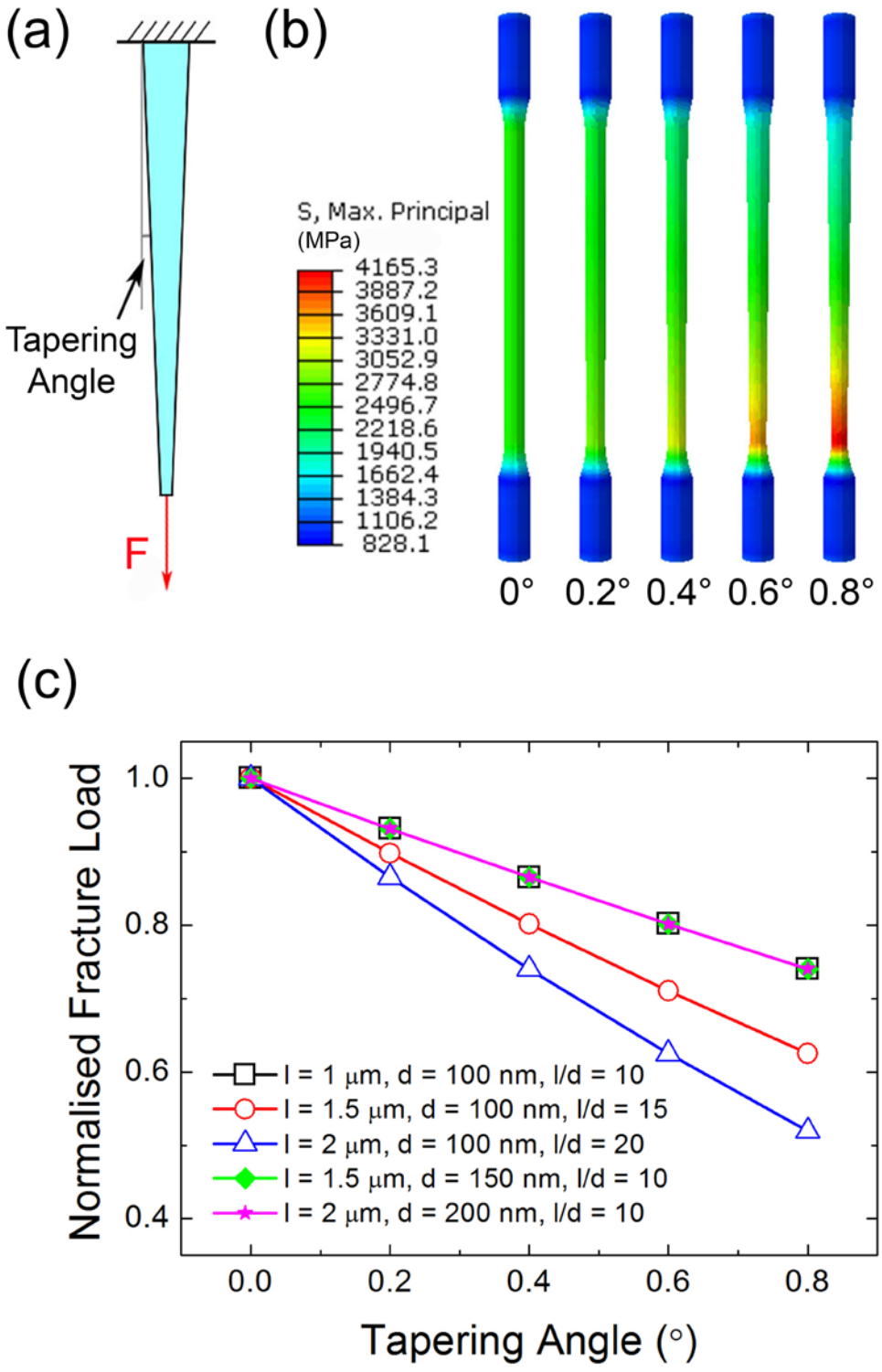

Figure 3-2 (a) Schematic diagram of a tapered NW under tension. (b) Contour plots of maximum principal stress distribution of NWs with a slenderness ratio of 15 and different degrees of tapering angle under the same tensile loading condition. (c) The effect of tapering angle on the normalised tensile fracture load of tapered NWs with different slenderness ratios under uniaxial tension.

Tapering of NWs also has profound effects on their tensile properties. Figure 3-2a shows a schematic diagram of a tapered NW under tension. Figure 3-2b displays the contour plot of maximum principal stress distribution of NWs with a constant average diameter of 100 nm, a constant length of 1.5 μm, and different tapering angles (0°, 0.2°, 0.4°, 0.6°, and 0.8°), under a uniaxial tensile load of 20 μN, at which the maximum principal stress of NW with 0.8° tapering reaches 4.165 GPa. The maximum stress is uniformly distributed along the cylindrical shaped NW. However, with the appearance of tapering, the stress distribution ceases to be uniform, maximum stress is present at the tip of the NW, and the value of maximum stress increases with tapering angle. Figure 3-2c shows the effect of tapering angle of a NW on the tensile fracture load of uniaxial tension. The results reveal that when the tapering angle increases, the tensile fracture load decreases. Moreover, similar to compression testing, the effect of tapering angle on the tensile fracture load is more prominent for a slender NW with a larger slenderness ratio. The results obtained from the three groups of NWs with the same slenderness ratio of 10 overlap, because with the same tapering angle, NWs with the same slenderness ratio have the same reduction of the cross-sectional area of the NW tip. Compared with the effect of tapering on the uniaxial compression testing results of a NW, tapering affects uniaxial tensile testing results more significantly. Therefore, the assumption of a cylindrical shape of a tapered NW during the data analysis of the tensile testing results leads to significant errors in the calculated results. As shown in Figure 3-2c, 37% less load is needed to break a 0.8°-tapered NW than that for a cylindrical NW with the same average diameter of 100 nm and the same length of 1.5 μm, i.e., treating a NW with a tapering angle of 0.8° as a uniform NW in data analysis will result in a 37% underestimation of the tensile fracture strength and Young's modulus calculated from the measured fracture load. This is reasonably expected due to the significant reduction in cross-sectional area near the tip of NW. With the same average diameter, the tip area of a NW with a 0.8° tapering angle is 37% smaller than that of a cylindrical NW, which is exactly the same as the reduction of fracture load. That is, if a tapered NW without any defect fractures near the clamping point, using the tip diameter instead of the average diameter in the calculation of fracture strength will dramatically increase the accuracy of the result. For example, if the fracture load and tip/base area of cylindrical NW are both 1.0, and then the normalised fracture strength is 1.0, which is considered to be the accurate value of normalised strength. Using the

average diameter in the calculation of the fracture load of NW with a 0.8° tapering angle results in a 37% lowered fracture strength than the actual value. However, if the tip area, 0.63, is used, the calculated fracture strength will be 1.0, which is accurate.

3.4 Effect of loading misalignment

Figure 3-3a presents a schematic diagram of a cylindrical NW under tension with misalignment angle. Unlike the effect of tapering angle, the effect of misalignment angle on the tensile fracture load of a NW is independent of the slenderness ratio. Figure 3-3b shows the contour plots of the stress distribution of the NW under tension with 0° and 10° misalignment. Figure 3-3c shows the effect of misalignment angle on the tensile fracture load of a cylindrical NW with a diameter of 100 nm and a length of 1.5 μm. The tensile fracture load decreases with increasing loading misalignment. As shown in Figure 3-3b and the insets in Figure 3-3c, the stress distribution near the tip end of the NW under tension with 10° misalignment is slightly different to that of the NW under uniaxial tension. There is an apparent shear component of maximum principal stress due to loading misalignment, which means a combined tension and shear loading condition. This promotes fracture of the NW and therefore results in a reduction of the tensile fracture load [210]. Ignoring a slight loading misalignment does not have much effect on the calculated results based on the tensile test data, but it is still important to have correct loading alignment in a tensile test of a NW for improved accuracy.

Because the Buckle method in Abaqus works only with symmetric loading condition, any analysis with asymmetric loading may lead to incorrect results. As such, *in situ* TEM compression tests, which include asymmetric loading when buckling occurs, were conducted in a JEM-2100 TEM using a Hysitron PI 95 TEM Pico-Indenter holder to study the effect of loading misalignment on the critical buckling load. GaAs NWs grown epitaxially on a single-crystal GaAs (111) substrate [41] was used for compression testing. The NWs have diameters and lengths of 150 nm to 160 nm and 1400 nm to 1500 nm, respectively. The method used is the same as the one described in the previous paragraph, but, here, the NW sample was

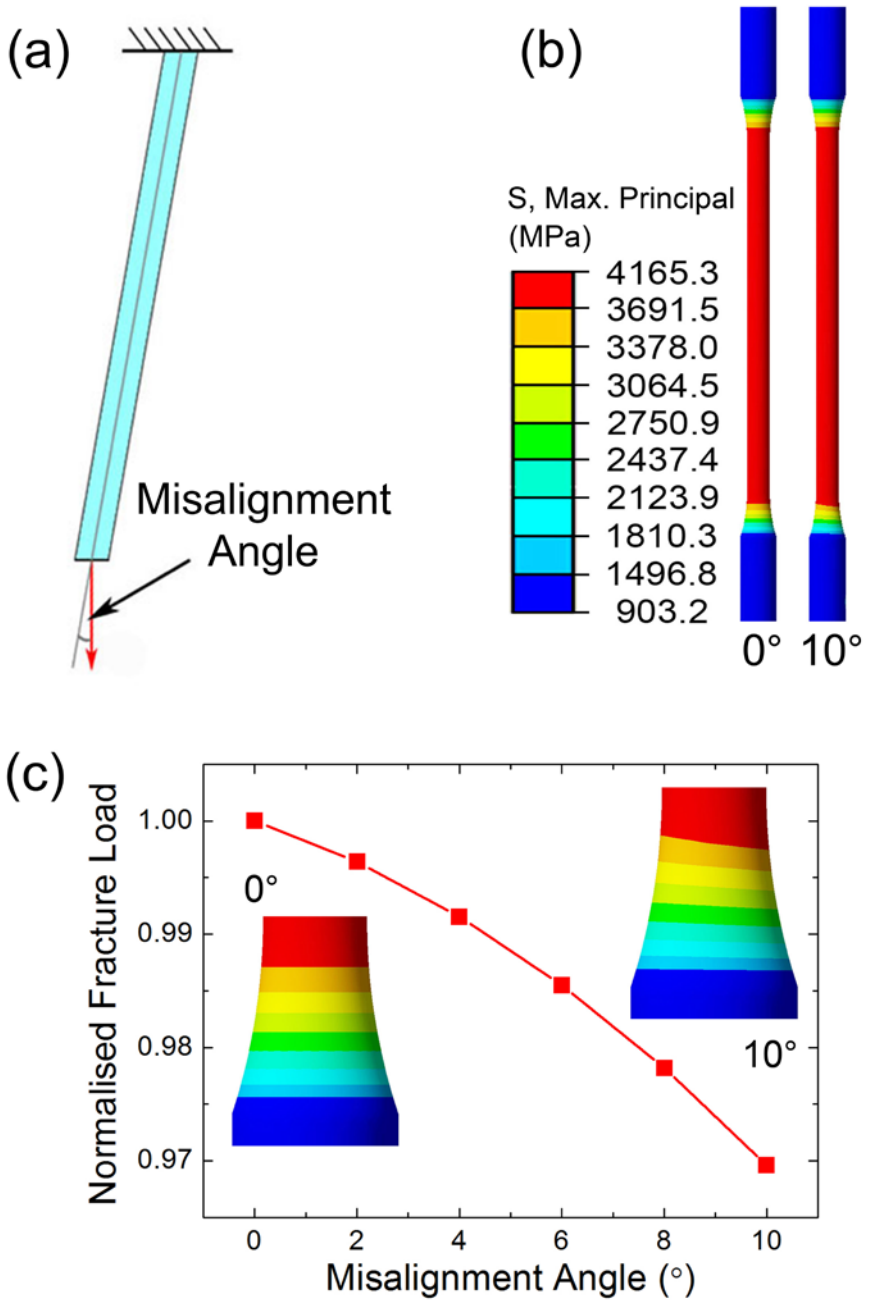

Figure 3-3 (a) Schematic diagram of a cylindrical NW under tension with misalignment angle. (b) Contour plot of maximum principal stress distribution of a cylindrical NW under uniaxial tension and 10°-misaligned tension. (c) The effect of loading misalignment angle on the normalised fracture load of a cylindrical NW with a diameter of 100 nm and a length of 1.5 μm under tension. The insets are the contour plots of maximum principal stress distribution at one end of a cylindrical NW under uniaxial tension (left) and 10°-misaligned tension (right).

attached onto a specimen mount in two ways so that the axial direction of the NWs was (1) parallel to the loading direction and (2) intentionally misaligned from the loading direction with different angles. The angle between the loading direction and the NW axis is defined as the misalignment angle, as shown in Figure 3-3a. The critical buckling load corresponding to different misalignment angle was determined from the force–time curve obtained during the compression tests.

Figures 3-4a–c show typical buckling behaviour of a cylindrical GaAs NW with a diameter of 160 nm and a length of 1500 nm during *in situ* compression testing with 0°, 4°, and 6° loading misalignment angles. TEM images of the same NW in Figures 3-4a–c show 0°, 4°, and 6° loading misalignment angles between the NW axial direction and the compression loading direction. The latter is perpendicular to the surface of the punch. Figure 3-4d shows the force-time curves corresponding to the loading condition in Figures 3-4a–c. Note that plastic deformation of the Au catalytic particle at the tip of the NW occurred during the first compression test, which resulted in the flat portion (indicated by the arrow) of the force curve for 4° misalignment. The flat portion does not affect the measurement of the critical buckling load of the NW. With 0°, 4°, and 6° loading misalignment, the critical buckling load is 35.0, 32.6, and 30.0 μN, respectively, for the same NW.

Figure 3-4e shows the effect of misalignment angle on the critical buckling load of the cylindrical NWs, in which each data point is the average from the results of five individual cylindrical NWs. A misaligned load can be resolved into two components F_x and F_y, which represent the force perpendicular to, and parallel to, the NW axial direction, respectively. For a compression test, the tip is pinned to restrict the translational motion along x and z axes but allow rotation around x, y, and z axes. Therefore, F_x can generate a bending moment M_z to buckle the NW. Compared to uniaxial compression, a smaller force is needed to buckle a NW with loading misalignment due to the bending moment. Therefore, as shown in Figure 3-4e, the critical stress and Young's modulus of the NW estimated without considering the loading misalignment will be lower than the actual values.

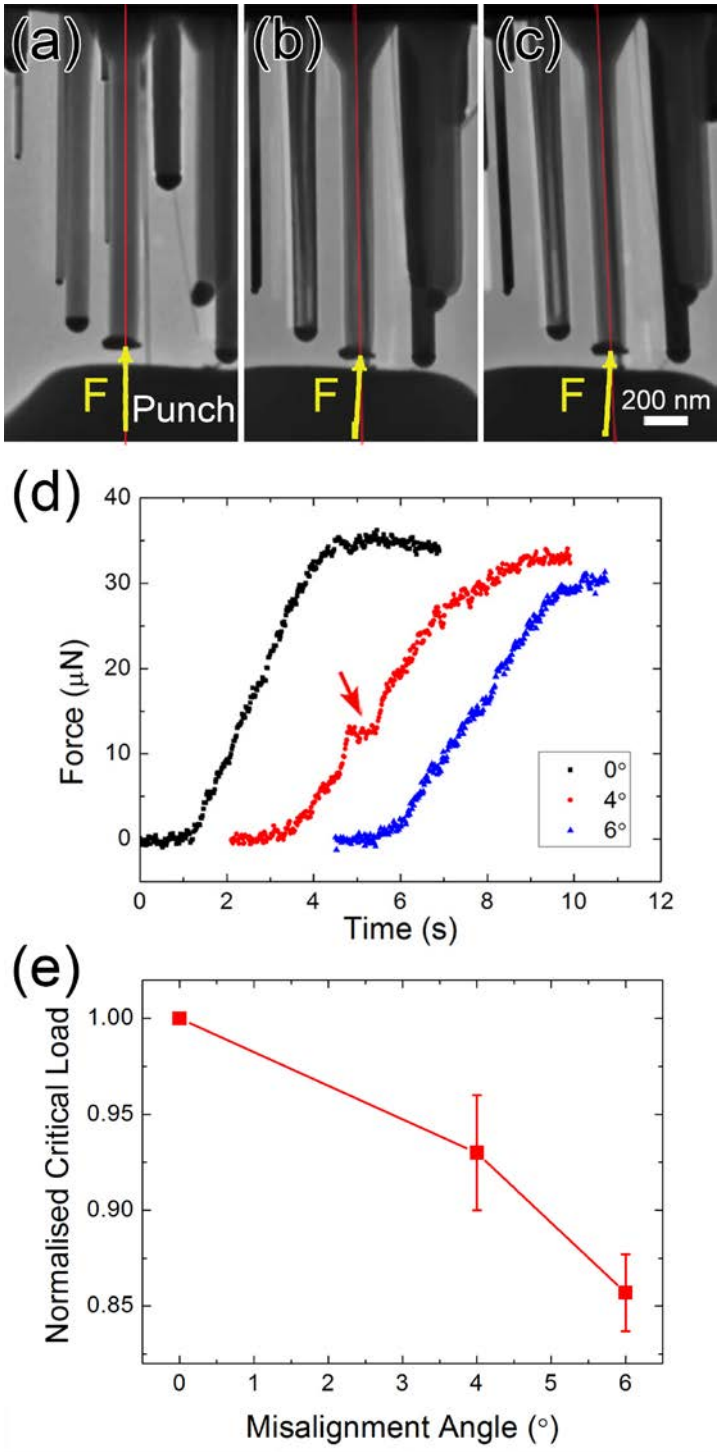

Figure 3-4 (a)–(c) Loading misalignment angle of 0°, 4°, and 6° between the NW axial direction and the loading direction. (d) Force-displacement curves of the same NW with different misalignment angles. The flat portion of the red curve indicated by the arrow is caused by the plastic deformation of the Au particle at the NW tip during the first compression test. (e) The effects of misalignment angle of loading on the normalised critical buckling load of cylindrical NWs under compression.

3.5 Combined effect of misalignment and tapering

Extensive FEA analysis on a tapered NWs under tension shows that the effect of loading misalignment angle on the tensile fracture load of tapered NWs is almost the same as that of cylindrical NWs, as shown in Figure 3-3c. Similarly, the effect of tapering angle on the tensile fracture load of a NW under misaligned loading is also almost the same as that of a NW under uniaxial loading, as shown in Figure 3-2c. The combined effect of misalignment and tapering on the tensile fracture load can be roughly estimated by superimposing the effect of each individual factor, however, the exact values can only be obtained from FEA. As mentioned earlier, the Buckle method in Abaqus works only with symmetric loading condition, so the combined effect of misalignment and tapering on the critical buckling load have not been investigated in this study.

Results obtained from FEA and *in situ* experiments in this study are only related to elastic deformation and therefore are applicable to NWs with different crystal structures. Different from plastic deformation in which crystal structure plays a critical role, the elastic deformation process of NWs should not be affected by their crystal structures, although NWs made from different materials or with different crystal structures have different values of elastic properties.

3.6 Conclusions

The quantitative effects of loading misalignment and tapering angle of NWs on the compression and tensile behaviours of NWs were demonstrated by measuring their critical buckling load and tensile fracture load, respectively. In summary, the following conclusions are drawn:

1. Ignoring the tapering angle and/or loading misalignment leads to different degrees of underestimation of the critical bulking load, Young's modulus, and tensile fracture strength from actual values.

2. Inclusion of these two factors in the compression and tensile data analysis is crucial for accurate determination of the mechanical properties of NWs.

3. Tensile fracture strength can be accurately determined by using the cross-sectional area at the fracture site.

4 Effect of a high density of stacking faults on the Young's modulus of GaAs nanowires

4.1 Introduction

Randomly distributed planar defects, including twins and SFs, commonly lead to the formation of polytypic structures in III-V semiconductor NWs [128, 211-213]. These defects can potentially have a positive impact on some of the physical properties of NWs, and therefore benefit certain NW applications [184, 185]. Just as planar defects are critical in determining the mechanical behaviour of bulk metallic materials [214-217], planar defects also significantly affect the mechanical properties of semiconductor NWs. Previous work has shown that the fracture strength of GaAs NWs greatly increases with the introduction of a high density of SFs [85], while the fracture strength [181] and plastic behaviour [90] of SiC NWs decrease with the presence of a high density of SFs, due to the different effects of SFs on atomic bonds in different materials and the blocking of dislocation slip by SFs. Until now, there have been only a few reports on the effect of planar defects on the Young's modulus of semiconductor NWs, and the available results vary remarkably among different materials [87, 186]. For example, molecular dynamics simulations revealed that increasing the volume fraction of SFs in SiC NWs from 0 to 50% leads to only a 1.0% decrease in Young's modulus [186], while the only available experimental data on this topic showed that introducing 4% volume fraction of SFs into GaN NWs results in a significant reduction of the Young's modulus from 272 GPa to 66 GPa in defect-free GaN NWs [87]. The different SF effects on Young's modulus might come from the intrinsic difference between different materials and/or possible errors introduced in simulations or experiments.

GaAs NWs can have either a cubic ZB or hexagonal WZ structure, although it only exists as a ZB structure in its bulk form. Under certain growth conditions, GaAs

NWs with the WZ structure can have a high density of SFs. SFs, or variations in the stacking sequence in WZ GaAs NWs, result in the formation of defective WZ with short inclusions of other polytypic structures in the NWs. As the properties of these polytypic structures vary, this polytypism may be harnessed to deliver unique structures such as crystal phase quantum dots and superlattices for a variety of novel applications [218-221]. While the physical properties of GaAs NWs are relatively well studied, the mechanical performance of defect-free WZ GaAs NWs and WZ GaAs NWs with high densities of SFs has been less investigated. However, because of the potential functional applications of WZ GaAs NWs, it is important to explore the mechanical behaviour of WZ GaAs NWs and to understand how the mechanical behaviour is affected by SFs.

In this chapter, the Young's moduli of GaAs NWs with two distinct structures – defect-free WZ, and WZ with a high density of SFs (hereafter referred to as WZ-SF) – grown on the same piece of substrate in one growth are evaluated using combined *in situ* compression TEM and FEA. Results obtained show that the presence of a high density of SFs in GaAs NWs significantly increases the Young's modulus of the NWs, and that the Young's modulus of GaAs NWs increases as the NW diameter decreases, regardless of the crystalline structure.

4.2 Results

Figures 4-1a and 4-1b present low magnification TEM images of WZ and WZ-SF NWs, respectively. An Au nanoparticle is seen at the tip of each NW. While no obvious tapering is seen in the WZ NWs (Figure 4-1a), tapering appears in the WZ-SF NWs (Figure 4-1b), i.e., the diameter of the WZ-SF NW at the base is slightly larger than that at the tip. The axial direction of all NWs is [0001]. Typical diffraction contrast and high-resolution TEM (HRTEM) images of WZ NWs are shown in Figures 4-1c and 4-1d, respectively. The HRTEM image of a WZ GaAs NW given in Figure 4-1d, together with a corresponding $\langle 11\bar{2}0 \rangle$ zone axis selected area electron diffraction (SAED) pattern inset in Figure 4-1c, clearly demonstrate that the NWs is of a perfect single crystalline WZ structure. Extensive TEM investigations showed no

planar defect is present in the WZ GaAs NWs. Figures 4-1e and 4-1f present the diffraction contrast image and an HRTEM image, respectively, of a WZ-SF NW. The diffraction spots or the reciprocal space lattice of the structure, as shown in the corresponding $\langle 11\bar{2}0 \rangle$ zone axis SAED pattern inset in Figure 4-1e, are similar to those obtained from the WZ structure. However, long streaks along the $[0001]^*$ direction in the SAED pattern, as well as the stripe contrast in the diffraction contrast image in Figure 4-1e, indicates that the NWs are of a WZ structure with a high density of planar defects parallel to the (0001) plane. The HRTEM image in Figure 4-1f indicates that the planar defects are SFs, leading to polytypic structures including 2H, 4H, 8H, and 3C, with the thickness of each structure ~ 2 nm. It is difficult to quantify

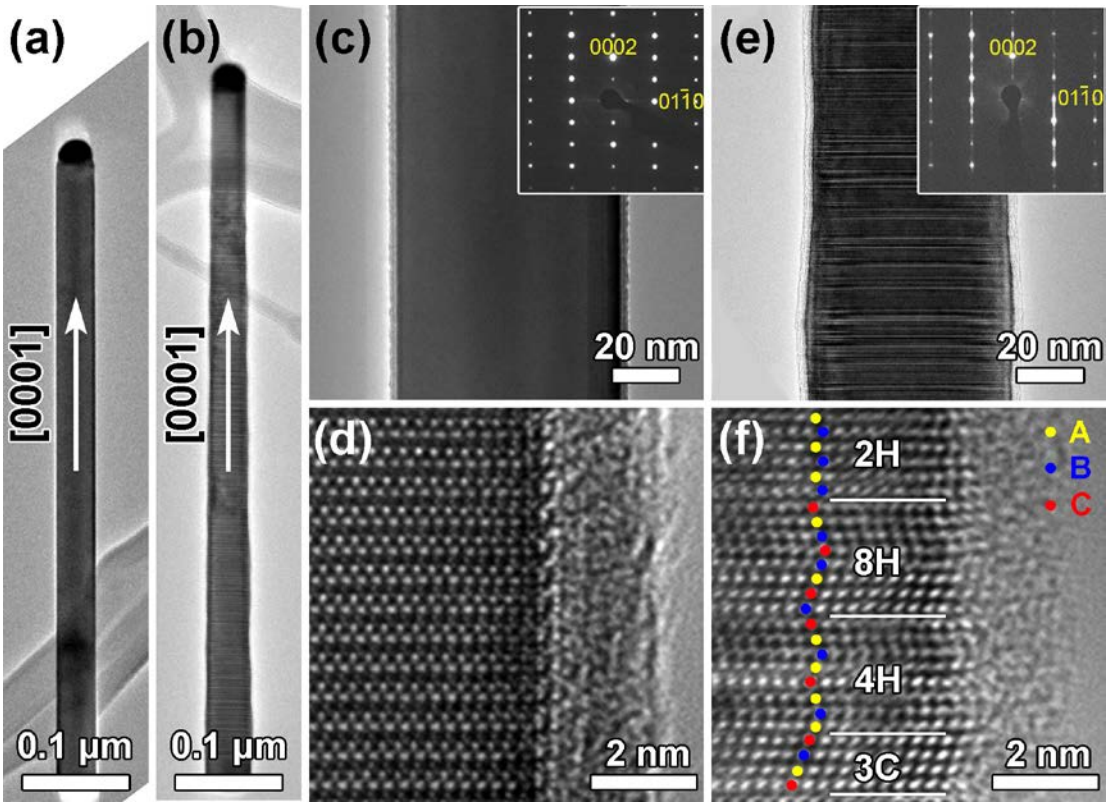

Figure 4-1 Low magnification TEM images of WZ (a) and WZ-SF (b) GaAs NWs. Diffraction contrast (c) and HRTEM (d) images of WZ GaAs NWs. Diffraction contrast (e) and HRTEM (f) images of WZ-SF GaAs NWs. The inset in (c) and (e) are their corresponding SAED patterns.

the volume fractions of these structures as they are randomly distributed along the NW. As shown in Figures 4-1c–f, there is an amorphous layer with a constant thickness of ~ 2 nm on both NWs, forming a core–shell type structure. The amorphous layer is the native oxide formed after the NWs were removed from the growth chamber and exposed to air [84, 222]. Careful examination of the HRTEM images in Figures 4-1d,f shows that the interface between the amorphous layer and the crystalline core is atomically flat for the WZ NWs and wavy for the WZ-SF NWs.

SEM characterisation showed that the GaAs NWs grow perpendicular to the surface of the GaAs substrate, as shown by the SEM image in Figure 4-2a. Since it has been identified in low magnification TEM images that slight tapering appears in WZ-SF NWs and no obvious tapering is present in WZ NWs (Figures 4-1a,b), these two types of NWs can be easily distinguished by their morphologies in the SEM images. As shown in Figure 4-2a, a WZ NW has a large base. The height of the base was not considered when measuring length. SEM images show that the cross sections of both WZ (Figure 4-2b) and WZ-SF (Figure 4-2c) NWs have a hexagonal geometry.

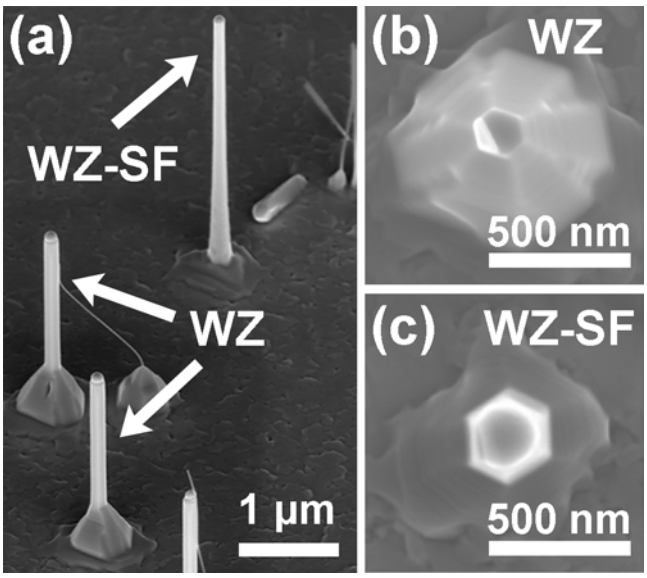

Figure 4-2 (a) An SEM image showing that the WZ and WZ-SF NWs are oriented perpendicularly to the GaAs substrate surface. SEM images show that the cross sections of both WZ (b) and WZ-SF (c) NWs are hexagonal.

In situ TEM compression tests were conducted to investigate the mechanical behaviour of WZ and WZ-SF GaAs NWs. Figure 4-3 shows typical mechanical and structural responses from a WZ-SF GaAs NW under *in situ* compression. The diameter (*d*) and the length (*l*) of the WZ-SF NW, were ~ 97 nm and 1,390 nm, respectively. This diameter was measured at the position where the largest buckling deformation occurred before fracture. The failure of brittle materials caused by compression occurs either by crushing or buckling (lateral deflection), and in the case of a NW depends if its slenderness ratio (*l*/*d*) is smaller or larger than a critical value [49]. The critical value varies and depends on boundary conditions and the type of material. The NW in Figure 4-3 with a slenderness ratio of ~ 14 failed by buckling, while GaAs NWs with a slenderness ratio of ~ 6.5 subjected to uniaxial compression in another study [85] failed by crushing. Figure 4-3a presents the load–time curve (from 3 s to 13 s) with the inset showing the complete load–displacement–time curve of the whole compression test of a NW. Figures 4-3b–e present a series of TEM images corresponding to points 1–4, respectively, in Figure 4-3a. At point 1, the flat punch is in contact with the NW (Figure 4-3b), and the NW is compressed by an axial load, *P*. The load increases with continuous displacement of the punch. The NW then starts to buckle (Figure 4-3c) at point 2, leading to a flat curve after that point. The critical load, $P_{\text{cr-wz}}$ at point 2 is ~ 7.8 μN. Upon removal of the external load, both WZ and WZ-SF NWs, which had buckled but not fractured, are observed to return to their original shape, indicating that the bending deformation is predominately elastic. Figure 4-3f shows the FEA results of the maximum principal strain of the NW at the deformation stage indicated in Figure 4-3d.

The measured Young's moduli of the WZ and WZ-SF GaAs NWs are presented in Figure 4-4. By decreasing the diameter of the WZ NWs from 170 nm to 75 nm, the Young's modulus of the NWs is enhanced from 161 GPa to 189 GPa. Similarly, the measured value of Young's modulus of the WZ-SF NWs increases from 183 GPa to 203 GPa with a reduction of the diameter from 151 nm to 77 nm. Clearly, there is a significant size effect on the Young's modulus. This is caused by the NW core–shell structure, in which the volume ratio of the core and shell varies with NW diameter [8]. Besides the size effect, it is remarkable that the Young's modulus of a WZ-SF NW is ~ 13% higher than that of a WZ NW with a similar diameter.

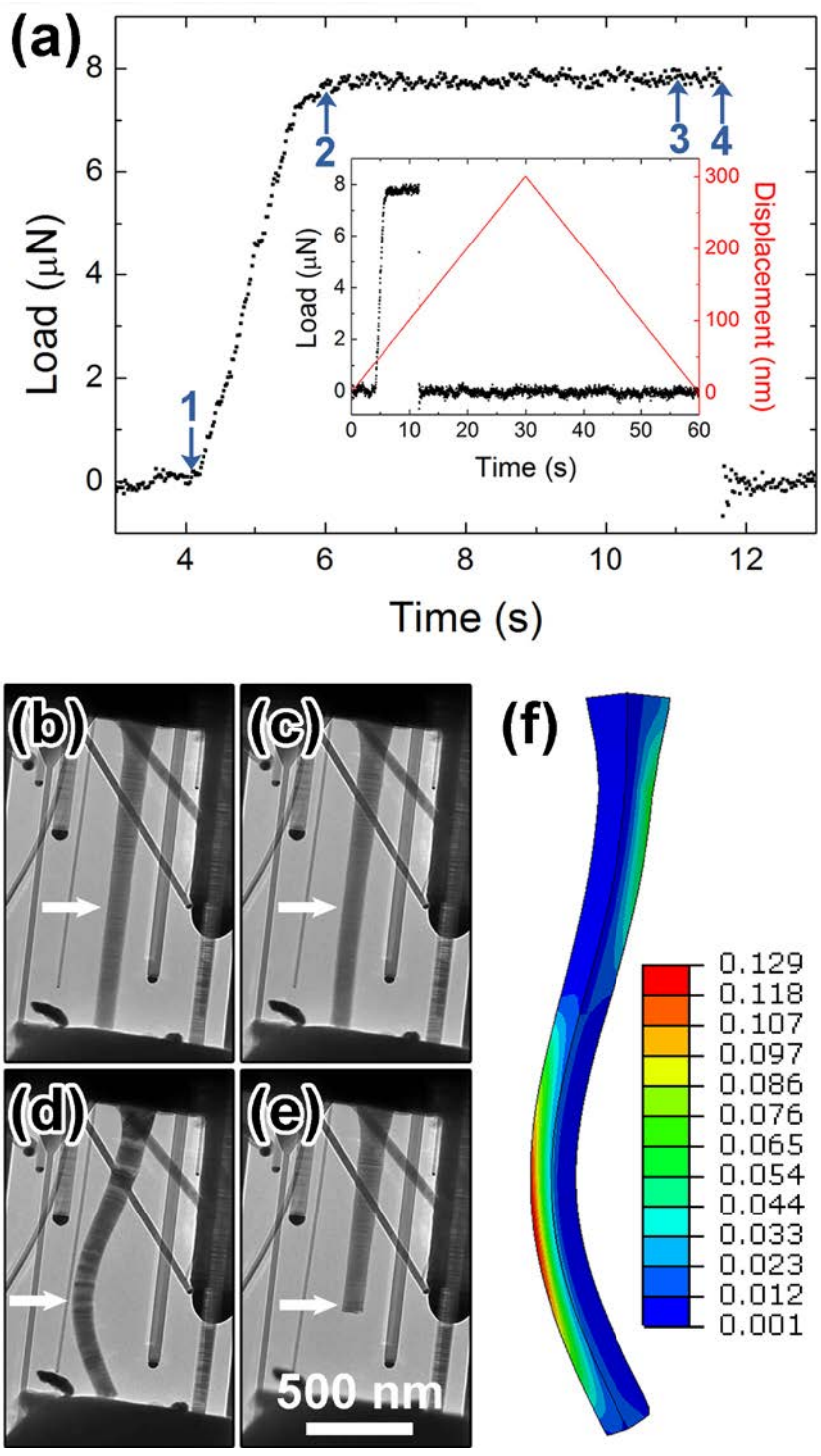

Figure 4-3 (a) A portion of a load-time curve (from 3 s to 13 s) of an *in situ* compression process of a WZ-SF GaAs NW. The inset shows the complete load-displacement-time curve of the whole compression process. (b)–(e) A series of microscopy images corresponding to points 1 (before compression), 2 (the starting point of buckling), 3, and 4 (fracture point), respectively, in (a). (f) FEA simulation of the maximum principal strain corresponding to the deformation state at (d).

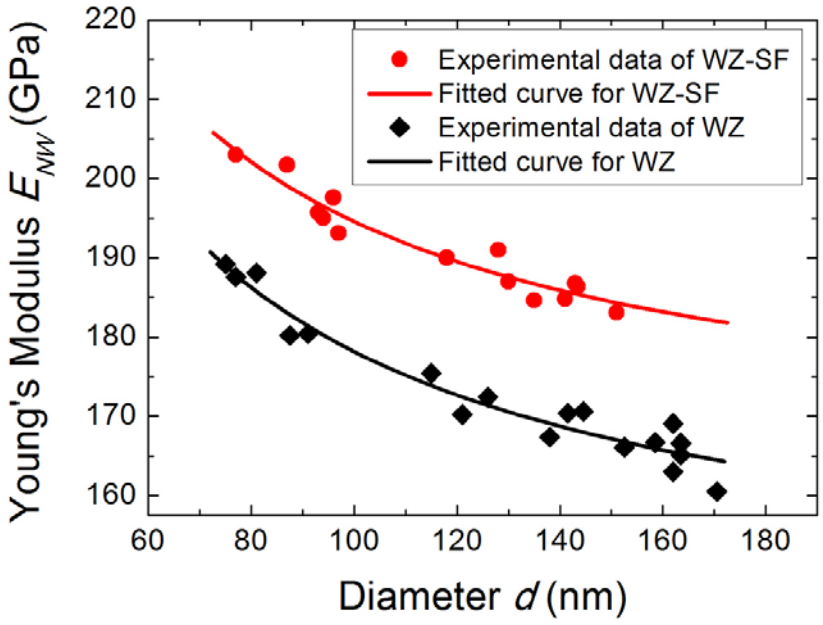

Figure 4-4 Experimental results showing the effective Young's modulus of WZ (black rhombus) and WZ-SF (red dot) GaAs NWs as a function of diameter and best fits to the WZ (black solid line) and WZ-SF (red solid line) data by the core–shell NW model.

As mentioned earlier, the NWs are of a core–shell structure with a GaAs core and an amorphous native oxide shell of ~ 2 nm [8, 11, 84, 144]. For a core–shell structure, the Young's moduli of the core and the shell are inevitably affected by the interface between the core and the shell.[187, 223, 224] To extract the Young's modulus of the GaAs core from the combined modulus of the core, the shell, and the interface, the results shown in Figure 4-4 were fitted to a modified core–shell model [11]:

$$E_{NW} = E_{SI} - \left(E_{SI} - E_C\right)\left[1 - \left(t_{SI}/R\right)^2\right] \qquad \textbf{4-1}$$

where E_{NW} and E_C are the Young's modulus of the core–shell NW and the GaAs core, respectively, E_{SI} is the combined Young's modulus of the shell and the interface, t_{SI} is the combined thickness of the shell and the interface, and R is the overall radius of the

NW including the core and the shell. Equation 4-1 is rearranged in the form of polynomial functions ($p(x) = p_1 x^n + p_2 x^{n-1} + \cdots + p_n x + p_{n+1}$):

$$E_{NW} = \left[t_{SI}^2 \left(E_C - E_{SI} \right) \right] R^{-2} + \left[2 t_{SI} \left(E_{SI} - E_C \right) \right] R^{-1} + E_C \qquad \textbf{4-2}$$

By inputting the values of R and the corresponding E_{NW} of the WZ-SF NWs in Matlab in the form of $y = ax^{-2} + bx^{-1} + c$ gives:

$a = -2206$, $b = 1593$, $c = 164$.

Note that *a*, *b*, and *c* are the coefficients in Equation 4-2, therefore:

$$a = t_S^2 \left(E_C - E_S \right) = -2206 \qquad \textbf{4-3}$$

$$b = 2 t_S \left(E_S - E_C \right) = 1593 \qquad \textbf{4-4}$$

$$c = E_C = 164 \qquad \textbf{4-5}$$

Solving equations 4-3, 4-4, and 4-5, we obtain:

E_C =164 GPa, E_S = 452 GPa, t_S = 2.8 nm.

The mathematical process of curve fitting for WZ GaAs NWs is the same as that for WZ-SF GaAs NWs.

The optimised curve fitting for WZ and WZ-SF NWs yields: E_{C_WZ} = 145 GPa, E_{SI_WZ} = 489 GPa, t_{SI_WZ} = 2.5 nm, $E_{C\_WZ\text{-}SF}$ = 164 GPa, $E_{SI\_WZ\text{-}SF}$ = 451 GPa, and $t_{SI\_WZ\text{-}SF}$ = 2.8 nm. Note that E_{C_WZ} = 145 GPa is very close to the calculated Young's modulus (143 GPa) of WZ GaAs in the bulk form (see below for the detailed calculation), which is similar to the situation of ZB GaAs [11]. It can be seen that the dependence of the Young's modulus on NW diameter described by the equation fits well with the experimental results.

The Young's modulus of WZ GaAs in the bulk form is calculated from stiffness matrix. On account of five independent elastic constants, the corresponding stiffness matrix of wurtzite GaAs is established as

$$C_{ij} = \begin{pmatrix} c_{11} & c_{12} & c_{13} & 0 & 0 & 0 \\ c_{12} & c_{11} & c_{13} & 0 & 0 & 0 \\ c_{13} & c_{13} & c_{33} & 0 & 0 & 0 \\ 0 & 0 & 0 & c_{44} & 0 & 0 \\ 0 & 0 & 0 & 0 & c_{44} & 0 \\ 0 & 0 & 0 & 0 & 0 & \frac{1}{2}(c_{11} - c_{12}) \end{pmatrix} \quad \textbf{4-6}$$

Here, c_{11} = 145 GPa, c_{12} = 51 GPa, c_{13} = 38 GPa, c_{33} = 158 GPa, c_{44} = 38 GPa [225].

According to the generalised Hooke's law, the flexibility matrix of wurtzite GaAs (S_{ij}) is derived from the inverse of the stiffness matrix C_{ij} in Equation 4-6.

$$S_{ij} = C_{ij}^{-1} = \begin{pmatrix} s_{11} & s_{12} & s_{13} & 0 & 0 & 0 \\ s_{12} & s_{11} & s_{13} & 0 & 0 & 0 \\ s_{13} & s_{13} & s_{33} & 0 & 0 & 0 \\ 0 & 0 & 0 & s_{44} & 0 & 0 \\ 0 & 0 & 0 & 0 & s_{44} & 0 \\ 0 & 0 & 0 & 0 & 0 & s_{66} \end{pmatrix} \quad \textbf{4-7}$$

In the flexibility matrix, $s_{11} = 0.0081$, $s_{12} = -0.0025$, $s_{13} = -0.0014$, $s_{33} = 0.0070$, $s_{44} = 0.0263$, and $s_{66} = 0.0213$.

For materials with hexagonal structures, the Young's modulus along a given direction perpendicular to a plane with a plane index (*HKL*) is related to its direction cosine R_3,

$$R_3 = \frac{L}{\sqrt{\frac{4}{3}\left(\frac{c}{a}\right)^2 \left(H^2 + K^2 + HK\right) + L^2}} \quad \textbf{4-8}$$

where *c* and *a* are the lattice constants of the hexagonal structure.

Then, the Young's modulus (*E*) perpendicular to the (*HKL*) plane can be obtained from the following equation:

$$E_{(HKL)}^{-1} = s_{11}\left(1-R_3^2\right)^2 + s_{33}R_3^4 + \left(2s_{13}+s_{44}\right)R_3^2\left(1-R_3^2\right) \quad \textbf{4-9}$$

In this study, WZ GaAs NWs was grown along the [001] direction (or [0001] in the four-digit Miller-Bravais indexing system). Therefore, taking the parameters (*HKL*) = (001) into Equation 4-8, the direction cosine of [001] is

$$R_3 = \frac{1}{\sqrt{\frac{4}{3}\left(\frac{c}{a}\right)^2\left(0^2+0^2+0\right)+1^2}} = 1 \quad \textbf{4-10}$$

Taking the values in the stiffness matrix of GaAs (S_{ij}) and the direction cosine of [001] into Equation 4-9,

$$E_{(001)}^{-1} = s_{11}\times\left(1-1\right)^2 + s_{33}\times 1 + \left(2s_{13}+s_{44}\right)\times 1\times\left(1-1\right) = s_{33} = 0.0070 \quad \textbf{4-11}$$

Therefore, the modulus is $E_{(001)} = \left(0.0070\right)^{-1}$ = 143 GPa, i.e., the Young's modulus of bulk WZ GaAs along the [001] (or [0001]) direction is 143 GPa.

4.3 Discussion

In this study, the Young's moduli of the shell in the WZ and WZ-SF NWs are 489 GPa and 451 GPa, respectively. As the amorphous native oxide surface is the same for all NWs, the ~ 8% difference in the Young's moduli of the shell must come from the slightly different interfacial thicknesses and the difference of the interfacial bonding. The latter should stem from the different crystalline structures of the core which has either a WZ or a WZ-SF structure (HRTEM images in Figure 4-1). The shell thicknesses obtained from the curve fitting for WZ and WZ-SF NWs are 2.5 nm and 2.8 nm, respectively. The wavy interfacial structure of WZ-SF NWs is responsible for its slightly thicker average interfacial thickness.

The Young's modulus of the core of GaAs NWs with a high density of SFs is ~ 13% higher than that of defect-free GaAs NWs, contradicting the suggestion that crystalline defects would decrease the Young's modulus of a material [186, 226]. A recent experimental study suggested that the Young's modulus of the SF regions in

GaN NWs is only 4.5 GPa, which is ~ 98% lower than that of defect-free bulk GaN (272 GPa). As such, the introduction of SFs significantly reduced the Young's modulus of GaN NWs [87]. It is worth noting that the volume fraction of the SFs in the GaN NWs in that study was only 4%, resulting in the presence of a very small amount of 3C structure in a 2H structure matrix, while the angle between the SFs and the NW axis was 54.6°. By contrast, the SF density in our NWs is high, generating a range of complex polytypes such as 2H, 4H, 8H, and 3C, which vary in thickness from 1 nm to 3 nm. These SFs are further oriented in a perpendicular direction to the growth direction [0001] (NW axis), which is also different from those reported in GaN NWs [87]. This difference in orientation and type of SFs might contribute to the difference in the Young's modulus measured for both of GaN [87] and GaAs NWs.

The Young's modulus of WZ-SF GaAs NW core (164 GPa) is higher than that of pure WZ GaAs (143 GPa) and pure ZB GaAs (86 GPa) [227]. The WZ-SF NWs exhibit a random mixture of many different structures, including 2H, 4H, 8H, and 3C, along the NW axial direction. The mechanism of the SF-induced stiffening effect in WZ GaAs NWs is thus likely complex. At the atomic scale, the magnitude of the Young's modulus can be regarded as the embodiment of the interatomic-bonding force, which decreases with increasing interatomic spacing [47]. Thus, Young's modulus is very sensitive to the configuration of interatomic bonding. Crystalline defects alter the interatomic bonding at the defect areas [226, 228]. The variation of bond arrangement at the SF sites is considered an important factor for the high Young's modulus of WZ-SF NWs. First principles calculations of the bonding in AlN, InN, GaN, and BeO with WZ structures suggested that the bond strength for a ZB-like region – a region introduced by a SF in the perfect WZ structure – is higher than that of the un-faulted WZ structure [229]. It has also been shown from *ab initio* simulations that the bond strength varies at different bonding locations [230], e.g., the A, B, or C stacking sites as shown in the HRTEM images of WZ-SF NWs (Figure 4-1f). The various arrangements of atom stacking in different structures presented in WZ-SF NWs may change the local interatomic interaction and thus change (increase) the Young's modulus. Molecular dynamics simulations might be an effective way to explore the effect of SFs on Young's modulus in WZ-SF GaAs NWs if appropriate potentials for the SF areas are available for the simulations. Further investigations are

needed to better understand the mechanism behind the stiffening effect of SFs on GaAs NWs.

4.4 Conclusions

The Young's moduli of WZ and WZ-SF GaAs NWs were investigated through combined *in situ* compression TEM and FEA. In summary, the following conclusions are drawn:

1. The presence of a high-density of SFs that leads to the formation of short polytypic segments results in an increase of the Young's modulus of GaAs NWs. The stiffening effect of SFs is attributed to the change of the interatomic bonding at the SFs.

2. The Young's moduli of both WZ and WZ-SF GaAs NWs increase with decreasing NW diameter, which is caused by the increase of the volume ratio of the amorphous shell of the NWs with decreasing NW diameter. The Young's modulus of the interfacial area between the amorphous shell and the crystalline core varies with the crystalline structure of the core.

3. The findings in this work provide a better understanding of the effect of high-density SFs on Young's modulus and offers potential guidance in using defect engineering to tailor mechanical properties of nanostructures.

5 Young's modulus of ultrathin nanomaterials

5.1 Introduction

As mentioned in Section 1.4.5, due to the computational limits, only theoretical simulations have been used to investigate the size dependency of elastic properties for nanomaterials with dimensions of smaller than 15 nm [129, 130, 138-140]. Moreover, opposite size-dependencies of Young's modulus were predicted for different materials [139, 140].

Experimental measurements are essential to confirm computational results. However, due to the difficulty of sample handling, the sensitivity limits of testing facilities, and the inability to decouple the mechanical properties of thin films from those of their underlying bulk substrates, most experimental results on the size dependency of mechanical behaviour have been obtained from nanowires and thin films with dimensions larger than 15 nm [8, 60, 72, 187]. Therefore, a gap in the dimensions between experimental measurements and computational predictions. Moreover, experimental results [8, 60, 72] have demonstrated that there are size effects in nanoscale materials with dimensions in the range from ~ 15 nm to 150 nm, which contradict certain computational predictions that proposed size effects only exist in nanomaterials when their dimensions are less than ~ 15 nm [129, 130, 138]. The gap between the experimentally-measurable dimensions and the computationally-predictable dimensions makes it difficult to explain the discrepancy between experimental and computational results, as well discrepancies between different computational results. In the latter case, for example, the modulus of a SiC NW with a diameter of 0.864 nm was predicted to be 768.8 GPa [141], whereas subsequent work predicted the modulus of a SiC NW with a similar diameter as 504.8 GPa [231].

In this chapter, we designed a method to measure experimentally the Young's modulus of nanoscale materials with one dimension as small as 2 nm by using a core–

shell NW structure. *In situ* nano-compression in a TEM and FEA were used to determine the Young's modulus of the core–shell NWs. As mentioned in Section 2.4.1, the core–shell NW in this study is a heterostructure that comprises two materials, which is different from the case discussed in Section 1.5.1, in which a ZnO NW with a modified surface layer is treated as a core–shell structure. The Young's moduli of shells with different thicknesses were then extracted using a core–shell model. This method uses a core–shell NW structure with a relatively large core diameter (100 nm), which overcomes the sensitivity limits of testing facilities. Moreover, using a core–shell model makes it possible to decouple the Young's modulus of shells from their underlying cores.

5.2 Results

The orientation of the GaAs–a-Al_2O_3 core–shell NWs is perpendicular to the GaAs substrate surface, (i.e., along a <111> direction), as shown in a typical SEM image provided in Figure 5-1a. A low magnification TEM image and a corresponding SAED pattern of a NW presented in Figure 5-1b clearly demonstrate that the NW is of a perfect single crystalline ZB (FCC) structure and the NW growth direction is [111]. The Au nanoparticle can be seen at the tip of the NW. The NW diameter at the base is slightly larger than that at the tip, resulting in a tapering angle of ~ 0.7°. A shell covering the surface of the NW is clearly seen in Figure 5-1b. Figure 5-1c provides a typical HRTEM image of a NW with a 10 nm thick a-Al_2O_3 shell, confirming that the NW core is a single crystal with the ZB structure. Extensive TEM investigations indicated that there were no planar defects present in the GaAs core. A typical HRTEM image of a NW without a-Al_2O_3 coating is shown in Figure 5-2. Instead of an a-Al_2O_3 shell, the GaAs NW in Figure 5-2 is coated with a native oxide shell with a thickness of ~ 2 nm that formed in the oxidation of the NW surface when the NW was removed from the growth chamber and exposed to the air. The NW core is still single crystalline ZB GaAs. The only difference between the two groups of samples is that the GaAs–a-Al_2O_3 core–shell NWs are coated with a layer of a-Al_2O_3 of varying thicknesses and the GaAs NWs without a-Al_2O_3 shell are coated with a layer of a native oxide with a fixed thickness.

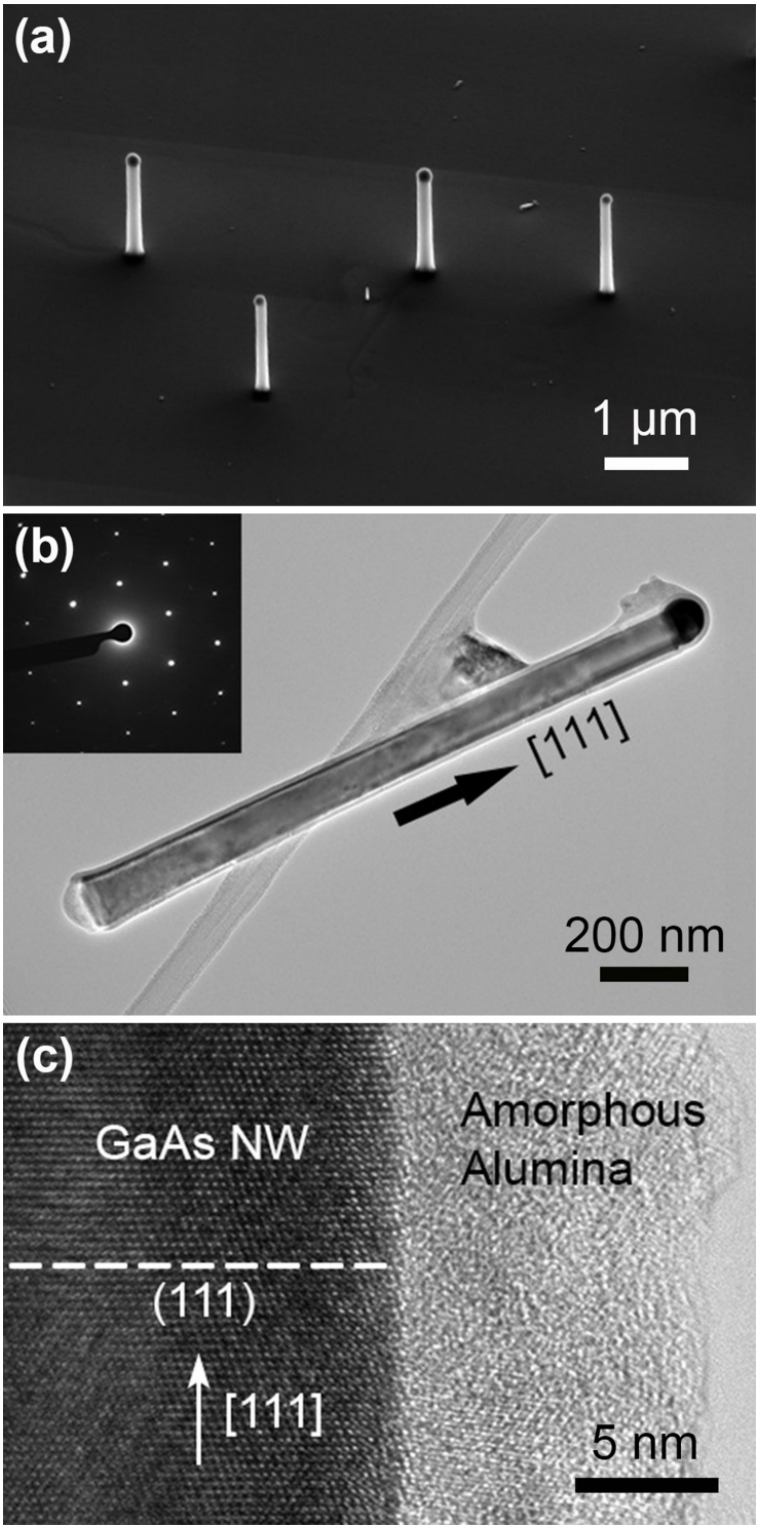

Figure 5-1 (a) An SEM image showing that the GaAs–a-Al_2O_3 core–shell NWs are oriented perpendicularly to the GaAs substrate surface. (b) A typical low magnification TEM image of a GaAs NW with a 10 nm thick a-Al_2O_3 shell. The inset is a corresponding SAED pattern. (c) An HRTEM image of the NW in (b).

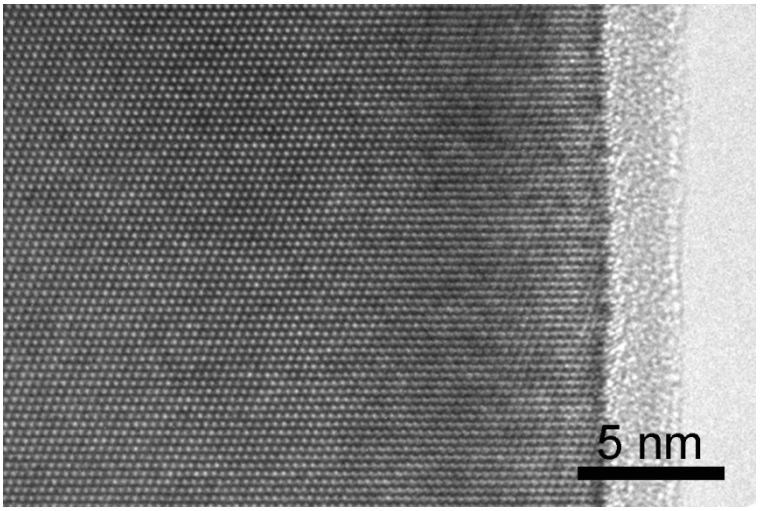

Figure 5-2 An HRTEM image of a GaAs NW with a native oxide layer on the surface.

Figure 5-3 provides a typical mechanical behaviour of a GaAs–a-Al_2O_3 core–shell NW with an a-Al_2O_3 shell thickness of 5 nm during *in situ* compression testing. The average diameter (including the core and the shell) of the core–shell NW, *d*, was ~ 110 nm. This diameter was defined as the average between the base and tip diameter values, because the tapering angle of the GaAs–a-Al_2O_3 core–shell NW is very small, there would not be a significant difference between the diameter measured at the largest buckling position and the diameter averaged from the base and tip. (The method of diameter measurement in this chapter is different from that in Chapter 4, where the diameter was measured at the largest buckling position of the NW because the tapering angle of the WZ-SF GaAs NWs is large, and the diameter measured at the largest buckling position is quite different from the diameter averaged from the base and tip.) The length of the NW, excluding the Au catalytic particle at the tip, was ~ 1,440 nm. Figure 5-3a presents the load-time curve (from 2.5 s to 9.5 s) with the inset providing the complete load–displacement–time curve of the whole test. Figures 5-3b–e provide a series of TEM images corresponding to points 1–4, respectively, in Figure 5-3a. At ~ 3.4 s, the flat punch makes contact with the Au particle at the tip of the NW, and the Au particle and the NW are compressed by an axial load *P*. With continuous displacement of the punch, the load increases. The NW starts to buckle at point 2 in Figure 5-3a, and this leads to a decrease in the load. The

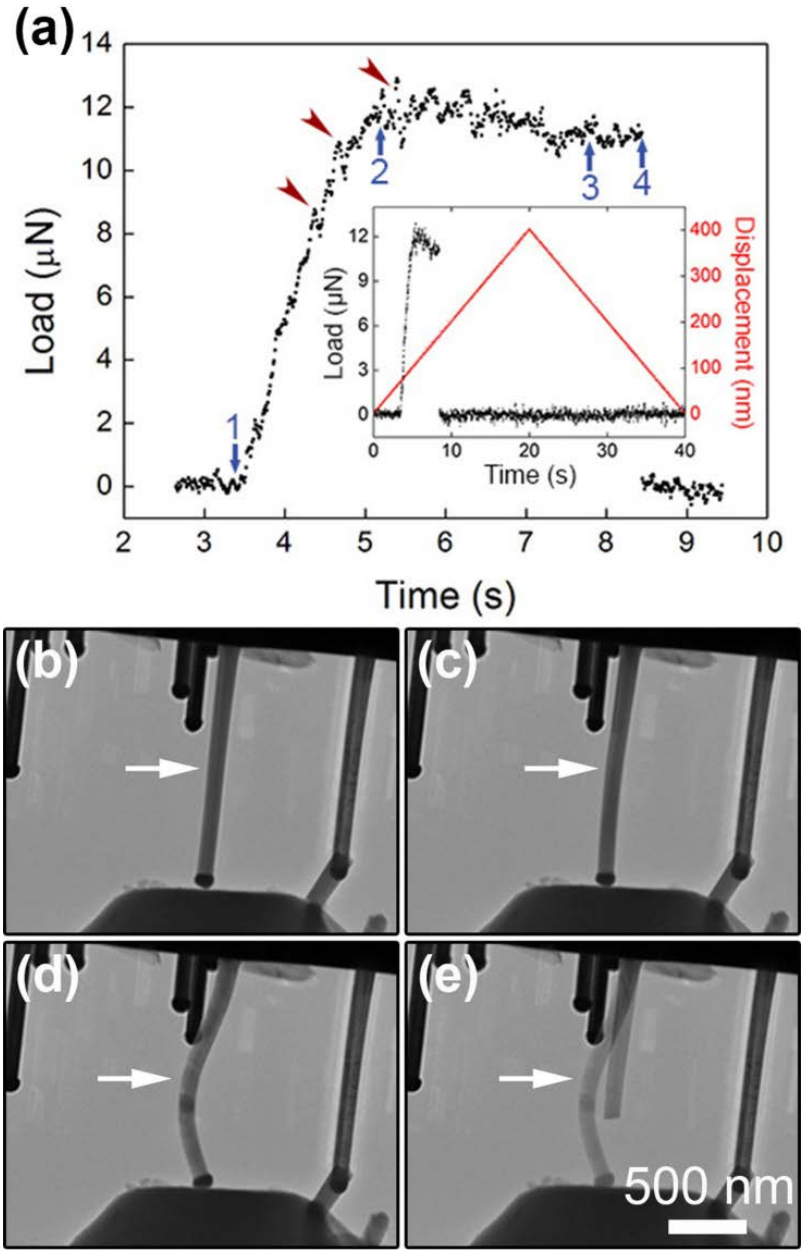

Figure 5-3 (a) A portion of a load-time curve (from 2.5 to 9.5 s) of an *in situ* compression process of a GaAs NW with a 5-nm thick a-Al_2O_3 shell. The inset shows the complete load-displacement-time curve of the whole compression process. The three arrowheads indicate load drops caused by plastic deformation of the Au particle at the tip of the NW. (b)–(e) A series of microscopy images corresponding to points 1 (before compression), 2 (starting point of buckling), 3, and 4 (fracture point), respectively, in (a). The white arrows in (b)–(e) point to the NW being tested.

critical load, P_{cr} at point 2 is ~ 12 μN. The load drops three times in this load-displacement curve, as indicated by the three arrowheads. These load drops are caused by the deformation of the Au particle, which does not affect the critical buckling load value that is the key to the analysis of the NW mechanical behaviour. The effect caused by the deformation of the Au particle can be removed by pre-deforming the Au particle but leaving the NW un-deformed before the test. For samples with shell thicknesses ranging from 2 to 25 nm, the NWs return to their original shapes when the external load is removed after buckling, but before fracture, indicating that the bending deformation is predominately elastic.

FEA analysis was used to accurately extract the maximum strain at failure of the tapered NWs based on the displacement of the NW tip at fracture measured from the *in situ* compression test. FEA models were created based on the experimental-measured dimensions and geometry of the NW samples. A typical meshed FEA NW model with a tapering angle of ~ 0.7° is shown in Figure 5-4. The model was meshed using C3D8R elements with a mesh size of 10 nm. Figures 5-5a–d present the FEA results of the maximum principal strains of the NW at different deformation stages indicated in Figures 5-5b–e, respectively. During the buckling deformation of the NW, the maximum principal strain, indicated by red in the contour plots, occurred near the tip of the NW. The principal strain of the NW increases when it is being compressed and bent, and finally reaches a value of 9.2% at fracture. The FEA results were consistent with the experimental observations. The location of the maximum principal strain shown in the contour plots is the point where the NW fractured in the compression test experiment.

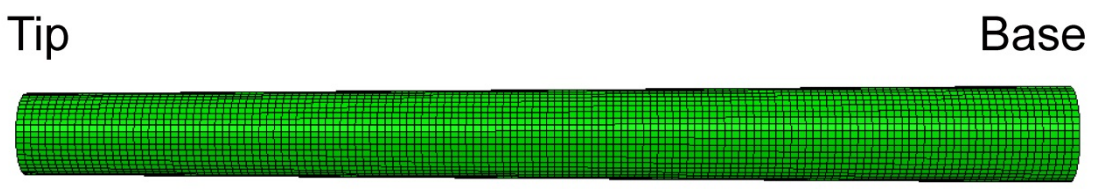

Figure 5-4 A typical tapered FEA NW model with a tapering angle of ~ 0.7°. The model was meshed using C3D8R elements with a mesh size of 10 nm.

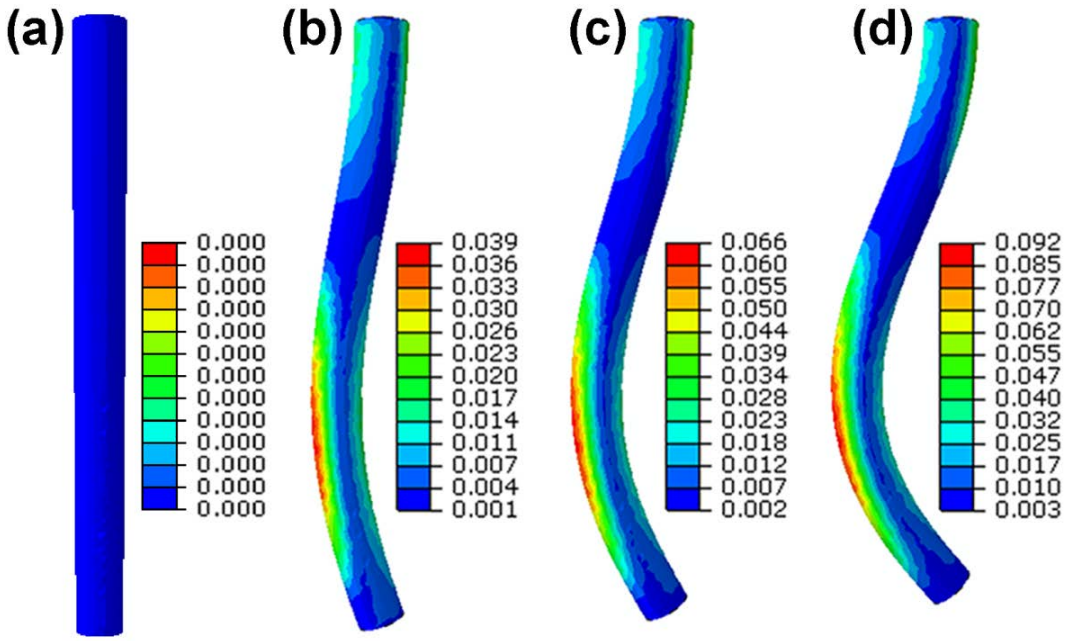

Figure 5-5 (a)–(d) FEA simulations of the maximum principal strain corresponding to the deformation state at Figures 5-3(b), (c), (d), and (e), respectively.

In addition to the maximum stain at failure, the Young's moduli of the GaAs–a-Al_2O_3 core–shell NWs with different shell thicknesses were also calculated using FEA based on the critical buckling loads measured from *in situ* compression tests of NWs. For the GaAs–a-Al_2O_3 core–shell NW with a shell thickness of 5 nm presented in Figure 5-3, the Young's modulus calculated from FEA is ~ 124 GPa. The results of the maximum strain at failure and the Young's modulus of the GaAs–a-Al_2O_3 core–shell NWs with different shell thicknesses are presented in Figure 5-6a and Figure 5-6b, respectively. The failure strain is approximately constant at between 8–10%, which is consistent with previous results for GaAs NWs with a native oxide shell [8]. This suggests that the thickness and the chemical composition of the a-Al_2O_3 shell do not affect the failure strain of the NWs, and that the large failure strains could be an intrinsic material property. These values are ~ 100 times larger than the failure strain of bulk GaAs [47]. Figure 5-6b shows that with decreasing a-Al_2O_3 shell thickness from 25 nm to 2 nm, the measured value of Young's modulus of the NWs first decreases from 143 GPa to 124 GPa at 5 nm, and then increases to 130 GPa when the shell thickness is 2 nm.

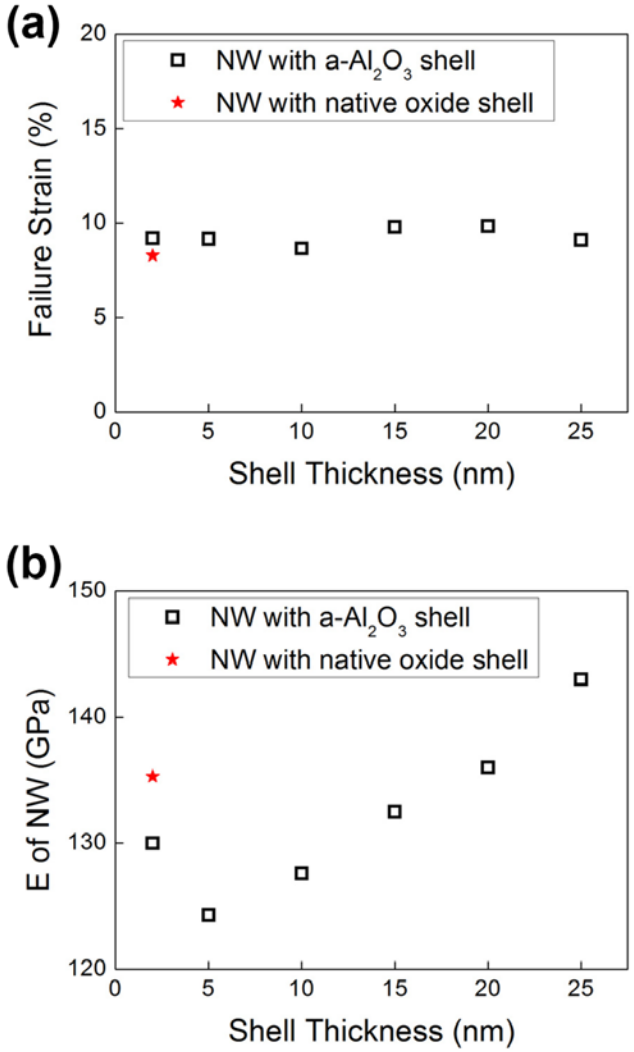

Figure 5-6 (a) The failure strain of GaAs core–shell NWs with different thicknesses of the a-Al_2O_3 shell (open squares) or with a 2 nm thick native oxide shell (red star). (b) Young's modulus of GaAs–a-Al_2O_3 NWs as a function of shell thickness. The red stars in (a) and (b) are the corresponding values for a GaAs NW with native oxide shell.

When a compressive force is applied to a core–shell structure, such as the NWs studied here, the strain experienced by the core (ε_C), the shell (ε_S), and the whole NW (ε_{NW}) is the same, and the compressive force (F_{NW}) is partitioned proportionately across both the core (F_C) and the shell (F_S) such that:

$$F_{NW} = F_C + F_S \qquad \textbf{5-1}$$

$$\varepsilon_{NW} = \varepsilon_C = \varepsilon_S \quad \textbf{5-2}$$

$$F_{NW} = (\varepsilon_{NW} E_{NW}) A_{NW} \quad \textbf{5-3}$$

$$F_C = (\varepsilon_C E_C) A_C \quad \textbf{5-4}$$

$$F_S = (\varepsilon_S E_S) A_S \quad \textbf{5-5}$$

$$E_{NW} A_{NW} = E_C A_C + E_S A_S \quad \textbf{5-6}$$

Here, E_{NW}, E_C, and E_S are the Young's modulus of the core–shell structure, GaAs core, and a-Al_2O_3 shell, respectively. E_S is a function of shell thickness. A_{NW}, A_C, and A_S are the cross-sectional area of the core–shell structure, GaAs core, and a-Al_2O_3 shell, respectively. Rearranging Equation 5-6 in terms of shell thickness t_S and core–shell NW radius R (including the shell), the following equations have been obtained:

$$E_{NW}(\pi R^2) = E_C\left[\pi (R - t_S)^2\right] + E_S\left[\pi R^2 - \pi (R - t_S)^2\right] \quad \textbf{5-7}$$

$$E_S = E_C + (E_{NW} - E_C)\frac{R^2}{2t_S R - t^2} \quad \textbf{5-8}$$

Since the Young's moduli of the NWs with shell thicknesses from ~ 2 nm to 25 nm have been measured and shown in Figure 5-6b, by first assuming that E_C is equal to that of bulk GaAs, i.e., $E_C = E_{Bulk}$ = 86 GPa [227], calculations using Equation 5-8 show that the Young's modulus of the shell E_S does not change with thickness t_S when the thickness is equal to or larger than 20 nm. Thus, the data for core–shell structures with shell thickness of 20 nm and 25 nm are used to deduce the true value of E_C. The results show that the Young's modulus for the shell with a thickness of 20 nm (E_{S20}) and 25 nm (E_{S25}) is 191.3 GPa and E_C is 83 GPa. Taking E_C = 83 GPa and the measured E_{NW} for different t_S into Equation 5-6, the Young's modulus of the a-Al_2O_3 shell was calculated as a function of shell thickness, as plotted in Figure 5-7. Our results reveal that the Young's modulus of the a-Al_2O_3 shell increases from 191.3 GPa to 669.2 GPa as the shell thickness is decreased from 25 nm to 2 nm. It is evident that the Young's modulus of the shell is thickness-dependent from 10 nm to 2 nm and varies sharply when the thickness is less than 5 nm. Note that the value of the Young's modulus of the shell is almost doubled when the thickness is decreased from

5 nm to 2 nm. Such a dramatic increase of Young's modulus has never been observed for nanostructures with a size greater than 15 nm. This is the first experimental measurement of an elastic property of a nanostructured material with dimensions below 15 nm. Similar phenomena have been predicted for ZnO nanofilms and nanowires by atomistic simulations [115, 130, 138].

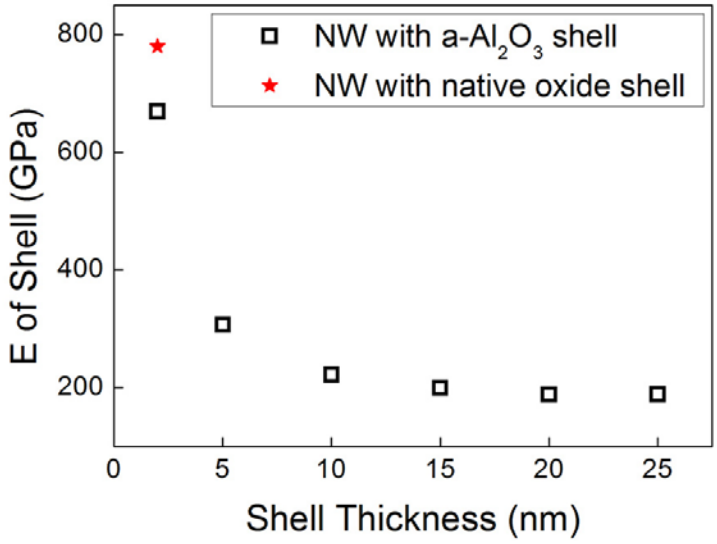

Figure 5-7 Young's modulus of a-Al_2O_3 as a function of shell thickness. The red star corresponds the value for a GaAs NW with a native oxide shell.

For GaAs NWs without the a-Al_2O_3 coating, oxidation on the NW surface occurred when the NWs were removed from the growth chamber and exposed to air. The native oxide layer usually has a thickness of ~ 2 nm. The failure strain and the Young's modulus of GaAs NWs with a native oxide layer on the surface were also measured in this study, and the results are presented in Figure 5-6 (and indicated with red stars). The Young's modulus of GaAs–native-oxide core–shell NWs with different NW diameters and approximately the same native oxide shell thickness has been reported in a previous work [8]. The experimentally-measured Young's modulus of GaAs–native-oxide core–shell NWs in this study matches well with that of NWs with similar diameters reported in the previous work [8]. Using the method outlined earlier for a-Al_2O_3 shells, the Young's modulus of the native oxide with a shell thickness of

2 nm was determined to be ~ 776 GPa (Figure 5-7). Native oxide surface layers have been reported to be responsible for the size dependency of different nanomaterials, including W nanobelts [222], Si nanocantilevers [232], Si nano-scale beam [233], Si NWs [124], Ag NWs [58], and CuO NWs [60].

5.3 Discussion

Elastic strain limit is the largest strain before plastic deformation. When materials are deformed beyond their elastic limit, plastic deformation occurs via the activation of dislocation motion and/or twinning. Although dislocations exist in most compound materials, e.g., GaAs, in which ionic and/or covalent bonds are directional and hence few dislocation slip systems are available, the motion of these dislocations is very difficult. Therefore, ceramic materials, such as GaAs, are naturally brittle at room temperature. They usually fracture in the brittle mode with little (< 0.1%) or no plastic strain [47]. A fracture process involves two steps: crack formation and propagation. For brittle materials, cracks usually initiate at microscopic flaws or imperfections that exist at the surface and within the interior of the materials. Moreover, since plastic deformation is impossible in ceramics, it is not possible to blunt the crack tip. These flaws significantly reduce the fracture stress and fracture strain because an applied stress may be significantly amplified or concentrated at the tip of a flaw, which makes the material fracture at a strain far below its elastic limit.

It is well known that reducing the dimensions of materials reduces the probability of having a flaw in the materials. Typical HRTEM images of GaAs–a-Al_2O_3 core–shell NWs and GaAs NWs, in Figure 5-1c and Figure 5-2, respectively, show no defect in the core, the shell, and the core–shell interface of the NWs. The perfect structure effectively suppresses crack initiation in the NWs during the loading process that increases the failure strain of the NWs. Therefore, the fracture strain of GaAs–a-Al_2O_3 core–shell NWs with no pre-existing defects is significantly higher than that of their bulk counterparts because the mechanism of crack initiation through flaws is absent.

It has been widely accepted that surface reconstruction plays a key role on the size-dependency of Young's modulus [72, 76, 115, 134]. The local bonding environment of atoms at or near the surface is distinct from that in the bulk. The termination of the lattice periodicity in the surface causes an imperfection of the coordination number – the total number of neighbours of a central atom – of the surface atoms, resulting in the remaining bonds of this lower-coordinated surface atom to relax and raise the binding energy and surface stress [234]. The relaxed bond is stronger. Surface stress, which always exists at a free surface of a solid material, drives the surface reconstruction [235]. The average bond length contracts on the surface as a result of surface reconstruction [235]. For example, for FCC materials such as Au, with (100) surface, the surface is reconstructed to a hexagonal surface layer that decreases the bonding length. For materials with close-packed (111) surface, the bond length contraction occurs without changing the surface atomic array [235]. As the Young's modulus is inversely proportional to the bond length [236], the surface usually exhibits a much higher Young's modulus than the interior.

In addition to surface effect, a similar situation occurs at an interface between two dissimilar media. For core–shell and film/substrate materials structures where a coherent epitaxial relationship exists between the core and the shell – or the film and the substrate – the mechanical properties, such as Young's modulus, of the shell or film is inevitably affected by the interfacial lattice stress that might significantly displace interfacial atoms from their equilibrium positions, and the lattice stress at the interface is a function of shell/film thickness [223, 224, 237]. Even though there is no coherent interface – that is, no interfacial stress induced by the lattice mismatch in the core–shell NWs studied here – the incoherent GaAs–a-Al_2O_3 core–shell interface also affects the bonding, and therefore Young's modulus, at the interface. Hence, the interfacial effect cannot be excluded. Because the only structural variable in the GaAs–a-Al_2O_3 core–shell NWs is shell thickness, it is concluded that the size dependency of Young's modulus of the a-Al_2O_3 shell originates mainly from the size dependency of the volume fraction of the surface and GaAs-Al_2O_3 interface. The volume fraction here refers to the ratio between the volume of the reconstructed surface and the interfacial layer, and the volume of the a-Al_2O_3 shell. Since the thicknesses of surface and interfacial layer are unknown, no quantitative datum is available.

Note that the Young's modulus of the a-Al_2O_3 shell measured from this study may be slightly different to that of the native oxide film formed on the surface of bulk Al due to the difference between the GaAs-Al_2O_3 interface and the Al-Al_2O_3 interface. As discussed in Chapter 4, the interface between the core and the shell affects the measured Young's modulus of the shell.

5.4 Conclusions

An experiment to measure the elastic modulus of amorphous Al_2O_3 films with thicknesses varying between 2 nm and 25 nm was designed. The amorphous Al_2O_3 was in the form of a shell wrapped around GaAs nanowires, thereby forming an effective core–shell structure. The GaAs core comprised a single crystal structure with a diameter of 100 nm. Combined *in situ* compression TEM and FEA were used to evaluate the elastic modulus of the overall core–shell nanowires. A core–shell model was applied to de-convolute the elastic modulus of the Al_2O_3 shell from the core. This method has been successfully applied to study the thickness effect on the Young's modulus of a-Al_2O_3 films (shells). We conclude the following:

1. The elastic modulus of amorphous Al_2O_3 increases significantly when the thickness of the layer is smaller than 5 nm. This can be attributed to the re-construction of the bonding at the surface of the material, coupled with the increase of the surface-to-volume ratio with nanoscale dimensions.

2. The fracture strain of GaAs–a-Al_2O_3 core–shell NWs is significantly higher than that of their bulk counterparts because there are no pre-existing defects in the NWs, and the mechanism of early crack initiation through structural flaws is absent.

3. The experimental technique and analysis methods presented in this study may be extended to measure the elastic moduli of other materials with dimensions of just several nanometers.

6 Conclusions and future perspectives

This chapter summarises the major results obtained in this thesis and suggests a several further research directions.

6.1 Conclusions

The mechanical behaviours of nanostructured materials including NWs and nanofilms have been investigated using *in situ* TEM compression combined with FEA. The following conclusions are drawn, which provide potential guidance on mechanical characterisation of low-dimensional nanostructures and tailoring mechanical properties of NWs through the control of their microstructures:

1. Tapering of NWs and loading misalignment have significant impact on the measured mechanical properties of NWs. For example, in a uniaxial compression test of NWs, ignoring the tapering angle of 0.8° and loading misalignment of 6° will result in underestimating the critical buckling stress and calculated Young's modulus using the Euler's formula by 7% and 13%, respectively. Compared with the effects of tapering and loading misalignment on the uniaxial compression testing results of a NW, tapering affects uniaxial tensile testing results more significantly, while loading misalignment does not have a significant effect on the calculated results based on the tensile test data. In a uniaxial tensile test of NWs, ignoring the tapering angle of 0.8° and loading misalignment of 6° will lead to an underestimation of the tensile fracture strength and Young's modulus calculated from the measured fracture load by 37% and 3%, respectively.

2. Inclusion of the effects of tapering and loading misalignment in the compression and tensile data analysis is crucial for accurate determination of the mechanical properties of NWs. If a slight loading misalignment exists in a tensile test of NWs, tensile fracture strength can be accurately determined by using the cross-sectional area at the fracture site.

3. The presence of a high-density of SFs leading to the formation of short polytypic segments results in an increase of the Young's modulus of GaAs NWs. The stiffening effect of SFs is attributed to the change of the interatomic bonding at the SFs. The findings provide a better understanding of the effect of high-density SFs on Young's modulus, and potential guidance in using defect engineering to tailor mechanical properties of nanostructures.

4. The Young's moduli of both WZ and WZ-SF GaAs NWs increase with decreasing NW diameter, which is caused by the increase of the volume ratio of the amorphous shell of the NWs with decreasing NW diameter. Quantitative analysis showed that by decreasing the diameters of the WZ NWs from 170 nm to 75 nm and the WZ-SF NWs from 151 to 77 nm, the Young's modulus of the NWs was enhanced from 161 GPa to 189 GPa and from 183 GPa to 203 GPa, respectively.

5. The crystalline structure of the core is important in determining the thickness and the Young's modulus of the amorphous native oxide shell in the NWs. Due to the slightly thicker than average interfacial thickness for WZ-SF NWs caused by the wavy interfacial structure of WZ-SF, the shell thickness for WZ-SF NWs is 2.8 nm, which is 0.3 nm thicker than that of WZ NWs. The Young's modulus of the amorphous native oxide shell in the WZ NWs is 8% larger than that in WZ-SF NWs. The Young's modulus of the interfacial area between the amorphous shell and the crystalline core varies with the crystalline structure of the core.

6. The Young's moduli of nanoscale films with thicknesses down to several nanometers can be measured by using a core–shell NW structure with a constant core diameter and varying shell thicknesses. *In situ* TEM compression and FEA were used to determine the Young's modulus of the core–shell NWs. The Young's modulus of the shell of varying thickness was then extracted using a core–shell model. The experimental technique and analysis methods presented in this study may be extended to measure the elastic modulus of other materials with dimensions of just several nanometers.

7. The elastic modulus of a-Al_2O_3 shells (thin films) of the GaAs–a-Al_2O_3 core–shell NW increases significantly when the thickness of the layer is less than 5 nm. This phenomenon can be attributed to the re-construction of the bonding on the surface of the material, coupled with the increase of the surface-to-volume ratio with reducing materials dimensions. The fracture strain of GaAs–a-Al_2O_3 core–shell NWs is significantly higher than that of their bulk counterparts because there are no pre-existing defects in the NWs and the mechanism of crack initiation through flaws is absent.

6.2 Future work

Although several important conclusions have been achieved throughout this thesis project, there still exist many unsolved issues on the mechanical behaviours of nanomaterials, and further thorough investigations are needed in the future as the extension of this thesis project.

1. Nanomaterials can apparently sustain larger elastic and plastic strains than conventional materials. The plastic deformation mechanisms and fracture process in nanomaterials could be considerably different to those of their bulk counterparts. All GaAs NWs with various crystalline structures and diameters ranging from 75 nm to 170 nm tested under compression in this thesis deformed elastically until fracture. Similarly, no plastic deformation was observed for GaAs NWs with diameters ~ 50 nm during tensile tests performed by using the thermal bimetallic technique (data not presented in this thesis). However, obvious plastic deformation was observed in NWs with diameters less than 25 nm under compression, leaving behind stacking faults on {111} planes [8]. Clearly a small diameter plays a critical role in the plastic deformation of the NWs. However, the critical diameter that allows plastic deformation is not clear. It is also not clear if the loading mode also plays a role. Therefore, it is necessary to test GaAs NWs with diameters in the range between 20 nm and 50 nm to determine the largest diameter that would experience plastic deformation under compression, and to conduct theoretical analysis of the physics of the size effect on plastic deformation. It is also

necessary to carry out deformation under different deformation modes (tensile, compression, and bending) to understand the effect of deformation mode on the plastic deformation behaviour of NWs. Atomic-scale observation of plastic deformation processes is critical for revealing plastic deformation mechanisms, including deformation twinning and the nucleation, motion, and interaction of dislocations. Most of the current *in situ* straining TEM holders have only single-tilt capability, making it impossible to image materials at atomic resolution. A double-tilt capability is essential for atomic-scale observation of the deformation processes of NWs, and this can be realised using the copper grid technique [9] and the thermal bimetallic technique [91], as discussed in Section 1.4.1 and Section 1.4.3, respectively. However, these two techniques do not provide any stress–strain or load–displacement curve.

2. Just as planar defects are critical in determining the mechanical behaviour of bulk metallic materials [214-217], crystalline defects might also significantly affect the deformation behaviours of GaAs NWs. However, whether twin boundaries and SFs have effects on dislocation behaviour, and how NWs with defects accommodate plastic deformation, remains unclear. Therefore, in addition to the defect-free GaAs NWs, atomic-scale investigation of the deformation mechanisms of NWs with crystalline defects, such as twin boundaries and SFs, is also needed. The effects of orientation and density of the crystalline defects in NWs on their deformation mechanisms should be studied as well.

3. In my PhD research, the elastic properties, including Young's modulus and elastic strain, of GaAs NWs were measured through combined *in situ* TEM compression and FEA. However, some other mechanical properties of NWs, for example, tensile or bending fracture strength and strain, were not measured although these properties are also important for their applications as building blocks of nano-devices or as components for composite materials. By using the Hysitron PI95 PicoIndenter combined with PTP devices, I found that the tensile fracture strength of ZB GaAs NWs with a diameter of 265 nm reaches 6.16 GPa, which is already close to its theoretical value (~ 8.6 GPa, which is $E/10$). So far, only NWs with diameters more than 200 nm have been tested. It

is not clear if the high tensile fracture strength is an intrinsic property of defect-free ZB GaAs NWs or whether NW dimensions play a role. It is necessary to carry out tensile tests of GaAs NWs with different sizes. Sample preparation for tensile tests of NWs using PTP devices is very difficult. The smallest diameter of NWs can be manipulated is ~ 50 nm. Further, testing of NWs with very small diameters would also challenge the sensitivity limit of the holder.

4. As mentioned in Section 1.5.3, single-crystal WZ GaAs NWs with small diameters (e.g., 25 nm) demonstrate anelasticity [84], which was attributed to the interfacial effect between the amorphous layer and the crystalline core. Anelasticity was also found in single-crystalline ZnO NWs with diameters of 38 nm–65 nm, and was explained as a result of stress-gradient-induced migration of point defects [165].

   Recent multiple compression experiments (by the author with colleagues, unpublished) of a WZ GaAs NW with a diameter of ~ 10 nm revealed that the so-called “anelasticity” was probably recovered plastic deformation triggered by the electron beam in TEM: the NW was uniaxially compressed and it did not return to its original shape after the external load was released. After the release of the load, the entire NW was exposed to a dispersed electron beam with low current intensity and a converged electron beam with high current intensity, after which the NW returned to its original shape in 10 minutes and 1 minute, respectively. However, when the electron beam was closed for ~ 1 hour, the NW remained at its deformed state. It took ~ 10 minutes for recovery after the electron beam was re-opened and spread to a low current intensity. Detailed quantitative and atomic scale observations as well as molecular dynamics simulations of the process are needed to understand this phenomenon and its underlying mechanism.

5. Twinning superlattices (TSL) or periodic arrangements of twin planes have recently been reported for a variety of III–V NWs, including InAs, InP, GaP, and GaAs. NWs with TSL structures have generated particular interest. It has been predicted that periodic twinning in III–V NWs introduces electronic miniband structures, which may be useful for bandgap engineering, as well as

direct intersubband optical transitions. To design and fabricate reliable nano-devices using III–V NWs with TSL structures, a clear understanding of their mechanical properties is necessary. TSL NWs show a periodic oscillation in sidewall facet orientation, appearing as a zigzagged sidewall of the NWs in 2-D TEM images [221]. The irregular NW morphology makes the quantitative mechanical testing data analysis extremely difficult. This difficulty can be overcome by combining *in situ* TEM mechanical testing with FEA. The FEA models will be created based on the real dimensions and morphology of the TSL NWs. NWs with different diameters should be investigated to check if there is any size effect on the mechanical properties of GaAs NWs with TSL structures. It is also necessary to study the effect of the spacing between the periodic twin planes on the mechanical properties of NWs.

6. Heterostructure NWs have been extensively investigated but the major focuses have been on their synthesis and physical properties. There are few studies, especially experimental studies, on the mechanical properties of NWs with heterostructures, including axial heterostructures and core–shell heterostructures [238, 239]. Heterostructure NWs have exhibited promising applications. Assessing the mechanical properties of NWs with heterostructures is not only important for their applications, but also has potential for fundamental insight into the mechanical behaviours of heterostructures with lattice mismatch strain at the heterogeneous interface. The volume fraction of the core and the shell in core–shell heterostructures may affect the bond lengths and the strains around the interface [240]. Investigation of the mechanical properties of core–shell heterostructures with different core/shell volume ratios could provide an understanding of the interfacial effect on the mechanical behaviours of core–shell heterostructures. Detailed quantitative mechanical testing and molecular dynamics simulations of the deformation process are needed to understand the measured mechanical properties and the underlying mechanism.

7 References

[1] C.M. Lieber, MRS Bull., 28 (2003) 486-491.

[2] F. Qian, S. Gradecak, Y. Li, C.Y. Wen, C.M. Lieber, Nano Lett., 5 (2005) 2287-2291.

[3] P.D. Yang, MRS Bull., 30 (2005) 85-91.

[4] C.M. Lieber, Z.L. Wang, MRS Bull., 32 (2007) 99-108.

[5] J.-G. Guo, Y.-P. Zhao, J. Appl. Phys., 98 (2005) 074306.

[6] E. Kapon, D.M. Hwang, R. Bhat, Phys. Rev. Lett., 63 (1989) 430-433.

[7] P.M. Petroff, G. Medeiros-Ribeiro, MRS Bull., 21 (1996) 50-54.

[8] Y.B. Wang, L.F. Wang, H.J. Joyce, Q. Gao, X.Z. Liao, Y.-W. Mai, H.H. Tan, J. Zou, S.P. Ringer, H.J. Gao, C. Jagadish, Adv. Mater., 23 (2011) 1356-1360.

[9] L.H. Wang, P. Liu, P.F. Guan, M.J. Yang, J.L. Sun, Y.Q. Cheng, A. Hirata, Z. Zhang, E. Ma, M.W. Chen, X.D. Han, Nat. Comm., 4 (2013) 2413.

[10] P.T. Bao, Y.B. Wang, X.Y. Cui, Q. Gao, H.-W. Yen, H.W. Liu, W.K. Yeoh, X.Z. Liao, S.C. Du, H.H. Tan, C. Jagadish, J. Zou, S.P. Ringer, R.K. Zheng, Appl. Phys. Lett., 104 (2014) 021904.

[11] Y.J. Chen, Q. Gao, Y.B. Wang, X.H. An, X.Z. Liao, Y.-W. Mai, H.H. Tan, J. Zou, S.P. Ringer, C. Jagadish, Nano Lett., 15 (2015) 5279-5283.

[12] D.-M. Tang, C.-L. Ren, M.-S. Wang, X.L. Wei, N. Kawamoto, C. Liu, Y. Bando, M. Mitome, N. Fukata, D. Golberg, Nano Lett., 12 (2012) 1898-1904.

[13] F. Xu, Q.Q. Qin, A. Mishra, Y. Gu, Y. Zhu, Nano Res., 3 (2010) 271-280.

[14] Y. Cui, Q.Q. Wei, H.K. Park, C.M. Lieber, Science, 293 (2001) 1289-1292.

[15] J. Hahm, C.M. Lieber, Nano Lett., 4 (2004) 51-54.

[16] F. Patolsky, B.P. Timko, G.H. Yu, Y. Fang, A.B. Greytak, G.F. Zheng, C.M. Lieber, Science, 313 (2006) 1100-1104.

[17] X.D. Wang, J.H. Song, J. Liu, Z.L. Wang, Science, 316 (2007) 102-105.

[18] M.H. Huang, S. Mao, H.N. Feick, H.Q. Yan, Y.Y. Wu, H. Kind, E. Weber, R. Russo, P.D. Yang, Science, 292 (2001) 1897-1899.

[19] M. Law, L.E. Greene, J.C. Johnson, R. Saykally, P.D. Yang, Nat. Mater., 4 (2005) 455-459.

[20] B.Z. Tian, X.L. Zheng, T.J. Kempa, Y. Fang, N.F. Yu, G.H. Yu, J.L. Huang, C.M. Lieber, Nature, 449 (2007) 885-889.

[21] E. Garnett, P.D. Yang, Nano Lett., 10 (2010) 1082-1087.

[22] D.Y. Li, Y.Y. Wu, P. Kim, L. Shi, P.D. Yang, A. Majumdar, Appl. Phys. Lett., 83 (2003) 2934-2936.

[23] A.I. Hochbaum, R. Chen, R.D. Delgado, W.J. Liang, E.C. Garnett, M. Najarian, A. Majumdar, P.D. Yang, Nature, 451 (2008) 163-167.

[24] Y. Cui, Z.H. Zhong, D.L. Wang, W.U. Wang, C.M. Lieber, Nano Lett., 3 (2003) 149-152.

[25] D.W. Wang, Q. Wang, A. Javey, R. Tu, H.J. Dai, H. Kim, P.C. McIntyre, T. Krishnamohan, K.C. Saraswat, Appl. Phys. Lett., 83 (2003) 2432-2434.

[26] Y. Huang, C.M. Lieber, Pure Appl. Chem., 76 (2004) 2051-2068.

[27] M. Chau, O. Englander, L.W. Lin, Proceedings of the 3rd IEEE Conference on Nanotechnology, IEEE, San Francisco, CA, 2003, pp. 879-880.

[28] X.F. Duan, Y. Huang, Y. Cui, J.F. Wang, C.M. Lieber, Nature, 409 (2001) 66-69.

[29] Z.H. Zhong, F. Qian, D.L. Wang, C.M. Lieber, Nano Lett., 3 (2003) 343-346.

[30] Y. Huang, X.F. Duan, C.M. Lieber, Small, 1 (2005) 142-147.

[31] T. Martensson, C.P.T. Svensson, B.A. Wacaser, M.W. Larsson, W. Seifert, K. Deppert, A. Gustafsson, L.R. Wallenberg, L. Samuelson, Nano Lett., 4 (2004) 1987-1990.

[32] M. Bhaskaran, S. Sriram, S. Ruffell, A. Mitchell, Adv. Funct. Mater., 21 (2011) 2251-2257.

[33] P. Mitra, A.P. Chatterjee, H.S. Maiti, Mater. Lett., 35 (1998) 33-38.

[34] D.W. Carr, S. Evoy, L. Sekaric, H.G. Craighead, J.M. Parpia, Appl. Phys. Lett., 75 (1999) 920-922.

[35] M. Yazawa, M. Koguchi, A. Muto, M. Ozawa, K. Hiruma, Appl. Phys. Lett., 61 (1992) 2051-2053.

[36] M. Yazawa, M. Koguchi, A. Muto, K. Hiruma, Adv. Mater., 5 (1993) 577-580.

[37] Y. Kim, H.J. Joyce, O. Gao, H.H. Tan, C. Jagadish, M. Paladugu, J. Zou, A.A. Suvorova, Nano Lett., 6 (2006) 599-604.

[38] H.J. Joyce, Q. Gao, H.H. Tan, C. Jagadish, Y. Kim, X. Zhang, Y.N. Guo, J. Zou, Nano Lett., 7 (2007) 921-926.

[39] A. Mishra, L.V. Titova, T.B. Hoang, H.E. Jackson, L.M. Smith, J.M. Yarrison-Rice, Y. Kim, H.J. Joyce, Q. Gao, H.H. Tan, C. Jagadish, Appl. Phys. Lett., 91 (2007) 263104.

[40] P. Parkinson, H.J. Joyce, Q. Gao, H.H. Tan, X. Zhang, J. Zou, C. Jagadish, L.M. Herz, M.B. Johnston, Nano Lett., 9 (2009) 3349-3353.

[41] H.J. Joyce, J. Wong-Leung, Q. Gao, H.H. Tan, C. Jagadish, Nano Lett., 10 (2010) 908-915.

[42] R.S. Wagner, W.C. Ellis, Appl. Phys. Lett., (1964) 89-90.

[43] D.L. Dheeraj, H.L. Zhou, A.F. Moses, T.B. Hoang, A.T.J. Van Helvoort, B.O. Fimland, H. Weman, Heterostructured III-V Nanowires with Mixed Crystal Phases Grown by Au-assisted Molecular Beam Epitaxy, Nanowires, InTech, 2010.

[44] J.W. Dailey, J. Taraci, T. Clement, D.J. Smith, J. Drucker, S.T. Picraux, J. Appl. Phys., 96 (2004) 7556-7567.

[45] H.J. Joyce, Q. Gao, H.H. Tan, C. Jagadish, Y. Kim, M.A. Fickenscher, S. Perera, T.B. Hoang, L.M. Smith, H.E. Jackson, J.M. Yarrison-Rice, X. Zhang, J. Zou, Adv. Funct. Mater., 18 (2008) 3794-3800.

[46] H.J. Joyce, Q. Gao, H.H. Tan, C. Jagadish, Y. Kim, M.A. Fickenscher, S. Perera, T.B. Hoang, L.M. Smith, H.E. Jackson, J.M. Yarrison-Rice, X. Zhang, J. Zou, Nano Lett., 9 (2009) 695-701.

[47] W.D. Callister, D.G. Rethwisch, Materials Science and Engineering: An introduction, 8th ed., John Wiley & Sons, Inc., New York, 2009.

[48] A. Holden, B. Sammler, B.L. Powers, S.A. Schmidt, Structural Design for the Stage, 2nd ed., Focal Press, Oxford, 2015.

[49] S.P. Timoshenko, J.M. Gere, Theory of elastic stability, second ed., McGraw-Hill, New York, 1961.

[50] S. Hoffmann, I. Utke, B. Moser, J. Michler, S.H. Christiansen, V. Schmidt, S. Senz, P. Werner, U. Gosele, C. Ballif, Nano Lett., 6 (2006) 622-625.

[51] C.Q. Chen, J. Zhu, Appl. Phys. Lett., 90 (2007) 043105-043105.

[52] S. Hoffmann, F. Oestlund, J. Michler, H.J. Fan, M. Zacharias, S.H. Christiansen, C. Ballif, Nanotechnology, 18 (2007) 205503.

[53] J.H. Song, X.D. Wang, E. Riedo, Z.L. Wang, Nano Lett., 5 (2005) 1954-1958.

[54] S.L. Wang, Y.H. He, H. Huang, J. Zou, G.J. Auchterlonie, L.Z. Hou, B.Y. Huang, Nanotechnology, 24 (2013) 285703.

[55] S.L. Wang, Y.Q. Wu, L.W. Lin, Y.H. He, H. Huang, Small, 11 (2015) 1672-1676.

[56] A. San Paulo, J. Bokor, R.T. Howe, R. He, P. Yang, D. Gao, C. Carraro, R. Maboudian, Appl. Phys. Lett., 87 (2005) 053111.

[57] B. Wu, A. Heidelberg, J.J. Boland, Nat. Mater., 4 (2005) 525-529.

[58] G.Y. Jing, H.L. Duan, X.M. Sun, Z.S. Zhang, J. Xu, Y.D. Li, J.X. Wang, D.P. Yu, Phys. Rev. B, 73 (2006) 235409.

[59] H. Ni, X.D. Li, H.S. Gao, Appl. Phys. Lett., 88 (2006) 043108-043108.

[60] E.P.S. Tan, Y. Zhu, T. Yu, L. Dai, C.H. Sow, V.B.C. Tan, C.T. Lim, Appl. Phys. Lett., 90 (2007) 163112.

[61] B.M. Wen, J.E. Sader, J.J. Boland, Phys. Rev. Lett., 101 (2008) 175502.

[62] P.-H. Sung, C.-D. Wu, T.-H. Fang, C.-I. Weng, Appl. Surf. Sci., 258 (2012) 7064-7069.

[63] K. Davami, B. Mortazavi, H.M. Ghassemi, R.S. Yassar, J.-S. Lee, Y. Remond, M. Meyyappan, Nanoscale, 4 (2012) 897-903.

[64] X.D. Han, Y.F. Zhang, X.Q. Liu, Z. Zhang, Y.J. Hao, X.Y. Guo, J. Appl. Phys., 98 (2005) 124307.

[65] X.D. Han, K. Zheng, Y.F. Zhang, X.N. Zhang, Z. Zhang, Z.L. Wang, Adv. Mater., 19 (2007) 2112-2118.

[66] X.D. Han, Y.F. Zhang, K. Zheng, X.N. Zhang, Z. Zhang, Y.J. Hao, X.Y. Guo, J. Yuan, Z.L. Wang, Nano Lett., 7 (2007) 452-457.

[67] K. Zheng, X.D. Han, L.H. Wang, Y.F. Zhang, Y.H. Yue, Y. Qin, X.N. Zhang, Z. Zhang, Nano Lett., 9 (2009) 2471-2476.

[68] K. Zheng, C.C. Wang, Y.-Q. Cheng, Y.H. Yue, X.D. Han, Z. Zhang, Z.W. Shan, S.X. Mao, M.M. Ye, Y.D. Yin, E. Ma, Nat. Comm., 1 (2010) 24.

[69] L.H. Wang, K. Zheng, Z. Zhang, X.D. Han, Nano Lett., 11 (2011) 2382-2385.

[70] P. Poncharal, Z.L. Wang, D. Ugarte, W.A. de Heer, Science, 283 (1999) 1513-1516.

[71] D.A. Dikin, X. Chen, W. Ding, G. Wagner, R.S. Ruoff, J. Appl. Phys., 93 (2003) 226-230.

[72] C.Q. Chen, Y. Shi, Y.S. Zhang, J. Zhu, Y.J. Yan, Phys. Rev. Lett., 96 (2006) 075505.

[73] K.H. Liu, W.L. Wang, Z. Xu, L. Liao, X.D. Bai, E.G. Wang, Appl. Phys. Lett., 89 (2006) 221908-221908.

[74] C.Y. Nam, P. Jaroenapibal, D. Tham, D.E. Luzzi, S. Evoy, J.E. Fischer, Nano Lett., 6 (2006) 153-158.

[75] P. Jaroenapibal, D.E. Luzzi, S. Evoy, S. Arepalli, Appl. Phys. Lett., 85 (2004) 4328-4330.

[76] S. Cuenot, C. Fretigny, S. Demoustier-Champagne, B. Nysten, Phys. Rev. B, 69 (2004) 165410.

[77] A.M. Minor, S.A.S. Asif, Z.W. Shan, E.A. Stach, E. Cyrankowski, T.J. Wyrobek, O.L. Warren, Nat. Mater., 5 (2006) 697-702.

[78] Z.W. Shan, R.K. Mishra, S.A.S. Asif, O.L. Warren, A.M. Minor, Nat. Mater., 7 (2008) 115-119.

[79] R. Nowak, D. Chrobak, S. Nagao, D. Vodnick, M. Berg, A. Tukiainen, M. Pessa, Nat. Nanotechnol., 4 (2009) 287-291.

[80] J.Y. Huang, H. Zheng, S.X. Mao, Q.M. Li, G.T. Wang, Nano Lett., 11 (2011) 1618-1622.

[81] H. Guo, K. Chen, Y. Oh, K. Wang, C. Dejoie, S.A.S. Asif, O.L. Warren, Z.W. Shan, J. Wu, A.M. Minor, Nano Lett., 11 (2011) 3207-3213.

[82] D. Kiener, A.M. Minor, Nano Lett., 11 (2011) 3816-3820.

[83] Y. Lu, J. Song, J.Y. Huang, J. Lou, Adv. Funct. Mater., 21 (2011) 3982-3989.

[84] B. Chen, Q. Gao, Y.B. Wang, X.Z. Liao, Y.-W. Mai, H.H. Tan, J. Zou, S.P. Ringer, C. Jagadish, Nano Lett., 13 (2013) 3169-3172.

[85] B. Chen, J. Wang, Q. Gao, Y.J. Chen, X.Z. Liao, C.S. Lu, H.H. Tan, Y.-W. Mai, J. Zou, S.P. Ringer, H.J. Gao, C. Jagadish, Nano Lett., 13 (2013) 4369-4373.

[86] J.W. Wang, F. Sansoz, J.Y. Huang, Y. Liu, S.H. Sun, Z. Zhang, S.X. Mao, Nat. Comm., 4 (2013) 1742.

[87] S. Dai, J. Zhao, M.-r. He, X.G. Wang, J.C. Wan, Z.W. Shan, J. Zhu, Nano Lett., 15 (2015) 8-15.

[88] Y.B. Wang, C.C. Lee, J. Yi, X.H. An, M.X. Pan, K.Y. Xie, X.Z. Liao, J.M. Cairney, S.P. Ringer, W.H. Wang, Scripta Mater., 84-85 (2014) 27-30.

[89] C. Chisholm, H.B. Bei, M.B. Lowry, J. Oh, S.A.S. Asif, O.L. Warren, Z.W. Shan, E.P. George, A.M. Minor, Acta Mater., 60 (2012) 2258-2264.

[90] Y.F. Zhang, X.D. Han, K. Zheng, Z. Zhang, X.N. Zhang, J.Y. Fu, Y. Ji, Y.J. Hao, X.Y. Guo, Z.L. Wang, Adv. Funct. Mater., 17 (2007) 3435-3440.

[91] L.H. Wang, X.D. Han, P. Liu, Y.H. Yue, Z. Zhang, E. Ma, Phys. Rev. Lett., 105 (2010) 135501.

[92] Y.H. Yue, P. Liu, Z. Zhang, X.D. Han, E. Ma, Nano Lett., 11 (2011) 3151-3155.

[93] Y.H. Yue, P. Liu, Q.S. Deng, E. Ma, Z. Zhang, X.D. Han, Nano Lett., 12 (2012) 4045-4049.

[94] Y.H. Yue, N.K. Chen, X.B. Li, S.B. Zhang, Z. Zhang, M.W. Chen, X.D. Han, Nano Lett., 13 (2013) 3812-3816.

[95] L.H. Wang, J. Teng, P. Liu, A. Hirata, E. Ma, Z. Zhang, M.W. Chen, X.D. Han, Nat. Comm., 5 (2014) 4402.

[96] J.S. Wang, X.J. Zheng, H. Zheng, Z. Zhu, S.T. Song, Appl. Surf. Sci., 256 (2010) 5998-6002.

[97] B. Zhou, B.C. Prorok, J. Mater. Res., 25 (2010) 1671-1678.

[98] S.X. Mao, M.H. Zhao, Z.L. Wang, Appl. Phys. Lett., 83 (2003) 993-995.

[99] M. Lucas, W.J. Mai, R.S. Yang, Z.L. Wang, E. Riedo, Nano Lett., 7 (2007) 1314-1317.

[100] X.D. Li, H.S. Gao, C.J. Murphy, K.K. Caswell, Nano Lett., 3 (2003) 1495-1498.

[101] G. Feng, W.D. Nix, Y. Yoon, C.J. Lee, J. Appl. Phys., 99 (2006) 074304.

[102] H. Ni, X.D. Li, Nanotechnology, 17 (2006) 3591-3597.

[103] W.C. Oliver, G.M. Pharr, J. Mater. Res., 7 (1992) 1564-1583.

[104] K. Kang, W. Cai, Philos. Mag., 87 (2007) 2169-2189.

[105] Y.H. Wen, Z.Z. Zhu, R.Z. Zhu, Comput. Mater. Sci., 41 (2008) 553-560.

[106] Y.H. Jing, Q.Y. Meng, Y.F. Gao, Comput. Mater. Sci., 45 (2009) 321-326.

[107] K. Kang, W. Cai, Int. J. Plasticity, 26 (2010) 1387-1401.

[108] B. Lee, R.E. Rudd, Phys. Rev. B, 75 (2007) 041305.

[109] B. Lee, R.E. Rudd, Phys. Rev. B, 75 (2007) 195328.

[110] A.V. Desai, M.A. Haque, Sensor Actuat. A-Phys., 134 (2007) 169-176.

[111] L.-W. Ji, S.-J. Young, T.-H. Fang, C.-H. Liu, Appl. Phys. Lett., 90 (2007) 033109-033109.

[112] G. Stan, C.V. Ciobanu, P.M. Parthangal, R.F. Cook, Nano Lett., 7 (2007) 3691-3697.

[113] G.F. Wang, X.D. Li, Appl. Phys. Lett., 91 (2007) 231912.

[114] S.J. Young, L.W. Ji, S.J. Chang, T.H. Fang, T.J. Hsueh, T.H. Meen, I.C. Chen, Nanotechnology, 18 (2007) 225603.

[115] R. Agrawal, B. Peng, E.E. Gdoutos, H.D. Espinosa, Nano Lett., 8 (2008) 3668-3674.

[116] M. Riaz, O. Nur, M. Willander, P. Klason, Appl. Phys. Lett., 92 (2008) 103118.

[117] M. Riaz, A. Fulati, Q.X. Zhao, O. Nur, M. Willander, P. Klason, Nanotechnology, 19 (2008) 415708.

[118] M.-R. He, Y. Shi, W. Zhou, J.W. Chen, Y.J. Yan, J. Zhu, Appl. Phys. Lett., 95 (2009) 091912.

[119] A. Asthana, K. Momeni, A. Prasad, Y.K. Yap, R.S. Yassar, Nanotechnology, 22 (2011) 265712.

[120] H.Y. Yao, G.H. Yun, Phys. E, 44 (2012) 1916-1919.

[121] H.Y. Yao, G.H. Yun, N. Bai, J.G. Li, J. Appl. Phys., 111 (2012) 083506.

[122] X.D. Bai, P.X. Gao, Z.L. Wang, E.G. Wang, Appl. Phys. Lett., 82 (2003) 4806-4808.

[123] C.-L. Hsin, W.J. Mai, Y.D. Gu, Y.F. Gao, C.-T. Huang, Y.Z. Liu, L.-J. Chen, Z.-L. Wang, Adv. Mater., 20 (2008) 3919-3923.

[124] M.J. Gordon, T. Baron, F. Dhalluin, P. Gentile, P. Ferret, Nano Lett., 9 (2009) 525-529.

[125] Y. Zhu, F. Xu, Q.Q. Qin, W.Y. Fung, W. Lu, Nano Lett., 9 (2009) 3934-3939.

[126] Y.S. Sohn, J. Park, G. Yoon, J. Song, S.W. Jee, J.H. Lee, S. Na, T. Kwon, K. Eom, Nanoscale Res. Lett., 5 (2010) 211-216.

[127] B. Lee, R.E. Rudd, Phys. Rev. B, 84 (2011) 161303.

[128] H.J. Joyce, Q. Gao, H.H. Tan, C. Jagadish, Y. Kim, J. Zou, L.M. Smith, H.E. Jackson, J.M. Yarrison-Rice, P. Parkinson, Prog. Quant. Electron., 35 (2011) 23-75.

[129] A.J. Kulkarni, M. Zhou, F.J. Ke, Nanotechnology, 16 (2005) 2749-2756.

[130] G.X. Cao, X. Chen, Int. J. Solids Struct., 45 (2008) 3821-3844.

[131] P. Schröer, P. Krüger, J. Pollmann, Phys. Rev. B, 49 (1994) 17092-17101.

[132] R.E. Miller, V.B. Shenoy, Nanotechnology, 11 (2000) 139-147.

[133] H.W. Shim, L.G. Zhou, H.C. Huang, T.S. Cale, Appl. Phys. Lett., 86 (2005) 151912.

[134] J. He, C.M. Lilley, Nano Lett., 8 (2008) 1798-1802.

[135] T.-Y. Zhang, M. Luo, W.K. Chan, J. Appl. Phys., 103 (2008) 104308.

[136] M.-S. Chiu, T.Y. Chen, Phys. E, 44 (2011) 714-718.

[137] M.-S. Chiu, T.Y. Chen, Procedia Eng., 10 (2011) 397-402.

[138] G.X. Cao, X. Chen, Phys. Rev. B, 76 (2007) 165407.

[139] R. Dingreville, J. Qu, M. Cherkaoui, J. Mech. Phys. Solids, 53 (2005) 1827-1854.

[140] R. Dingreville, A.J. Kulkarni, M. Zhou, J. Qu, Modell. Simul. Mater. Sci. Eng., 16 (2008) 025002.

[141] T.Y. Kim, S.S. Han, H.M. Lee, Mater. Trans., 45 (2004) 1442-1449.

[142] T. Kizuka, Y. Takatani, K. Asaka, R. Yoshizaki, Phys. Rev. B, 72 (2005) 035333.

[143] D.A. Smith, V.C. Holmberg, B.A. Korgel, ACS Nano, 4 (2010) 2356-2362.

[144] Y.B. Wang, H.J. Joyce, Q. Gao, X.Z. Liao, H.H. Tan, J. Zou, S.P. Ringer, Z.W. Shan, C. Jagadish, Nano Lett., 11 (2011) 1546-1549.

[145] J.J. Gilman, Electronic basis of the strength of materials, Cambridge University Press, New York, 2003.

[146] A. Rochefort, P. Avouris, F. Lesage, D.R. Salahub, Phys. Rev. B, 60 (1999) 13824-13830.

[147] E.D. Minot, Y. Yaish, V. Sazonova, J.Y. Park, M. Brink, P.L. McEuen, Phys. Rev. Lett., 90 (2003) 156401.

[148] K.H. Ahn, T. Lookman, A.R. Bishop, Nature, 428 (2004) 401-404.

[149] J. Cao, E. Ertekin, V. Srinivasan, W. Fan, S. Huang, H. Zheng, J.W.L. Yim, D.R. Khanal, D.F. Ogletree, J.C. Grossmanan, J. Wu, Nat. Nanotechnol., 4 (2009) 732-737.

[150] T. Koga, X. Sun, S.B. Cronin, M.S. Dresselhaus, Appl. Phys. Lett., 75 (1999) 2438-2440.

[151] A.R. Abramson, C.L. Tien, A. Majumdar, J. Heat Trans-T ASME, 124 (2002) 963-970.

[152] R.S. Jacobsen, K.N. Andersen, P.I. Borel, J. Fage-Pedersen, L.H. Frandsen, O. Hansen, M. Kristensen, A.V. Lavrinenko, G. Moulin, H. Ou, C. Peucheret, B. Zsigri, A. Bjarklev, Nature, 441 (2006) 199-202.

[153] V.M. Pereira, A.H. Castro Neto, Phys. Rev. Lett., 103 (2009) 046801.

[154] M. Ieong, B. Doris, J. Kedzierski, K. Rim, M. Yang, Science, 306 (2004) 2057-2060.

[155] P.R. Chidambaram, C. Bowen, S. Chakravarthi, C. Machala, R. Wise, IEEE Trans. Electron Dev., 53 (2006) 944-964.

[156] M. Chu, Y.K. Sun, U. Aghoram, S.E. Thompson, Annu. Rev. Mater. Res., 39 (2009) 203-229.

[157] R.R. He, P.D. Yang, Nat. Nanotechnol., 1 (2006) 42-46.

[158] L. David, R. Quinson, C. Gauthier, J. Perez, Polym. Eng. Sci., 37 (1997) 1633-1640.
[159] M. Wuttig, C.H. Lin, Acta Metall., 31 (1983) 1117-1122.
[160] J. San Juan, M.L. No, C.A. Schuh, Nat. Nanotechnol., 4 (2009) 415-419.
[161] L.S. Pan, S. Horibe, J. Mater. Sci., 31 (1996) 6523-6527.
[162] A. Caron, A. Kawashima, H.J. Fecht, D.V. Louzguine-Luzguin, A. Inoue, Appl. Phys. Lett., 99 (2011) 171907.
[163] L.S. Pan, S. Horibe, Acta Mater., 45 (1997) 463-469.
[164] H. Tanimoto, S. Sakai, H. Mizubayashi, Mater. Sci. Eng. A, 370 (2004) 135-141.
[165] G.M. Cheng, C.Y. Miao, Q.Q. Qin, J. Li, F. Xu, H. Haftbaradaran, E.C. Dickey, H.J. Gao, Y. Zhu, Nat. Nanotechnol., 10 (2015) 687-691.
[166] F. Oestlund, K. Rzepiejewska-Malyska, K. Leifer, L.M. Hale, Y. Tang, R. Ballarini, W.W. Gerberich, J. Michler, Adv. Funct. Mater., 19 (2009) 2439-2444.
[167] H. Van Swygenhoven, Science, 296 (2002) 66-67.
[168] X.Z. Liao, Y.H. Zhao, S.G. Srinivasan, Y.T. Zhu, R.Z. Valiev, D.V. Gunderov, Appl. Phys. Lett., 84 (2004) 592-594.
[169] Y.-J. Kim, K. Son, I.-C. Choi, I.-S. Choi, W.I. Park, J.-i. Jang, Adv. Funct. Mater., 21 (2011) 279-286.
[170] D. Zhang, J.-M. Breguet, R. Clavel, V. Sivakov, S. Christiansen, J. Michler, J. Microelectromech. Syst., 19 (2010) 663-674.
[171] M.S. Steighner, L.P. Snedeker, B.L. Boyce, K. Gall, D.C. Miller, C.L. Muhlstein, J. Appl. Phys., 109 (2011) 033503.
[172] J. Samuels, S.G. Roberts, P.B. Hirsch, Mater. Sci. Eng. A, 105 (1988) 39-46.
[173] M. Brede, Acta Metall. Mater., 41 (1993) 211-228.
[174] M.A. Meyers, K.K. Chawla, Mechanical behavior of materials, Cambridge university press, Cambridge, 2009.
[175] Z. Yuan, K.-i. Nomura, A. Nakano, Appl. Phys. Lett., 100 (2012) 153116.
[176] Z.W. Pan, Z.R. Dai, Z.L. Wang, Appl. Phys. Lett., 80 (2002) 309-311.
[177] E.W. Wong, P.E. Sheehan, C.M. Lieber, Science, 277 (1997) 1971-1975.
[178] D.Y.R. Chong, W.E. Lee, B.K. Lim, J.H.L. Pang, T.H. Low, Inter Society Conference on Thermal Phenomena, IEEE, 2004, pp. 203-210.
[179] C.S. Lu, R. Danzer, F.D. Fischer, Phys. Rev. E, 65 (2002) 067102.

[180] J.J. Brown, A.I. Baca, K.A. Bertness, D.A. Dikin, R.S. Ruoff, V.M. Bright, Sensor Actuat. A-Phys., 166 (2011) 177-186.

[181] G.M. Cheng, T.-H. Chang, Q.Q. Qin, H.C. Huang, Y. Zhu, Nano Lett., 14 (2014) 754-758.

[182] P.F. Li, Q.L. Liao, S.Z. Yang, X.D. Bai, Y.H. Huang, X.Q. Yan, Z. Zhang, S. Liu, P. Lin, Z. Kang, Y. Zhang, Nano Lett., 14 (2014) 480-485.

[183] Z.Y. Gao, Y. Ding, S.S. Lin, Y. Hao, Z.L. Wang, Phys. Status Solidi Rapid Res. Lett., 3 (2009) 260-262.

[184] B.D. Liu, Y. Bando, C.C. Tang, F.F. Xu, J.Q. Hu, D. Golberg, J. Phys. Chem., B, 109 (2005) 17082-17085.

[185] Z. Chen, C.B. Cao, H.S. Zhu, Chem. Vap. Deposition, 13 (2007) 527-532.

[186] J. Wang, C.S. Lu, Q. Wang, P. Xiao, F.J. Ke, Y.L. Bai, Y.G. Shen, X.Z. Liao, H.J. Gao, Nanotechnology, 23 (2012) 025703.

[187] Y.-G. Jung, B.R. Lawn, M. Martyniuk, H. Huang, X.Z. Hu, J. Mater. Res., 19 (2004) 3076-3080.

[188] Z. Wu, Y.-W. Zhang, M.H. Jhon, H. Gao, D.J. Srolovitz, Nano Lett., 12 (2012) 910-914.

[189] D.B. Murphy, Fundamentals of light microscopy and electronic imaging, John Wiley & Sons, 2002.

[190] E. Abbe, Arch Mikrosk Anat, 9 (1873) 413-418.

[191] J.J. Thomson, Philos. Mag., 44 (1897) 93.

[192] L.d. Broglie, Philos. Mag., 47 (1924) 446-458.

[193] D.B. Williams, C.B. Carter, Springer: New York, 2009.

[194] H. Busch, Ann. Phys., 386 (1926) 974-993.

[195] M. Knoll, E. Ruska, Z. Phys., 78 (1932) 318-339.

[196] M. Von Ardenne, Z. Phys., 109 (1938) 553-572.

[197] L. Reimer, Transmission electron microscopy: physics of image formation and microanalysis, Springer, 2013.

[198] J. Goldstein, D.E. Newbury, P. Echlin, D.C. Joy, A.D. Romig Jr, C.E. Lyman, C. Fiori, E. Lifshin, Scanning electron microscopy and X-ray microanalysis: a text for biologists, materials scientists, and geologists, Springer Science & Business Media, 2012.

[199] N. Gane, F.P. Bowden, J. Appl. Phys., 39 (1968) 1432-1435.

[200] N. Gane, Proceedings of the Royal Society of London A: Mathematical, Physical and Engineering Sciences, The Royal Society, 1970, pp. 367-391.
[201] PI 95 TEM PicoIndenter User Manual, Hysitron Incorporated, 2011.
[202] Y.H. Zhao, Y.Z. Guo, Q. Wei, A.M. Dangelewicz, C. Xu, Y.T. Zhu, T.G. Langdon, Y.Z. Zhou, E.J. Lavernia, Scripta Mater., 59 (2008) 627-630.
[203] J.T. Wang, C.H. Yang, P.D. Hodgson, Scripta Mater., 69 (2013) 626-629.
[204] R. Courant, Bull. Amer. Math. Soc, 49 (1943) 1-23.
[205] K.H. Huebner, D.L. Dewhirst, D.E. Smith, T.G. Byrom, The finite element method for engineers, John Wiley & Sons, 2008.
[206] Y.J. Chen, X.H. An, X.Z. Liao, Y.-W. Mai, Nanotechnology, 26 (2015) 435704.
[207] K. Hibbitt, ABAQUS theory manual and analysis user's manual, Hibbitt, Karlsson and Sorensen, Inc, Pawtucket, 2002.
[208] E. Riks, Int. J. Solids Struct., 15 (1979) 529-551.
[209] H.T. Zhang, B.E. Schuster, Q.M. Wei, K.T. Ramesh, Scripta Mater., 54 (2006) 181-186.
[210] Z.F. Zhang, J. Eckert, Phys. Rev. Lett., 94 (2005) 094301.
[211] K. Pemasiri, M. Montazeri, R. Gass, L.M. Smith, H.E. Jackson, J. Yarrison-Rice, S. Paiman, Q. Gao, H.H. Tan, C. Jagadish, Nano Lett., 9 (2009) 648-654.
[212] F.J. Lopez, E.R. Hemesath, L.J. Lauhon, Nano Lett., 9 (2009) 2774-2779.
[213] K.A. Dick, J. Bolinsson, M.E. Messing, S. Lehmann, J. Johansson, P. Caroff, J. Vac. Sci. Technol., B, 29 (2011) 04D103.
[214] L. Lu, X. Chen, X.X. Huang, K. Lu, Science, 323 (2009) 607-610.
[215] X.Y. Li, Y.J. Wei, L. Lu, K. Lu, H.J. Gao, Nature, 464 (2010) 877-880.
[216] K.A. Afanasyev, F. Sansoz, Nano Lett., 7 (2007) 2056-2062.
[217] Y.H. Zhao, J.F. Bingert, X.Z. Liao, B.Z. Cui, K. Han, A.V. Sergueeva, A.K. Mukherjee, R.Z. Valiev, T.G. Langdon, Y.T. Zhu, Adv. Mater., 18 (2006) 2949-2953.
[218] N. Akopian, G. Patriarche, L. Liu, J.-C. Harmand, V. Zwiller, Nano Lett., 10 (2010) 1198-1201.
[219] C. Thelander, P. Caroff, S. Plissard, A.W. Dey, K.A. Dick, Nano Lett., 11 (2011) 2424-2429.
[220] S. Lehmann, D. Jacobsson, K. Deppert, K.A. Dick, Nano Res., 5 (2012) 470-476.

[221] T. Burgess, S. Breuer, P. Caroff, J. Wong-Leung, Q. Gao, H.H. Tan, C. Jagadish, ACS Nano, 7 (2013) 8105-8114.
[222] S.L. Wang, G.L. Chen, H. Huang, S.J. Ma, H.Y. Xu, Y.H. He, J. Zou, Nanotechnology, 24 (2013) 505705.
[223] H.L. Duan, J. Wang, Z.P. Huang, B.L. Karihaloo, J. Mech. Phys. Solids, 53 (2005) 1574-1596.
[224] J. Wang, A. Misra, Curr. Opin. Solid State Mater. Sci., 15 (2011) 20-28.
[225] D. Barettin, A.V. Platonov, A. Pecchia, V.N. Kats, G.E. Cirlin, I.P. Soshnikov, A.D. Bouravleuv, L. Besombes, H. Mariette, M. Auf der Maur, IEEE J. Sel. Top. Quantum Electron., 19 (2013) 1-9.
[226] M.D. Kluge, D. Wolf, J.F. Lutsko, S.R. Phillpot, J. Appl. Phys., 67 (1990) 2370-2379.
[227] S.M. Sze, Semiconductor sensors, Wiley New York, 1994.
[228] J. Schiotz, F.D. Di Tolla, K.W. Jacobsen, Nature, 391 (1998) 561-563.
[229] J.A. Chisholm, P.D. Bristowe, J. Phys.: Condens. Matter, 11 (1999) 5057.
[230] Y. Umeno, Y. Kinoshita, T. Kitamura, Modell. Simul. Mater. Sci. Eng., 15 (2007) 27-37.
[231] M.A. Makeev, D. Srivastava, M. Menon, Phys. Rev. B, 74 (2006) 165303.
[232] H. Sadeghian, C.-K. Yang, J.F. Goosen, A. Bossche, U. Staufer, P.J. French, F. van Keulen, J. Micromech. Microeng., 20 (2010) 064012.
[233] J. Wang, Q.-A. Huang, H. Yu, Solid State Commun., 145 (2008) 351-354.
[234] C.Q. Sun, B.K. Tay, X.T. Zeng, S. Li, T.P. Chen, J. Zhou, H.L. Bai, E.Y. Jiang, J. Phys.: Condens. Matter, 14 (2002) 7781.
[235] J.V. Barth, H. Brune, G. Ertl, R.J. Behm, Phys. Rev. B, 42 (1990) 9307.
[236] L.H. Liang, H.S. Ma, Y.G. Wei, J. Nanomaterials, 2011 (2011) 24.
[237] R.C. Cammarata, K. Sieradzki, Phys. Rev. Lett., 62 (1989) 2005.
[238] R.N. Musin, X.-Q. Wang, Phys. Rev. B, 71 (2005) 155318.
[239] Y.L. Chueh, C.H. Hsieh, M.T. Chang, L.J. Chou, C.S. Lao, J.H. Song, J.Y. Gan, Z.L. Wang, Adv. Mater., 19 (2007) 143-149.
[240] X.W. Liu, J. Hu, B.C. Pan, Phys. E, 40 (2008) 3042-3048.